MICROMECHANICS MODELING OF NONLINEAR AND TIME-DEPENDENT RESPONSES OF PIEZOELECTRIC 1-3, 0-3, AND HYBRID COMPOSITES

A Dissertation

by

CHIEN-HONG LIN

Submitted to the Office of Graduate and Professional Studies of
Texas A&M University
in partial fulfillment of the requirements for the degree of

DOCTOR OF PHILOSOPHY

Chair of Committee,	Anastasia Muliana
Committee Members,	Hong Liang
	Miladin Radovic
	Stefan Hurlebaus
Head of Department,	Andreas Polycarpou

May 2014

Major Subject: Mechanical Engineering

ABSTRACT

Nonlinear electromechanical and polarization switching behaviors of piezoelectric materials and viscoelastic nature of polymers result in the overall nonlinear and hysteretic responses of active polymeric composites. Understanding the nonlinear behavior of the active polymeric composites is crucial in designing structures comprising of these active materials. This study presents three micromechanical models, i.e., fiber-, particle-, and hybrid-unit-cell models, to study the effective nonlinear and hysteretic electro-mechanical responses of 1-3, 0-3, and hybrid piezocomposites, respectively. The microstructures of the active composites are idealized with periodically distributed arrays of cubic representative unit cells. A unit cell is divided into several subcells. The fiber- and particle-unit-cell models consist of four and eight subcells, respectively. The hybrid-unit-cell model is derived based on the fiber-unit-cell model of 1-3 active composites consisting of fiber and matrix subcells, in which the matrix subcells are comprised of a particle-unit-cell model of 0-3 active composites. In order to obtain the overall nonlinear responses of the active composites linearized micromechanical relations are first used to provide trial solutions followed by iterative schemes in order to correct errors from linearizing the nonlinear responses. The micromechanical predictions are capable in predicting the overall nonlinear electromechanical, time-dependent, and polarization switching responses of active composites available in literature. Parametric studies are also performed to illustrate the effects of microstructural geometry and volume content of the piezoelectric inhomogeneities as well as loading history on the

overall nonlinear and hysteretic responses of active composites. Finally, a multi-scale analysis of a functionally graded piezoelectric bimorph actuator using the developed particle-unit-cell model is given as an example of practical applications.

DEDICATION

To my parents

ACKNOWLEDGEMENTS

This dissertation is based on my doctoral study which was conducted at Texas A&M University. This research was supported by Air Force Office of Scientific Research (AFOSR) Multi-Scale Structural Mechanics and Prognosis under grant FA 9550-10-1-0002 (Dr. David Stargel).

I gratefully acknowledge Dr. Muliana who first introduced me to the micromechanics of composite materials. I want to thank Dr. Muliana for her academic guidance, fruitful ideas, countless encouragements, and support to complete this dissertation. I extend my gratitude to my committee members, Dr. Liang, Dr. Radovic, and Dr. Hurlebaus, for their insightful comments to improve the quality of this dissertation. I would also like to thank Texas A&M Supercomputing Facility (http://sc.tamu.edu/) for providing computing resources useful in conducting this research.

Moreover, thanks go to my friends, colleagues and department faculties and staffs for making my life at Texas A&M University a great experience. I thank my parents, my family and doubleU who let me have peace of mind which enable me to do what I like to do most.

In closing, I hope this work can be useful and serve as a starting point for further research.

NOMENCLATURE

FE	Finite Element
FGM	Functionally Graded Material
MT	Mori-Tanaka
PZT	Lead Zirconate Titanate
RVE	Representative Volume Element
SC	Self-consistent
UC	Unit Cell
VF	Volume Fraction

TABLE OF CONTENTS

Page

LIST OF FIGURES

Page

LIST OF TABLES

Page

CHAPTER I

INTRODUCTION AND LITERATURE REVIEW[1]

In 1880, Curie brothers discovered that several natural materials, including quartz and Rochelle salt, exhibited an electromechanical coupling property. Since then, there have been vast developments of man-made materials that exhibit electromechanical coupling behavior. One of the most commonly used materials with electro-mechanical coupling is piezoelectric ceramics, such as lead zirconate titanate (PZT) and barium titanate ($BaTiO_3$). Piezoceramics exhibit high electromechanical coupling behavior; as a result they are used as sensors and actuators in smart devices and intelligent structures.

Due to their inherently brittle characteristics, piezoceramics are often dispersed in compliant/soft matrix such as polymers, which forms piezoelectric (active) composites. The use of piezoelectric composites enhances energy absorber capability in smart structures and creates more compliant devices. Several types of piezocomposites have been developed. For examples piezoelectric unidirectional fibers or particles embedded in a polymer matrix which forms 1-3 and 0-3 piezocomposites, respectively,

[1] Parts of this chapter are taken from: Lin, C.-H., and A. Muliana. 2013a. "Micromechanics Models for the Effective Nonlinear Electro-mechanical Responses of Piezoelectric Composites," *Acta Mech.*, 224(7):1471-1492 and reprinted with permission of Springer Publishing, Inc. Copyright 2013 by Springer Publishing, Inc. and from: Lin, C.-H., and A. Muliana. 2013b. "Micromechanical Models for the Effective Time-dependent and Nonlinear Electromechanical Responses of Piezoelectric Composites," *J Intel. Mat. Syst. Str.*, doi:10.1177/1045389X13504477 and reprinted with permission of Sage Publications, Inc. Copyright 2013 by Sage Publications, Inc.

are widely used in many engineering applications. Swallow et al. (2008) developed a wearable energy-harvesting device by using piezoelectric fibers embedded in an epoxy matrix. Hori et al. (2001) blended piezoelectric and carbon black power into an epoxy resin to develop piezoelectric damping materials.

Many 1-3 piezocomposites use polymer as their matrix medium. However, polymers have relatively low mechanical and electrical properties compared to those of piezoceramic fibers, such as PZT fibers; thus, limiting the potential applications of the piezocomposites. Significant mismatches in the electromechanical properties of the fiber and matrix could lead to high stress discontinuities at the interface between the fibers and matrix, which could cause debonding. Neat polymeric matrix is often modified by adding particulate fillers in order to improve the properties of the polymeric matrix, which forms a hybrid composite[2] with fibers and particles embedded in polymeric matrix.

1.1 Motivation

Piezoelectric materials exhibit prominent nonlinear behaviors when they are subjected to high electric fields, which are often the case in actuator applications. The nonlinear behavior is also seen in the hysteretic polarization and butterfly strain responses when piezoelectric materials are subjected to a cyclic electric field input with high amplitude, in which the materials experience polarization switching. Polymers naturally exhibit viscoelastic behaviors (see Ferry, 1970) and the viscoelastic behavior is

[2] The hybrid composite defined in this study is a three-phase composite having both fibers and particles in a matrix in order to distinguish a two-phase composite which has either only fibers or only particles in a matrix, i.e., a 1-3 or 0-3 composite.

more pronounced when they are exposed to hostile environmental conditions, such as elevated temperatures and high moisture contents. As the overall performance of piezocomposites depend on the responses of all constituents, it is necessary to study the overall time-dependent and nonlinear behaviors of piezocomposites prior to designing smart devices made of these piezocomposites, which is currently limited.

Micromechanics modeling has been used to determine effective properties and responses of the heterogeneous materials, including piezocomposites. Current works on micromechanical modeling of piezocomposites are primary focus on linear electro-mechanical constitutive behavior. Thus, it is essential to formulate micromechanical models, which are capable of estimating the overall time-dependent and nonlinear behavior of the piezocomposites and active hybrid composites, which can support the design of smart devices made of piezocomposites.

1.2 Literature Review

This section discusses a state of art knowledge in the overall response of piezoceramics, piezocomposites, and active hybrid composites in terms of experimental observations, electro-mechanical constitutive models, and micromechanical modeling.

1.2.1 Piezoceramics

When polarized piezoceramics are subject to large electric fields as in the case of actuators, the electromechanical coupling responses are shown to be nonlinear, which had been experimentally observed by Crawley and Anderson (1990) and Park et al. (1998). Figure 1.1 depicts the experimental data (symbols), from Crawley and Anderson (1990), of in-plane strain response of a stress free polarized PZT-G1195 ceramic plate

subject to an electric field input along the poling direction. The maximum electric field applied is ~1MV/m, which was 85% of the coercive electric field of the PZT-G1195. Thus, under the maximum electric field of 1 MV/m, the PZT-G1195 does not experience depolarization and polarization switching. As illustrated in the hysteretic polarization and butterfly strain responses under a cyclic electric field input (Figure 1.2), polarization switching occurs when the electric field input is higher than the coercive electric field and the applied electric field is in the opposite direction to the current poling direction. When the sample has been polarized (point B) and on the polarized sample, an electric field is applied in the poling direction (dashed line) with a magnitude below the coercive field electric field, a nonlinear electro-mechanical coupling response is observed when a relatively large electric field is applied. In order to describe the nonlinear electromechanical coupling behavior, Tiersten (1993) proposed a nonlinear constitutive model of piezoelectrictricity by considering higher-order terms of the electric field. In contrast, a linear constitutive model of piezoelectrictricity, which is often used for polarized piezoceramics and had been standardized by IEEE (1987), cannot capture the nonlinear electro-mechanical response of the sample, as shown in Figure 1.1. It is necessary to consider the nonlinear constitutive model (solid line) in order to capture the electro-mechanical response of the piezoelectric materials and the linear constitutive model (dashed line) is useful for a relatively small electric field input.

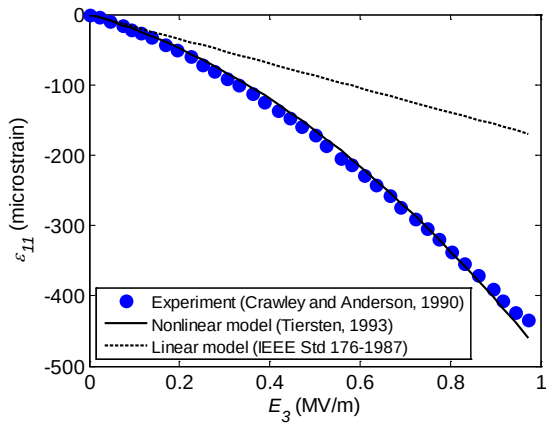

Figure 1.1 Strain-electric field curve (ε_{11} vs. E_3) for a stress free polarized PZT-G1195.

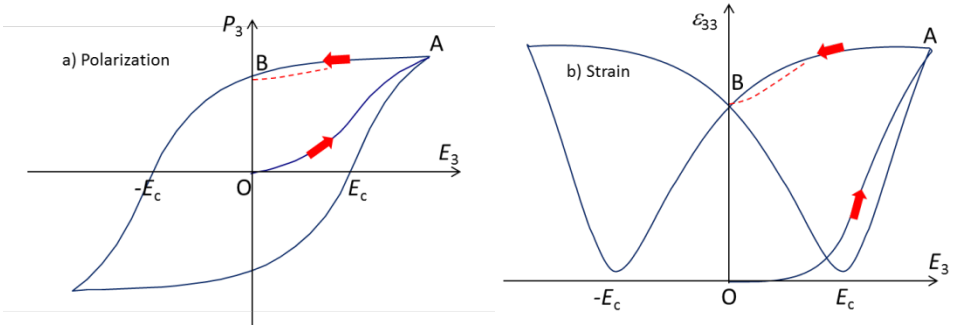

Figure 1.2 Examples of the a) polarization and 2) butterfly strain responses in ferroelectric materials due to a cyclic electric field. The operating range of a polarized piezoelectric material is shown by a dashed line.

The nonlinear behavior is also seen in the hysteretic polarization and butterfly strain responses when piezoceramics are subjected to a cyclic electric field input with high amplitude, in which the materials experience polarization switching. A polarized

piezoceramics can be depolarized by a high compressive stress applied in its poling axis. Unlike polarization switching induced by an electric field, the depolarized piezoceramics caused by a compressive stress cannot be repolarized by simply applying mechanical stresses. Extensive experimental and theoretical studies have been done on understanding nonlinear polarization switching responses in ferroelectric ceramics. Some of the prominent works in this area can be found in Cao and Evans (1993), Fang and Li (1999), Hwang et al. (1995), Kamlah (2001) and Landis (2004). The electrical and mechanical responses of piezoceramics are time-dependent (Fett and Thun 1998; Cao and Evans, 1993; Hall, 2001). Zhou and Kamlah (2005, 2006) have examined the creep responses in soft PZT under static electric fields and compressive stresses. The creep responses were significant at higher stress and at electric field near the coercive electric field. The hysteretic responses of piezoceramics strongly depend on the amplitude of electric fields, frequencies, existence of stresses, and ambient temperatures. Experimental studies have shown the degradation in the hysteretic electro-mechanical responses of several ferroelectric ceramics, both bulk and thin film structures, after several cycles of electric field inputs (Jiang et al., 1994; Dausch 1997; Wang et al., 1998; Zhang et al., 2001; Lou, 2009; Ma et al. 2011). The study showed a decrease in the saturated and remanent polarizations with degradation. Figure 1.3 depicts the experimental data (square and circle symbols) from Fang and Li (1999) of the hysteretic polarization and butterfly strain responses of a stress free PZT-51 subject to a cyclic electric field loading along the poling direction, which illustrates the time-dependent polarization switching responses.

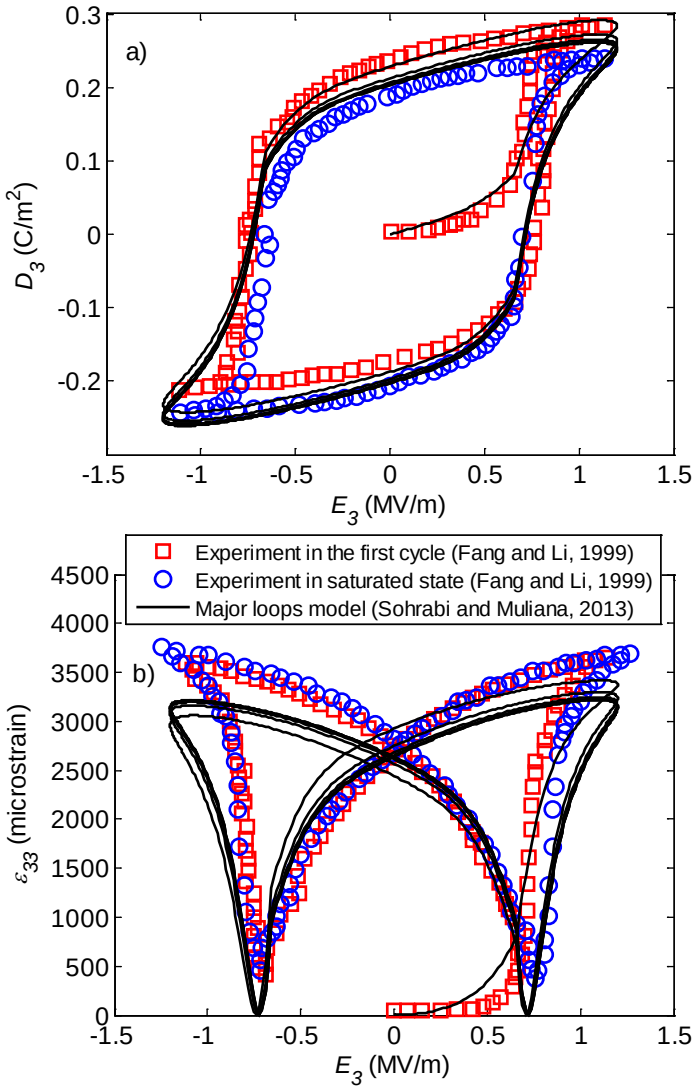

Figure 1.3 a) Hysteretic polarization and b) hysteretic butterfly strain responses for a stress free PZT-51.

There have been several constitutive models formulated for the polarization switching responses. The first type of models is motivated by considering domain switching in the crystallites of the piezoelectric ceramics. The bulk behavior of the

polycrystalline piezoelectric material is determined by averaging the domain switching of the individual grains. Examples of domain switching constitutive models can be found in Hwang et al. (1995), Chen and Lynch (1998), Huber et al. (1999), and Lu et al. (1999). A recent review article from Huber (2005) gives an overview in terms of modeling of microscopic polarization switching mechanisms. The second type of models focuses on macroscopic behavior of piezoceramics through the development of phenomenological constitutive model. Two examples in this category are: Bassiouny et al. (1988) used thermodynamical theory to model polarization switching behavior in the form of plasticity evaluation for the plastic strain, residual polarization, and both mechanical and electric hardenings. Zhou and Chattopadhyay (2000, 2001) adopted elastic Gibbs free energy to incorporate saturation polarization, remnant polarization, and coercive electric field on polarization switching behavior. The above constitutive models, however, focused on *rate-independent* constitutive relations. In a recent work by Sohrabi and Muliana (2013), a three-dimensional phenomenological constitutive model accounted for both rate-dependent polarization and compressive stress effect for piezoceramics was proposed. It is seen in Figure 1.3 that the constitutive model (solid lines) proposed by Sohrabi and Muliana (2013) can capture the experimental data quite well. Excellent review articles by Kamlah (2001) and Landis (2004) discussed both two categories of constitutive modeling on the nonlinear electromechanical hysteretic responses of piezoceramics.

1.2.2 Piezocomposites

Some experimental studies suggested that piezocomposites with polymeric matrix exhibit more desirable performance than monolithic piezoceramics. For instance, Smith (1986) and Safari (1994) reported that 1-3 piezocomposites have higher electromechanical coupling constant than that of conventional piezoceramic PZT. Bent and Hagood (1997) experimentally observed that 1-3 active composites, having PZT fibers, exhibit larger in-plane actuations than bulk PZTs. Alternatively, piezoceramics have been combined with conductive metals such as silver and platinum to form active composites. Hwang et al. (1997) and Zhang et al. (2006) experimentally observed that 0-3 active composites formed by adding silver particles in a PZT matrix exhibit higher fracture strength, fracture toughness and dielectric constant. A similar enhancement can be achieved by using platinum particles as reinforcement (Li et al., 2001 and Takagi et al., 2003) as well. In 0-3 active composites having silver fillers in a $BaTiO_3$ matrix also showed improvement in fracture strength as reported by Panteny et al. (2006). Performance of metal matrix composites with piezoceramics as reinforcements has also been studied. Experimental studies indicated that 0-3 metal matrix composites formed by adding $BaTiO_3$ particles into copper (Asare et al., 2005) or bronze (Poquette et al., 2005) exhibited higher passive damping capability than pure metal. Metallic based structures generally have high stiffness and strength; however, stiff materials typically have limited capability to damp out the mechanical or acoustical vibrations.

Micromechanical modeling of piezocomposites was started by Newnham's (1978) *connectivity* theory in which the micromechanical relations were derived based

on arrangements of different constituents in the piezocomposites. In order to determine the overall performance of piezocomposites, several micromechanical models have been developed. The results of the micromechanical models are the predictions of the effective properties and responses of heterogeneous materials based on the properties of the constituents and microstructural morphologies. The micromechanical model is formulated based on the assumption that a heterogeneous body is considered as a statistically homogeneous medium and the overall field variables, e.g., stress and strain, of the heterogeneous body can be evaluated by a volume-average scheme over a representative volume element (RVE). Early works on modeling 0-3 and 1-3 piezocomposites based on the connectivity theory can be found in Banno (1983) and Smith and Auld (1991), respectively. Numerous micromechanical models have been formulated to study the overall performance of piezocomposites. For predicting the effective linear electromechanical properties of piezocomposites, Nan and Jin (1993) and Nan (1994) proposed the effective-medium theory; Dunn and Taya (1993a) applied four micromechanical models, i.e., dilute, Mori-Tanaka (MT), self-consistent (SC) and differential models; Aboudi (1998) used generalized method of cells model (presented in Aboudi, 1991); and Odegard (2004) extended Dvorak and Srinivas's (1999) model. Only limited micromechanical models consider the nonlinear and field-dependent responses of piezoceramics embedded in an elastic matrix in predicting the responses of piezocomposites (Tan and Tong, 2001 and Muliana and Lin, 2011). For predicting responses of the composites having piezoelectric inhomogeneities in a linear viscoelastic matrix, Li and Dunn (2001a) as well as Jiang and Batra (2001) used the correspondence

principle of linear viscoelasticity within the MT model in order to determine the effective complex electromechanical moduli for piezoelectric fiber-reinforced and laminated composites. Muliana and Li (2010) presented a simplified micromechanical model and representative microstructures generated using finite element (FE) to estimate the linear time-dependent responses of 1-3 piezocomposites. Arafa and Baz (2000) used FE method to study the complex properties of a piezocomposite with PZT rods embedded in a viscoelastic matrix. It should be emphasized that the constitutive relations that were employed by these authors are restricted to the modeling of *polarized* piezocomposites.

Only limited micromechanical models are available for predicting the hysteretic polarization switching responses of active composites comprising of piezoceramics inclusions. Aboudi (2005) used high fidelity generalized method of cells micromechanical model together with the phenomenological constitutive model proposed by Zhou and Chattopadhyay (2001) to predict the effective polarization switching responses of 1-3 active composites. Muliana (2010) extend the phenomenological constitutive model in Zhou and Chattopadhyay (2000) to incorporate inelastic mechanical responses to model hysteretic behaviors of piezoceramics and further implemented the constitutive model in a simplified micromechanical model in order to estimate overall hysteretic responses of a 1-3 active composite whose epoxy matrix is consider as a viscoelastic medium. Jayendiran and Arockiarajan (2012, 2013) adopted the equivalent layered approach proposed by Kar-Gupta and Venkatesh (2007) and the domain switching constitutive model based on a switching criterion proposed by

Jayabal et al. (2009) to study the effective hysteresis of 1-3 active composites. It should be noted that the above micromechanics models merely considered *rate-independent hysteretic* constitutive relations for piezoelectric constituents.

1.2.3 Hybrid composites

There have been several experimental studies conducted on enhancing the mechanical properties of 1-3 composites by dispersing particulate fillers into the matrix. For examples, hybrid composites show significant improvements in the transverse strength (Gadkaree, 1992, and Tsai and Wu, 2007), the flexural strength (Hussain et al., 1996, Wang et al., 1997, and Asi, 2009), the longitudinal compressive strength (Vlasveld et al., 2005, Zheng et al., 2005, Subramaniyan and Sun, 2006, Cho et al., 2007 and Uddin and Sun, 2008), and the bearing strength (Asi 2010). Hagood and Bent (1993) and Bent and Hagood (1997) have shown that improvement in the overall dielectric constants of a 1-3 piezocomposite could be achieved by adding PZT powder with a dispersing agent into the epoxy matrix. Bent and Hagood (1997) also showed that a matrix system incorporating both dielectric and conductive fillers reduces the magnitude of voltages required for poling the 1-3 piezocomposites. Bent et al. (1995) discussed that 1-3 piezocomposites, which have relatively low transverse stiffness, are unable to bear large transverse loads without any additional substrates to enhance the structural stiffness.

While extensive micromechanics studies have been done on understanding responses of 1-3 piezocomposites (discussed in Section 1.2.2), only limited micromechanical models are available for predicting the overall responses of hybrid

piezocomposites, i.e., active composites comprising of multiple types and shapes of inclusions/inhomogeneities. Aldraihem et al. (2007) used the correspondence principle in conjunction with the MT model to evaluate the effective loss factor of a hybrid piezocomposite having shunted piezoelectric particles embedded in a conductive particle reinforced matrix. This model was extended by Aldraihem (2011) to derive the effective loss factor for a hybrid piezocomposite with orientation-dependent piezoelectric inhomogeneities and conductive inhomogeneities dispersed in a viscoelastic polymer.

1.3 Research Objective

This study presents micromechanical models for analyzing responses of active composites, including nonlinear electromechanical, time-dependent, and polarization switching responses for 1-3, 0-3, and hybrid piezocomposites. The specific aims are:

1) Develop fiber-, particle-, and hybrid- unit-cell (UC) micromechanical models for predicting effective responses of 1-3, 0-3, and hybrid piezocomposites, respectively. The proposed micromechanical models are used to predict the overall nonlinear electromechanical, time-dependent, and polarization switching responses of the studied piezocomposites.
2) Reformulate the widely used micromechanical model in literature, Mori-Tanaka (MT) model, to include nonlinear polarized piezoelectric and linear viscoelastic constitutive models. This is done in order to compare the UC predictions with MT estimations.
3) Validate the proposed UC micromechanical models with available experimental data in literature, e.g., Furukawa et al. (1976), Chan and

Unsworth (1989), Zeng et al. (2002), Hussain et al. (1996), and Jayendiran and Arockiarajan (2013).

4) Perform parametric study to examine the effects of microstructural geometry, i.e., unidirectional fiber and particle, and volume content of the piezoelectric inhomogeneities as well as various boundary conditions on the overall nonlinear and time-dependent responses of 1-3, 0-3, and hybrid piezocomposites by using the proposed UC micromechanical models.
5) Use the UC micromechanical models analyze electro-mechanical response of functionally graded piezoelectric bending actuator.

CHAPTER II

CONSTITUTIVE MODELS[3]

Piezoceramics are polarized by applying high electric field, above the coercive electric field at elevated temperature (Lines and Glass, 1977) before they are used in sensing and actuating applications. The polarized piezoceramics show electromechanical coupling response, which is quantified by piezoelectric constants. When high electric field is prescribed to the polarized piezoceramics, which is often the case in actuator applications, they exhibit nonlinear electromechanical coupling response. In this study, the constitutive model proposed by Tiersten (1993) is adopted for modeling nonlinear responses of polarized piezoceramics subject to a large electric field but smaller than coercive electric field of the piezoceramics. Another type of nonlinear electromechanical coupling response is hysteretic polarization switching response. Polarization switching can occur when high amplitude of cyclic electric field above the coercive electric field of the materials is considered. The constitutive model proposed by Sohrabi and Muliana (2013) is chosen for modeling the hysteretic polarization switching of piezoceramics. A linear viscoelastic constitutive model is used for the polymer constituent. This chapter

[3] Parts of this chapter are taken from: Lin, C.-H., and A. Muliana. 2013a. "Micromechanics Models for the Effective Nonlinear Electro-mechanical Responses of Piezoelectric Composites," *Acta Mech.*, 224(7):1471-1492 and reprinted with permission of Springer Publishing, Inc. Copyright 2013 by Springer Publishing, Inc. and from: Lin, C.-H., and A. Muliana. 2013b. "Micromechanical Models for the Effective Time-dependent and Nonlinear Electromechanical Responses of Piezoelectric Composites," *J Intel. Mat. Syst. Str.*, doi:10.1177/1045389X13504477 and reprinted with permission of Sage Publications, Inc. Copyright 2013 by Sage Publications, Inc.

briefly discusses the constitutive models used for the constituents in the active composites followed by numerical methods for solving the coupled nonlinear electro-mechanical constitutive relations.

2.1 Polarized Piezoceramic Model

2.1.1 Constitutive model

A nonlinear constitutive model proposed by Tiersten (1993) for polarized piezoceramics undergoing large electric fields and small strains is:

$$\varepsilon_{ij} = s_{ijkl}\sigma_{kl} + d_{kij}E_k + \frac{1}{2} f_{klij}E_l E_k, \tag{2.1}$$

$$D_i = d_{ikl}\sigma_{kl} + \kappa_{ij}E_j + \frac{1}{2}\chi_{ijk}E_k E_j, \tag{2.2}$$

where ε_{ij}, σ_{ij}, E_i and D_i are the scalar components of strain, stress, electric field and electric displacement, respectively. The material properties are the elastic compliances s_{ijkl} determined at a constant electric field, the third- and fourth-order piezoelectric strain coefficients d_{ijk} and f_{ijkl}, respectively, which are determined at constant stresses; and the second- and third-order dielectric coefficients κ_{ij} and χ_{ijk} calibrated at constant stresses. The higher-order term of the electric field is introduced in order to better capture the nonlinear response of the polarized PZTs due to large electric driving fields. Tiersten (1993) also discussed an alternative form of the constitutive model when strain and electric field are taken as the independent field variables:

$$\sigma_{ij} = c_{ijkl}\varepsilon_{kl} - e_{kij}E_k - \frac{1}{2}b_{klij}E_l E_k, \tag{2.3}$$

$$D_i = e_{ikl}\varepsilon_{kl} + \kappa_{ij}^{\varepsilon} E_j + \frac{1}{2}\chi_{ijk}^{\varepsilon} E_j E_k. \tag{2.4}$$

where c_{ijkl} is the elastic stiffness at a constant reference electric field, e_{ijk} and b_{ijkl} are the third- and fourth-order piezoelectric stress coefficients respectively, and $\kappa_{ij}^{\varepsilon}$ and χ_{ijk}^{ε} are the second- and third-order dielectric coefficients at a constant reference strain. The material properties given in Equations (2.3) and (2.4) are related to those in Equations (2.1) and (2.2) by

$$\mathbf{s} = \left(\mathbf{c}\right)^{-1}, \tag{2.5}$$

$$d_{ijk} = e_{imn} s_{jkmn}, \tag{2.6}$$

$$\kappa_{ij} = \kappa_{ij}^{\varepsilon} + e_{imn} d_{jmn}, \tag{2.7}$$

$$f_{ijkl} = b_{ijmn} s_{klmn}, \tag{2.8}$$

$$\chi_{ijk} = \chi_{ijk}^{\varepsilon} + e_{imn} f_{jkmn}. \tag{2.9}$$

Boldface variables indicate first order tensors or higher, for example, the fourth order tensors $\mathbf{s}$ and $\mathbf{c}$ in Equation (2.5).

2.1.2 Linearized constitutive model

For convenience in analyzing the time-dependent and nonlinear electromechanical behavior, we present a linearized incremental form of the constitutive relations, i.e., Equations (2.1) and (2.2). The incremental independent field variables at current time t are chosen as:

$$\Delta\boldsymbol{\sigma}^t = \boldsymbol{\sigma}^t - \boldsymbol{\sigma}^{t-\Delta t}, \tag{2.10}$$

$$\Delta\mathbf{E}^t = \mathbf{E}^t - \mathbf{E}^{t-\Delta t}, \tag{2.11}$$

where superscript $t-\Delta t$ denotes the previous time and Δt is the current incremental time. The linearized constitutive relation can be expressed in a single equation, which follows a conventional indicial notation with lower case subscripts range from 1 to 3 while upper case subscripts range from 1 to 4:

$$\Xi_{iJ}^{t} = O_{iJMn}^{t}\ \Delta T_{Mn}^{t} + \Xi_{iJ}^{t-\Delta t}, \tag{2.12}$$

where

$$\Xi_{iJ}^{t} = \begin{cases} \varepsilon_{ij}^{t}, & J = 1,2,3, \\ D_{i}^{t}, & J = 4, \end{cases} \tag{2.13}$$

$$O_{iJMn}^{t} = \begin{cases} \tilde{s}_{ijmn}^{t}, & J,M = 1,2,3, \\ \tilde{d}_{nij}^{t}, & J = 1,2,3;\ M = 4, \\ \tilde{d}_{imn}^{t}, & J = 4;\ M = 1,2,3, \\ \tilde{\kappa}_{in}^{t}, & J,M = 4, \end{cases} \tag{2.14}$$

$$\Delta T_{Mn}^{t} = \begin{cases} \Delta\sigma_{mn}^{t}, & M = 1,2,3, \\ \Delta E_{n}^{t}, & M = 4. \end{cases} \tag{2.15}$$

The components of O_{iJMn}^{t} are represented by a 9 by 9 matrix. Vectors Ξ_{iJ}^{t} and ΔT_{Mn}^{t} are 9 by 1 column vectors and $\Xi_{iJ}^{t-\Delta t}$ is the history variables of the dependent field variables Ξ_{iJ}^{t}. A factor of two for the shear strains is accounted for in the vector Ξ_{iJ}^{t}. This matrix formulation of the linearized constitutive relation will be used in the next chapter (Chapter III) for the micromechanical analysis. After some algebraic manipulations, the resulting components of O_{iJMn}^{t} and $\Xi_{iJ}^{t-\Delta t}$ for constitutive model of polarized piezoceramics are summarized as:

$$\tilde{s}_{ijmn}^{t} = s_{ijmn}, \tag{2.16}$$

$$\tilde{d}'^{t}_{nij} = d_{nij} + \frac{1}{2} f_{nlij} E^t_l, \tag{2.17}$$

$$\tilde{d}^t_{imn} = d_{imn}, \tag{2.18}$$

$$\tilde{\kappa}^t_{in} = \kappa_{in} + \frac{1}{2} \chi_{ink} E^t_k, \tag{2.19}$$

$$\varepsilon^{t-\Delta t}_{ij} = s_{ijkl} \sigma^{t-\Delta t}_{kl} + \left(d_{kij} + \frac{1}{2} f_{klij} E^t_l \right) E^{t-\Delta t}_k, \tag{2.20}$$

$$D^{t-\Delta t}_i = d_{ikl} \sigma^{t-\Delta t}_{kl} + \left(\kappa_{ij} + \frac{1}{2} \chi_{ijk} E^t_k \right) E^{t-\Delta t}_j. \tag{2.21}$$

2.2 Hysteretic Polarization Switching for Piezoceramics

2.2.1 Constitutive model

A rate-dependent electromechanical constitutive model, incorporating polarization switching response, formulated by Sohrabi and Muliana (2013), is given as:

$$\varepsilon^t_{ij} \equiv \varepsilon_{ij}(t) = s_{ijkl} \sigma^t_{kl} + 4 g^t_{nij} \kappa_{nm} g^t_{mkl} \sigma^t_{kl} + 2 g^t_{kij} P^t_k, \tag{2.22}$$

$$D^t_i = 2 \kappa_{im} g^t_{mkl} \sigma^t_{kl} + P^t_i, \tag{2.23}$$

where g^t_{ijk} is the scalar component of the third-order piezoelectric coefficient which is dependent on the current polarization P^t_3 with the x_3 direction chosen as the poling axis. The upper right superscript t indicates the current time. The piezoelectric constant g^t_{ijk} is assumed as:

$$g^t_{ijk} = \frac{P^t_3}{P_r} e^{\frac{-\left|P^t_3\right|}{c_1}} g^r_{ijk}, \tag{2.24}$$

where g_{ijk}^{r} is the scalar component of the third-order piezoelectric coefficient measured at constant (remanent) polarization P_r. It is noted that $\mathbf{g}^r = \boldsymbol{\kappa}^{-1}\mathbf{d}^r$., where $\mathbf{d}^r$ is the direct piezoelectric constant measured at remanent polarization. The scalar components of the polarization are

$$P_1^t = \kappa_{11} E_1^t, \tag{2.25}$$

$$P_2^t = \kappa_{22} E_2^t. \tag{2.26}$$

$$P_3^t = R(E_3^\tau, t) + Q(E_3^t), \tag{2.27}$$

where $R(E_3^\tau, t)$ is the time-dependent reversible polarization at current time t with $R(0, t)$=0 while $Q(E_3^t)$ is the residual (irreversible) polarization. The upper right superscript τ denotes the previous time variable. The reversible polarization is written as:

$$R^t = R(E_3^0, t) + \int_0^t \frac{\partial}{\partial E_3^\tau} R(E_3^\tau, t-\tau) \frac{dE_3^\tau}{d\tau} d\tau, \tag{2.28}$$

where

$$R(E_3^0, t) = R_0(E_3^0) + R_1(E_3^0)\left(1 - \exp\left(-\frac{t}{\tau_1}\right)\right). \tag{2.29}$$

Both $R_0(E_3^\tau)$ and $R_1(E_3^\tau)$ are function of E_3^τ. The characteristic time τ_1 indicates the speed of polarization changes. The irreversible polarization is given as:

$$Q^t = \int_0^{E_3^t} \frac{dQ^\tau}{dE_3^\tau} dE_3^\tau. \tag{2.30}$$

The rate of the residual polarization during polarization switching response is:

$$\frac{dQ^t}{dE_3^t}=\begin{cases}0, & 0\le E_3^t<E_m,\ dE_3^t<0 \quad \text{or} \quad -E_m<E_3^t\le 0,\ dE_3^t>0,\\ \lambda\left|\dfrac{E_3^t}{E_c}\right|^n, & -E_c\le E_3^t<0,\ dE_3^t\le 0 \quad \text{or} \quad 0<E_3^t\le E_c,\ dE_3^t\ge 0,\\ \mu\exp[-\omega\left(\dfrac{\left|E_3^t\right|}{E_c}-1\right)], & -E_m\le E_3^t<-E_c,\ dE_3^t\le 0 \quad \text{or} \quad E_c<E_3^t\le E_m,\ dE_3^t\ge 0,\end{cases} \tag{2.31}$$

where λ, μ, ω, n are the material parameters that are calibrated from experiments. A similar function with different material parameters can be used for modeling the initial polarization, as discussed in Muliana (2011).

The compressive stresses along the poling axis could significantly affect the hysteretic polarization switching response. In this study, it is assumed that the coercive electric field varies with the compressive stresses along the x_3 direction:

$$E_c=\begin{cases}E_c(E_c^0,\sigma_{33}^t), & \sigma_{33}^t<0,\\ E_c^0, & \sigma_{33}^t\ge 0,\end{cases} \tag{2.32}$$

where E_c^0 is the coercive electric field in absence of mechanical stresses. In order to incorporate the effect of compressive stress on the polarization switching responses, it is assumed that the compressive stress that is higher than the coercive stress limit affects the current polarization state P_3^t and the piezoelectric coefficient g_{ijk}^t:

$$g_{ijk}^t=\frac{P_3^t}{P_r}e^{\frac{-\left|P_3^t\right|}{c_1}}e^{\frac{-c_2\left|\sigma_{33}^t\right|}{\sigma_c}}g_{ijk}^r, \qquad c_2=0, \quad \text{if} \quad \sigma_{33}^t>-\sigma_c, \tag{2.33}$$

where σ_c is the coercive stress limit and C_2 is a material parameter.

2.2.2 Linearized constitutive model

A recursive time-integration algorithm presented in Taylor et al. (1970) is used to numerically evaluate the time integral forms of the constitutive models, i.e., Equation (2.28). After some algebraic manipulations, the resulting components of O^{t}_{iJMn} and $\Xi^{t-\Delta t}_{iJ}$ for constitutive model for modeling hysteretic polarization switching responses of piezoceramics are summarized as:

$$\tilde{s}^{t}_{ijmn} = s_{ijmn} + 4g^{t}_{kij}\kappa_{kl}g^{t}_{lmn}, \tag{2.34}$$

$$\tilde{d}^{\,t}_{nij} = 2g^{t}_{nij}K^{t}_{kl}, \tag{2.35}$$

$$\tilde{d}^{t}_{imn} = 2\kappa_{ij}g^{t}_{jmn}, \tag{2.36}$$

$$\tilde{\kappa}^{t}_{in} = K^{t}_{in}, \tag{2.37}$$

$$\varepsilon^{t-\Delta t}_{ij} = \left(s_{ijkl} + 4g^{t}_{nij}\kappa_{nm}g^{t}_{mkl}\right)\sigma^{t-\Delta t}_{kl} + 2g^{t}_{kij}\left(P^{t-\Delta t}_{k} + F^{t}_{k}\right), \tag{2.38}$$

$$D^{t-\Delta t}_{i} = 2\kappa_{im}g^{t}_{mkl}\sigma^{t-\Delta t}_{kl} + P^{t-\Delta t}_{i} + F^{t}_{i}, \tag{2.39}$$

where $R_0(E^{\tau}_3)$ and $R_1(E^{\tau}_3)$ in Equation (2.29) are considered as linear functions:

$$\begin{aligned} R_0(E^{\tau}_3) &= \kappa_0 E^{\tau}_3, \\ R_1(E^{\tau}_3) &= \kappa_1 E^{\tau}_3, \end{aligned} \tag{2.40}$$

where κ_0 is referred to the dielectric constant of a macroscopically unpolarized ferroelectric ceramics corresponding to the second-order permeability tensor in a multi-axial case while κ_1 is the time-dependent part of the dielectric constant. In Equations (2.35) and (2.37), K^{t}_{ij} is:

$$K_{ij}^{t}=\begin{cases}\kappa_{11}, & i=j=1,\\ \kappa_{22}, & i=j=2,\\ \kappa_{0}+\kappa_{1}+\Delta Q^{t}, & i=j=3,\\ 0, & i\neq j.\end{cases} \tag{2.41}$$

Using the rate of residual polarization in Equation (2.31), the incremental residual polarization at current time t is approximated by:

$$\Delta Q^{t}\approx\frac{dQ^{t}}{dE_{3}^{t}}\Delta E_{3}^{t}. \tag{2.42}$$

In Equations (2.38) and (2.39), F_{ij}^{t} and P_{i}^{t} are:

$$F_{i}^{t}=\begin{cases}0, & i=1,2,\\ \left[1-\exp[-\frac{\Delta t}{\tau_{1}}]\right]q^{t-\Delta t}-\left[\frac{\partial R_{1}(E_{3}^{t})}{\partial E_{3}^{t}}\frac{dE_{3}^{t}}{dt}+\exp[-\frac{\Delta t}{\tau_{1}}]\frac{\partial R_{1}(E_{3}^{t-\Delta t})}{\partial E_{3}^{t-\Delta t}}\frac{dE_{3}^{t-\Delta t}}{dt}\right]\frac{\Delta t}{2}, & i=3,\end{cases} \tag{2.43}$$

$$P_{i}^{t}=P_{i}^{t-\Delta t}+\Delta P_{i}^{t}, \tag{2.44}$$

where the history variable related to the polarization is:

$$q^{t}=\exp[-\frac{\Delta t}{\tau_{1}}]q^{t-\Delta t}+\left[\frac{\partial R_{1}(E_{3}^{t})}{\partial E_{3}^{t}}\frac{dE_{3}^{t}}{dt}+\exp[-\frac{\Delta t}{\tau_{1}}]\frac{\partial R_{1}(E_{3}^{t-\Delta t})}{\partial E_{3}^{t-\Delta t}}\frac{dE_{3}^{t-\Delta t}}{dt}\right]\frac{\Delta t}{2}, \tag{2.45}$$

and the incremental polarization is determined by:

$$\Delta P_{i}^{t}=K_{ij}^{t}\Delta E_{j}^{t}+F_{i}^{t}. \tag{2.46}$$

2.3 Polymers

2.3.1 Constitutive model

For the inactive constituent, a constitutive model for isotropic viscoelastic solid is considered:

$$\varepsilon_{ij}^{t} = (1+\nu)\int_0^t D(t-\tau)\frac{dS_{ij}^{\tau}}{d\tau}d\tau + \frac{(1-2\nu)}{3}\delta_{ij}\int_0^t D(t-\tau)\frac{d\sigma_{kk}^{\tau}}{d\tau}d\tau, \quad (2.47)$$

$$D_i = \kappa_{ij}E_j. \quad (2.48)$$

For simplicity, we assume that the corresponding linear elastic Poisson's ratio ν in to Equation (2.47) and dielectric constant κ_{ij} in to Equation (2.48) are time-independent[4]. S_{ij}^{t} and σ_{kk}^{t} are the components of the deviatoric stress and volumetric stress tensors at current time *t*, respectively. δ_{ij} is the Kronecker delta. $D(t)$ is the extensional (uniaxial) time-dependent compliance, which is expressed as:

$$D(t) = D_0 + \sum_{n=1}^{N} D_n\left(1-\exp[-\lambda_n t]\right). \quad (2.49)$$

Here D_0 is the instantaneous (elastic) compliance and the transient compliance is expressed in terms of a series of exponential functions (i.e., Prony series), where N is the number of terms, D_n is the *n*th coefficient of the time-dependent compliance and λ_n is the *n*th reciprocal of retardation time. The constitutive relation in Equation (12) reduces to linear elastic response in absence of the time-dependent variables.

2.3.2 Linearized constitutive model

Again, the recursive time-integration algorithm presented in Taylor et al. (1970) is used to numerically evaluate the time integral forms of the constitutive models, i.e.,

[4] Limited studies from Schapery (1974) and Le Moal and Perreux (1994) on the epoxy materials used for composites show that the Poison's effect is nearly constant. Several experimental studies suggest that the dielectric properties of polymers and piezoelectric materials are time-dependent, and the piezoelectric constants of several piezoceramics also show time-dependent behaviors. In this study we want to highlight the effect of the viscoelastic polymers on the overall electromechanical responses of piezocomposites; therefore we assumed the rest of the properties are time-independent for the polymers.

Equation (2.47). After some algebraic manipulations, the resulting components of O^t_{iJMn} and $\Xi^{t-\Delta t}_{iJ}$ for constitutive model of viscoelastic polymers are summarized as:

$$\tilde{s}^t_{ijmn} = \left(\frac{1}{3}\breve{B} - \frac{1}{3}\breve{J}\right)\delta_{ij}\delta_{mn} + 2\breve{J}\delta_{ik}\delta_{jl} - \breve{J}\delta_{il}\delta_{jk}, \tag{2.50}$$

$$\tilde{d}^{\,t}_{nij} = 0, \tag{2.51}$$

$$\tilde{d}^t_{imn} = 0, \tag{2.52}$$

$$\tilde{\kappa}^t_{in} = \kappa^t_{in}, \tag{2.53}$$

$$\varepsilon^{t-\Delta t}_{ij} = 2\left(\breve{J}S^{t-\Delta t}_{ij} - d^t_{ij}\right) + \delta_{ij}\left[-\breve{J}S^{t-\Delta t}_{ij} + d^t_{ij} + \frac{1}{3}\left(\breve{B}\sigma^{t-\Delta t}_{kk} - V^t_{kk}\right)\right], \tag{2.54}$$

$$D^{t-\Delta t}_i = \kappa_{ij}E^{t-\Delta t}_j. \tag{2.55}$$

In Equations (2.50), $\breve{B}$, $\breve{J}$, d^t_{ij} and V^t_{kk} are:

$$\breve{B}^t = (1-2\nu)\left[D_0 + \sum_{n=1}^{N} D_n - \sum_{n=1}^{N} D_n \frac{1-\exp[-\lambda_n\Delta t]}{\lambda_n\Delta t}\right], \tag{2.56}$$

$$\breve{J}^t = (1+\nu)\left[D_0 + \sum_{n=1}^{N} D_n - \sum_{n=1}^{N} D_n \frac{1-\exp[-\lambda_n\Delta t]}{\lambda_n\Delta t}\right], \tag{2.57}$$

$$d^t_{ij} = (1+\nu)\sum_{n=1}^{N} J_n\left[\exp[-\lambda_n\Delta t]q^{t-\Delta t}_{ij,n} - \frac{1-\exp[-\lambda_n\Delta t]}{\lambda_n\Delta t}S^{t-\Delta t}_{ij}\right], \tag{2.58}$$

$$V^t_{kk} = (1-2\nu)\sum_{n=1}^{N} J_n\left[\exp[-\lambda_n\Delta t]q^{t-\Delta t}_{kk,n} - \frac{1-\exp[-\lambda_n\Delta t]}{\lambda_n\Delta t}\sigma^{t-\Delta t}_{kk}\right], \tag{2.59}$$

where the history variables related to the deviatoric and volumetric strains are:

$$q_{ij,n}^{t} = \exp[-\lambda_n \Delta t] q_{ij,n}^{t-\Delta t} + \left[\frac{1-\exp[-\lambda_n \Delta t]}{\lambda_n \Delta t}\right]\left(S_{ij}^{t} - S_{ij}^{t-\Delta t}\right), \tag{2.60}$$

$$q_{kk,n}^{t} = \exp[-\lambda_n \Delta t] q_{kk,n}^{t-\Delta t} + \left[\frac{1-\exp[-\lambda_n \Delta t]}{\lambda_n \Delta t}\right]\left(\sigma_{kk}^{t} - \sigma_{kk}^{t-\Delta t}\right). \tag{2.61}$$

CHAPTER III

MICROMECHANICAL MODELS FOR FIBER, PARTICLE, AND HYBRID PIEZOCOMPOSITES[5]

This chapter presents simplified UC micromechanical models for studying nonlinear electromechanical, time-dependent, and polarization switching responses for 1-3, 0-3, and hybrid piezocomposites followed by formulation of MT model in order to include nonlinear polarized piezoelectric and linear viscoelastic constitutive relations.

3.1 Fiber- and Particle-unit-cell Models (An Incremental Formulation)

Fiber- and particle-unit-cell models are formulated which result in a rough approximation of the effective properties and responses of 1-3 and 0-3 composites, respectively. The composite microstructures are idealized with periodically distributed arrays of inhomogeneities in a homogeneous matrix. Figure 3.1 illustrates idealized microstructures for the 1-3 and 0-3 composites. A unit cell (UC) is selected as a representative volume element (RVE) and each UC is divided into several subcells. The first subcell denotes the inhomogeneity constituent and the rest of the subcells indicate the homogeneous matrix phase. A fiber UC with a unidirectional square fiber consisting

[5] Parts of this chapter are taken from: Lin, C.-H., and A. Muliana. 2013a. "Micromechanics Models for the Effective Nonlinear Electro-mechanical Responses of Piezoelectric Composites," *Acta Mech.*, 224(7):1471-1492 and reprinted with permission of Springer Publishing, Inc. Copyright 2013 by Springer Publishing, Inc. and from: Lin, C.-H., and A. Muliana. 2013b. "Micromechanical Models for the Effective Time-dependent and Nonlinear Electromechanical Responses of Piezoelectric Composites," *J Intel. Mat. Syst. Str.*, doi:10.1177/1045389X13504477 and reprinted with permission of Sage Publications, Inc. Copyright 2013 by Sage Publications, Inc.

of four subcells and a particle unit cell with a cubic particle consisting of eight subcells are used to approximate the responses of the 1-3 and 0-3 composites, respectively. The interfaces between all subcells are assumed perfectly bonded.

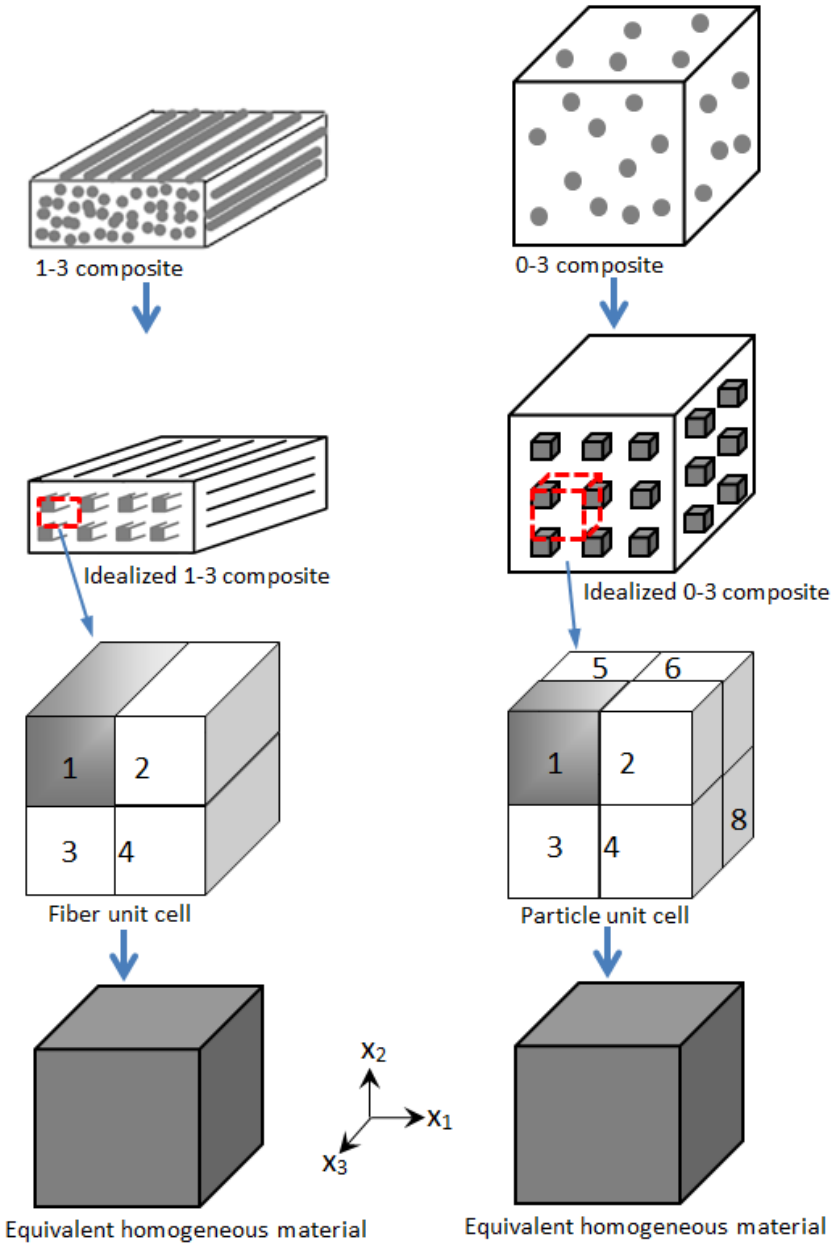

Figure 3.1 Fiber- and particle-unit-cell models.

The UC models are formulated based on simple micromechanical relations by satisfying equilibrium condition and displacement compatibility among all subcells. The time-integration algorithms for the rate-dependent ferroelectric ceramics, i.e., Equation (2.28), and viscoelastic matrix, i.e., Equation (2.47) are integrated to the UC models in order to obtain approximate solutions of the overall nonlinear and time-dependent responses of the 1-3 and 0-3 composites.

The linearized effective field variables, denoted by an overbar, of the UCs at current time t are determined based on:

$$\overline{\boldsymbol{\Xi}}^{t} = \sum_{\alpha=1}^{n} c^{(\alpha)} \boldsymbol{\Xi}^{(\alpha),t}, \tag{3.1}$$

where the superscript α denotes the subcells' number and n is the number of subcells (e.g. n=4 for a fiber UC and n=8 for a particle UC). The variable $\boldsymbol{\Xi}^{(\alpha),t}$ is the average field variable within each subcell with a volume $V^{(\alpha)}$. The UC volume V is given by

$$V = \sum_{\alpha=1}^{n} V^{(\alpha)}. \tag{3.2}$$

A linearized constitutive relation for the composite at current time t is written as:

$$\overline{\boldsymbol{\Xi}}^{t} = \overline{\mathbf{O}}^{t} \Delta \overline{\mathbf{T}}^{t} + \overline{\boldsymbol{\Xi}}^{t-\Delta t}, \tag{3.3}$$

and also for the subcell (α) is:

$$\boldsymbol{\Xi}^{(\alpha),t} = \mathbf{O}^{(\alpha),t} \Delta \mathbf{T}^{(\alpha),t} + \boldsymbol{\Xi}^{(\alpha),t-\Delta t}. \tag{3.4}$$

In order to relate the effective incremental independent field variable in the UC to the corresponding incremental field variable in its subcells, a concentration matrix $\mathbf{B}^{(\alpha),t}$ and a vector of history variables $\mathbf{X}^{(\alpha),t}$ at current time t are defined through the relation:

$$\Delta\mathbf{T}^{(\alpha),t} = \mathbf{B}^{(\alpha),t}\Delta\overline{\mathbf{T}}^{t} + \mathbf{X}^{(\alpha),t}. \tag{3.5}$$

Substituting $\Delta\mathbf{T}^{(\alpha),t}$ from Equation (3.5) into (3.4) gives

$$\boldsymbol{\Xi}^{(\alpha),t} = \mathbf{O}^{(\alpha),t}\mathbf{B}^{(\alpha),t}\Delta\overline{\mathbf{T}}^{t} + \mathbf{O}^{(\alpha),t}\mathbf{X}^{(\alpha),t} + \boldsymbol{\Xi}^{(\alpha),t-\Delta t}. \tag{3.6}$$

Substituting $\boldsymbol{\Xi}^{(\alpha),t}$ from Equation (3.6) into (3.1) gives

$$\overline{\boldsymbol{\Xi}}^{t} = \sum_{\alpha=1}^{n} c^{(\alpha)}\mathbf{O}^{(\alpha),t}\mathbf{B}^{(\alpha),t}\Delta\overline{\mathbf{T}}^{t} + \sum_{\alpha=1}^{n} c^{(\alpha)}\left(\mathbf{O}^{(\alpha),t}\mathbf{X}^{(\alpha),t} + \boldsymbol{\Xi}^{(\alpha),t-\Delta t}\right). \tag{3.7}$$

From Equations (3.7) and (3.3), the effective electro-mechanical properties and history variables of the UC are:

$$\overline{\mathbf{O}}^{t} = \sum_{\alpha=1}^{n} c^{(\alpha)}\mathbf{O}^{(\alpha),t}\mathbf{B}^{(\alpha),t}. \tag{3.8}$$

$$\overline{\boldsymbol{\Xi}}^{t-\Delta t} = \sum_{\alpha=1}^{n} c^{(\alpha)}\left(\mathbf{O}^{(\alpha),t}\mathbf{X}^{(\alpha),t} + \boldsymbol{\Xi}^{(\alpha),t-\Delta t}\right). \tag{3.9}$$

In order to evaluate the concentration matrices and history variables $\mathbf{B}^{(\alpha),t}$, $\mathbf{B}^{(\alpha,\beta),t}$ and $\mathbf{X}^{(\alpha),t}$, $\mathbf{X}^{(\alpha,\beta),t}$ in the fiber- and particle-unit-cell models it is necessary to include the constitutive relations for the different constituents together with the linearized micromechanical relations from the fiber UC and the particle UC. The linearized micromechanical relations for the fiber and particle UCs are listed in **Appendix A** and **B**, respectively. Because of the nonlinear constitutive relations for the constituents, the linearized micromechanical relations generally violate the overall nonlinear responses, which results in the following residual vector:

$$\left\{\mathbf{R}^{t}\right\} = \left[\mathbf{P}^{t}\right]\left\{\Delta\mathbf{T}_{s}^{t}\right\} - \left[\mathbf{Q}\right]\left\{\Delta\overline{\mathbf{T}}^{t}\right\} + \left\{\mathbf{Y}^{t}\right\}, \tag{3.10}$$

where

$$\left\{\Delta \mathbf{T}_s^t\right\} = \left\{\Delta \mathbf{T}^{(1),t}, \Delta \mathbf{T}^{(2),t}, \cdots, \Delta \mathbf{T}^{(n),t}\right\}^{\mathsf{T}}, \tag{3.11}$$

and $\left\{\mathbf{Y}^t\right\}$ includes the zero components resulting from stress and electric field equilibrium conditions through the subcells, and the differences in the history variables from imposing displacement compatibility and electric potential continuity at the interfaces between the adjacent subcells. $\left[\mathbf{P}^t\right]$ matrix is a function of the electric fields, material parameters and the volume fraction of each subcell at current time t and the $\left[\mathbf{Q}\right]$ matrix is a constant matrix from the micromechanical relations. A fixed-point iterative method is used to minimize the above residual vector at each time step. Once the residual vector has been minimized, the increment of the independent field variable in each subcell is given as:

$$\left\{\Delta \mathbf{T}_s^t\right\} = \left[\mathbf{B}_s^t\right]\left\{\Delta \overline{\mathbf{T}}^t\right\} + \left\{\mathbf{X}_s^t\right\}, \tag{3.12}$$

where

$$\left[\mathbf{B}_s^t\right] = \left[\mathbf{P}^t\right]^{-1}\left[\mathbf{Q}\right], \tag{3.13}$$

$$\left\{\mathbf{X}_s^t\right\} = -\left[\mathbf{P}^t\right]^{-1}\left\{\mathbf{Y}^t\right\}. \tag{3.14}$$

$\left[\mathbf{B}_s^t\right]$ includes the elements of the concentration matrix $\mathbf{B}^{(\alpha),t}$, i.e.,

$$\left[\mathbf{B}_s^t\right] = \left[\mathbf{B}^{(1),t}, \mathbf{B}^{(2),t}, \cdots, \mathbf{B}^{(n),t}\right]^{\mathsf{T}}. \tag{3.15}$$

$\left\{\mathbf{X}_s^t\right\}$ consists of the history variables $\mathbf{X}^{(\alpha),t}$, i.e.,

$$\left\{\mathbf{X}_s^t\right\} = \left\{\mathbf{X}^{(1),t}, \mathbf{X}^{(2),t}, \cdots, \mathbf{X}^{(n),t}\right\}^{\mathsf{T}}. \tag{3.16}$$

Once $\mathbf{B}^{(\alpha),t}$ and $\mathbf{X}^{(\alpha),t}$ have been determined, the effective electro-mechanical properties inside $\bar{\mathbf{O}}^t$ and the field variables in $\bar{\bar{\mathbf{\Xi}}}^t$ are evaluated via Equations (3.8), and (3.1), (3.6), respectively. It is noted that different incremental independent field variables, e.g., ($\Delta\boldsymbol{\varepsilon}$, $\Delta\mathbf{E}$) can be chosen to derive the fiber- and particle-unit-cell models following a similar procedure.

3.2 Hybrid-unit-cell Model (An Incremental Formulation)

A hybrid-unit-cell model for obtaining the overall responses of hybrid composites whose constituents experience nonlinear electro-mechanical and viscoelastic behaviors is presented in this section. The microstructures of a hybrid composite are idealized with periodically distributed fibers of square cross section in a matrix medium and the microstructures of the matrix are idealized with periodically distributed cubic particles in a homogeneous viscoelastic matrix. Here, we consider a UC as the smallest representative microstructures and each UC is divided into several subcells. Figure 3.2 illustrates an idealized UC for the RVE of the hybrid composites. At the upper scale, a hybrid-UC model consists of a fiber-UC model, comprising of four fiber and matrix subcells, and the lower scale is a particle-UC model, having eight particle and polymer subcells. The particle-UC model is implemented at each matrix subcell in the fiber-UC model. The first subcell of the fiber UC is the unidirectional square fiber constituent and the rest of the subcells represent the matrix, which is a homogenized composite of the particule UCs. The first subcell of the particule UC is the cubic particle constituent and the remaining subcells in the particule UC indicate the homogeneous viscoelastic matrix. The fiber and particle UCs lead to rather simple micromechanical relations by satisfying

equilibrium condition and displacement compatibility among all subcells. The time-integration algorithm for the rate-dependent PZT (Equation (2.28)) and viscoelastic matrix (Equation (2.47)) is nested to the hybrid-unit-cell model in order to obtain approximate solutions of the overall nonlinear and time-dependent responses of the hybrid composites.

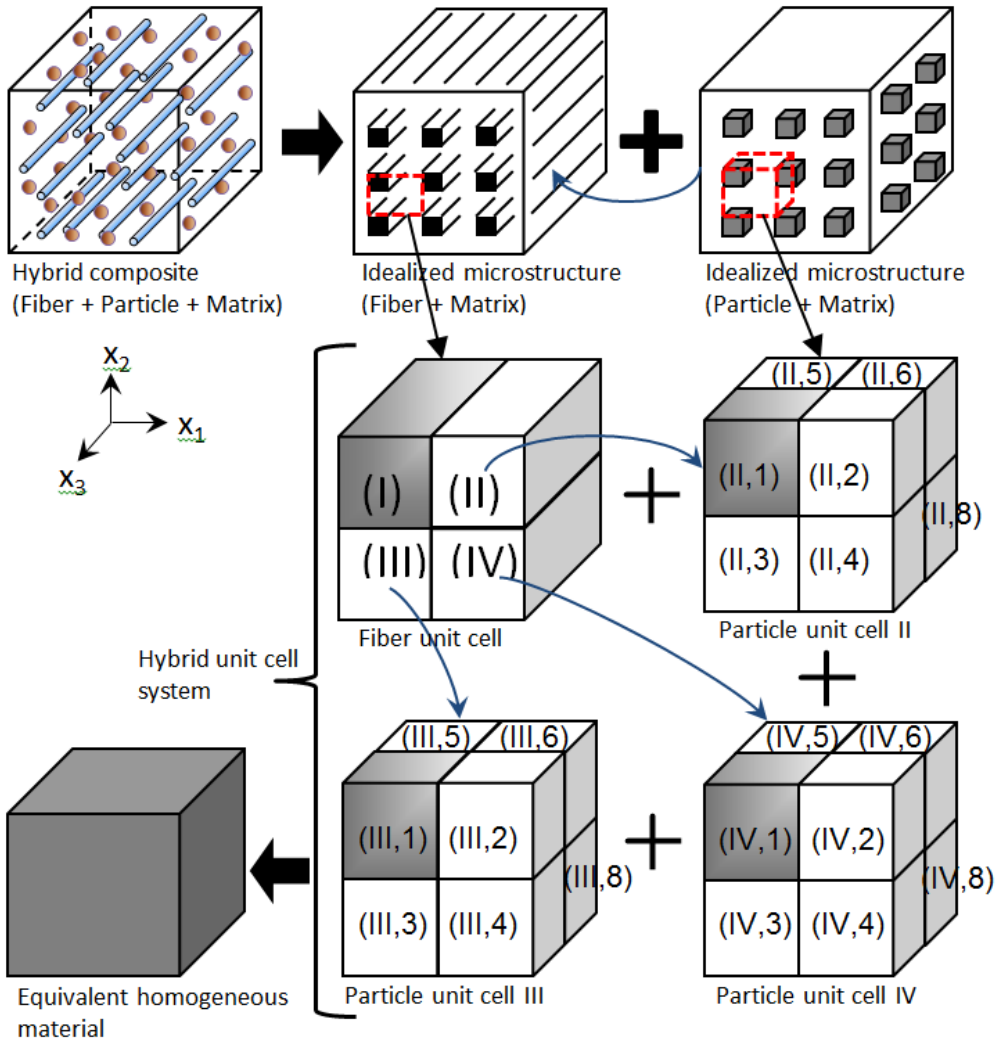

Figure 3.2 Hybrid-unit-cell model

For the derivation of the hybrid-UC model, we start with the fiber UC. Using a volume-average scheme, the effective field variable, denoted by an overbar, of the fiber UC at current time t is written as:

$$\bar{\boldsymbol{\Xi}}^{t} = \sum_{\alpha=\mathrm{I}}^{\mathrm{IV}} c^{(\alpha)} \boldsymbol{\Xi}^{(\alpha),t}. \tag{3.17}$$

The superscript (α) denotes the subcell's number of the fiber unit cell. The fiber volume fraction is defined as $c^{(\mathrm{I})} = V^{(\mathrm{I})}/V$ (i.e., volume fraction of the fibers with respect to the hybrid composite) and the fiber UC volume is given by $V = \sum_{\alpha=\mathrm{I}}^{\alpha=\mathrm{IV}} V^{(\alpha)}$. A linearized constitutive relation for the fibrous composite at current time t is written as:

$$\bar{\boldsymbol{\Xi}}^{t} = \bar{\mathbf{O}}^{t} \Delta \bar{\mathbf{T}}^{t} + \bar{\boldsymbol{\Xi}}^{t-\Delta t}, \tag{3.18}$$

and also for the subcell (α) is:

$$\boldsymbol{\Xi}^{(\alpha),t} = \mathbf{O}^{(\alpha),t} \Delta \mathbf{T}^{(\alpha),t} + \boldsymbol{\Xi}^{(\alpha),t-\Delta t}. \tag{3.19}$$

In order to relate the effective incremental independent field variables in the fiber UC to the corresponding incremental field variables in its subcells, a concentration matrix $\mathbf{B}^{(\alpha),t}$ and a vector of history variable $\mathbf{X}^{(\alpha),t}$ at current time t are defined through the following relation:

$$\Delta \mathbf{T}^{(\alpha),t} = \mathbf{B}^{(\alpha),t} \Delta \bar{\mathbf{T}}^{t} + \mathbf{X}^{(\alpha),t}. \tag{3.20}$$

Substituting $\Delta \mathbf{T}^{(\alpha),t}$ from Equation (3.20) into (3.19) gives

$$\boldsymbol{\Xi}^{(\alpha),t} = \mathbf{O}^{(\alpha),t} \mathbf{B}^{(\alpha),t} \Delta \bar{\mathbf{T}}^{t} + \mathbf{O}^{(\alpha),t} \mathbf{X}^{(\alpha),t} + \boldsymbol{\Xi}^{(\alpha),t-\Delta t}. \tag{3.21}$$

Substituting $\boldsymbol{\Xi}^{(\alpha),t}$ from Equation (3.21) into (3.17) gives

$$\overline{\boldsymbol{\Xi}}^{t} = \sum_{\alpha=\mathrm{I}}^{\mathrm{IV}} c^{(\alpha)} \mathbf{O}^{(\alpha),t} \mathbf{B}^{(\alpha),t} \Delta \overline{\mathbf{T}}^{t} + \sum_{\alpha=\mathrm{I}}^{\mathrm{IV}} c^{(\alpha)} \left(\mathbf{O}^{(\alpha),t} \mathbf{X}^{(\alpha),t} + \boldsymbol{\Xi}^{(\alpha),t-\Delta t} \right). \tag{3.22}$$

From Equations (3.22) and (3.18), the effective electro-mechanical property and history variable of the fibrous UC are:

$$\overline{\mathbf{O}}^{t} = \sum_{\alpha=1}^{\mathrm{IV}} c^{(\alpha)} \mathbf{O}^{(\alpha),t} \mathbf{B}^{(\alpha),t}. \tag{3.23}$$

$$\overline{\boldsymbol{\Xi}}^{t-\Delta t} = \sum_{\alpha=1}^{\mathrm{IV}} c^{(\alpha)} \left(\mathbf{O}^{(\alpha),t} \mathbf{X}^{(\alpha),t} + \boldsymbol{\Xi}^{(\alpha),t-\Delta t} \right). \tag{3.24}$$

The linearized constitutive model for the fiber subcell I is obtained directly from Equation (2.12). The matrix subcells II, III, and IV in the fiber unit cell consist of cubic fillers dispersed in the matrix. The electro-mechanical properties of these subcells are determined using the particle-unit-cell model, comprising of eight subcells (Figure 3.2). The average dependent field variables in the matrix subcells II, III, and IV are determined as:

$$\boldsymbol{\Xi}^{(\alpha),t} = \sum_{\beta=1}^{8} c^{(\alpha,\beta)} \boldsymbol{\Xi}^{(\alpha,\beta),t}, \quad \alpha = \mathrm{II}, \mathrm{III}, \mathrm{IV}. \tag{3.25}$$

The superscript (α,β) indicates the subcells' numbers corresponding to the particle UC (β) and fiber UC (α). The particle volume fraction is defined as $c^{(\mathrm{II},1)} = V^{(\mathrm{II},1)} / V^{(\mathrm{II})}$ (volume fraction of the filler particles in the matrix) which should be the same as $c^{(\mathrm{III},1)}$ and $c^{(\mathrm{IV},1)}$. The corresponding particle UC volumes are given by $V^{(\alpha)} = \sum_{\beta=1}^{\beta=8} V^{(\alpha,\beta)}$ with $\alpha = \mathrm{II}, \mathrm{III}, \mathrm{IV}$. The linearized constitutive relation for the particulate subcell (α,β) at current time t is:

$$\boldsymbol{\Xi}^{(\alpha,\beta),t} = \mathbf{O}^{(\alpha,\beta),t}\Delta\mathbf{T}^{(\alpha,\beta),t} + \boldsymbol{\Xi}^{(\alpha,\beta),t-\Delta t}, \quad \alpha = \text{II, III, IV}, \quad \beta = 1,2,..,8. \tag{3.26}$$

The concentration matrix $\mathbf{B}^{(\alpha,\beta),t}$ and the vector of history variable $\mathbf{X}^{(\alpha,\beta),t}$ at current time t are defined through the relation:

$$\Delta\mathbf{T}^{(\alpha,\beta),t} = \mathbf{B}^{(\alpha,\beta),t}\Delta\mathbf{T}^{(\alpha),t} + \mathbf{X}^{(\alpha,\beta),t}, \quad \alpha = \text{II, III, IV}, \quad \beta = 1,2,..,8, \tag{3.27}$$

which relates the incremental independent average field variables of the matrix subcells II, III and IV to the corresponding incremental field variables of the particle and matrix subcells. Substituting Equation (3.27) into Equation (3.26) and using the volume-average scheme in Equation (3.25), the corresponding dependent field variables for the matrix subcells are:

$$\boldsymbol{\Xi}^{(\alpha),t} = \sum_{\beta=1}^{8} c^{(\alpha,\beta)}\mathbf{O}^{(\alpha,\beta),t}\mathbf{B}^{(\alpha,\beta),t}\Delta\mathbf{T}^{(\alpha),t} + \sum_{\beta=1}^{8} c^{(\alpha,\beta)}\left(\mathbf{O}^{(\alpha,\beta),t}\mathbf{X}^{(\alpha,\beta),t} + \boldsymbol{\Xi}^{(\alpha,\beta),t-\Delta t}\right), \quad \alpha = \text{II, III, IV}. \tag{3.28}$$

Comparing Equation (3.28) to Equation (3.4) gives the overall electro-mechanical properties and history variables of the matrix subcells:

$$\mathbf{O}^{(\alpha),t} = \sum_{\beta=1}^{8} c^{(\alpha,\beta)}\mathbf{O}^{(\alpha,\beta),t}\mathbf{B}^{(\alpha,\beta),t}, \quad \alpha = \text{II, III, IV}. \tag{3.29}$$

$$\boldsymbol{\Xi}^{(\alpha),t-\Delta t} = \sum_{\beta=1}^{8} c^{(\alpha,\beta)}\left(\mathbf{O}^{(\alpha,\beta),t}\mathbf{X}^{(\alpha,\beta),t} + \boldsymbol{\Xi}^{(\alpha,\beta),t-\Delta t}\right), \quad \alpha = \text{II, III, IV}. \tag{3.30}$$

Finally, in order to evaluate the concentration matrices and history variables $\mathbf{B}^{(\alpha),t}$, $\mathbf{B}^{(\alpha,\beta),t}$ and $\mathbf{X}^{(\alpha),t}$, $\mathbf{X}^{(\alpha,\beta),t}$ in the hybrid-UC model it is necessary to use the constitutive relations for all constituents together with the linearized micromechanical relations from the fiber unit cell (**Appendix A**) and the particle unit cell (**Appendix B**). Because of the

nonlinear constitutive relations for the constituents, the linearized micromechanical relations generally violate the overall nonlinear responses, which results in the following residual vector:

$$\underset{252\times1}{\left\{\mathbf{R}^t\right\}} = \underset{252\times252}{\left[\mathbf{P}^t\right]}\underset{252\times1}{\left\{\Delta\mathbf{T}_s^t\right\}} - \underset{252\times9}{\left[\mathbf{Q}\right]}\underset{9\times1}{\left\{\Delta\bar{\mathbf{T}}^t\right\}} + \underset{252\times1}{\left\{\mathbf{Y}^t\right\}}, \tag{3.31}$$

where

$$\left\{\Delta\mathbf{T}_s^t\right\} = \left\{\Delta\mathbf{T}^{(\mathrm{I}),t},\cdots,\Delta\mathbf{T}^{(\mathrm{IV}),t},\Delta\mathbf{T}^{(\mathrm{II},1),t},\cdots,\Delta\mathbf{T}^{(\mathrm{II},8),t},\Delta\mathbf{T}^{(\mathrm{III},1),t},\cdots,\Delta\mathbf{T}^{(\mathrm{III},8),t},\Delta\mathbf{T}^{(\mathrm{IV},1),t},\cdots,\Delta\mathbf{T}^{(\mathrm{IV},8),t}\right\}^{\mathrm{T}}, \tag{3.32}$$

and $\left\{\mathbf{Y}^t\right\}$ includes the zero entities due to stress and electric field equilibrium conditions in the subcells, and the differences in the history variables from the displacement compatibility and electric displacement continuity at the interfaces between the adjacent subcells. $\left[\mathbf{P}^t\right]$ matrix is a function of the electric fields, material parameters and the volume fraction of each subcell at current time t and the $\left[\mathbf{Q}\right]$ matrix is a constant matrix from the micromechanical relations. The dimension of each matrix is denoted on its bottom. A fixed-point iterative method is used to minimize the above residual vector at each time step. Once the residual vector has been minimized, the increment of the independent field variable in each subcell is given as:

$$\left\{\Delta\mathbf{T}_s^t\right\} = \left[\mathbf{B}_s^t\right]\left\{\Delta\bar{\mathbf{T}}^t\right\} + \left\{\mathbf{X}_s^t\right\}, \tag{3.33}$$

where

$$\left[\mathbf{B}_s^t\right] = \left[\mathbf{P}^t\right]^{-1}\left[\mathbf{Q}\right], \tag{3.34}$$

$$\left\{\mathbf{X}_s^t\right\} = -\left[\mathbf{P}^t\right]^{-1}\left\{\mathbf{Y}^t\right\}. \tag{3.35}$$

$\left[\mathbf{B}_s^t\right]$ comprises the elements of the concentration matrices $\mathbf{B}^{(\alpha),t}$ and $\mathbf{B}^{(\alpha,\beta),t}$, i.e.,

$$\left[\mathbf{B}_s^t\right]=\left[\mathbf{B}^{(\mathrm{I}),t},\cdots,\mathbf{B}^{(\mathrm{IV}),t},\mathbf{B}^{(\mathrm{II},1),t},\cdots,\mathbf{B}^{(\mathrm{II},8),t},\mathbf{B}^{(\mathrm{III},1),t},\cdots,\mathbf{B}^{(\mathrm{III},8),t},\mathbf{B}^{(\mathrm{IV},1),t},\cdots,\mathbf{B}^{(\mathrm{IV},8),t}\right]^{\mathsf{T}}. \tag{3.36}$$

$\left\{\mathbf{X}_s^t\right\}$ includes the history variables $\mathbf{X}^{(\alpha),t}$ and $\mathbf{X}^{(\alpha,\beta),t}$, i.e.,

$$\left\{\mathbf{X}_s^t\right\}=\left\{\mathbf{X}^{(\mathrm{I}),t},\cdots,\mathbf{X}^{(\mathrm{IV}),t},\mathbf{X}^{(\mathrm{II},1),t},\cdots,\mathbf{X}^{(\mathrm{II},8),t},\mathbf{X}^{(\mathrm{III},1),t},\cdots,\mathbf{X}^{(\mathrm{III},8),t},\mathbf{X}^{(\mathrm{IV},1),t},\cdots,\mathbf{X}^{(\mathrm{IV},8),t}\right\}^{\mathsf{T}}. \tag{3.37}$$

Once $\mathbf{B}^{(\alpha),t}$, $\mathbf{B}^{(\alpha,\beta),t}$, $\mathbf{X}^{(\alpha),t}$ and $\mathbf{X}^{(\alpha,\beta),t}$ have been determined, the effective electro-mechanical property $\bar{\mathbf{O}}^t$ and the field variable $\bar{\bar{\boldsymbol{\Xi}}}^t$ are evaluated via Equations (3.8), (3.29) and (3.1), (3.6), (3.29), (3.30), respectively. It is noted that different incremental independent field variables, e.g., ($\Delta\boldsymbol{\varepsilon}$, $\Delta\mathbf{E}$) can be chosen to derive the hybrid-UC model following a similar procedure.

3.3 Mori-Tanaka Model with Correspondence Principle (A Total Formulation)

A reformulation of Mori-Tanaka micromechanical model is done in order to estimate the overall responses of 1-3 and 0-3 polarized piezocomposites, whose piezoceramic inhomogeneities are modeled with higher order electromechanical constitutive model proposed by Tiersten (1993), while the polymeric matrix is assumed linear viscoelastic. There exists certain correspondence between the elastic and viscoelastic solutions of an initial-boundary value problem. Discussion and limitation on using the correspondence principle for linear viscoelastic problems can be found in Christensen (1982) and Rajagopal and Wineman (2008). Since the constitutive relation of the polymeric matrix is linear viscoelastic (i.e., Equation (2.47)) and the model for the

polarized piezoceramic inhomogeneities is field-dependent but time-independent, i.e., constitutive Equations (2.1), (2.2), (2.3), and (2.4), the correspondence principle is applicable through the use of the Laplace-Carson transform (see Laws and McLaughlin, 1978)

$$\hat{f}(s) = s\int_0^{\infty} \exp[-st] f(t) dt, \tag{3.38}$$

where the hat indicates the transformed function of the time-dependent function $f(t)$ and s is the transform variable. Equation (2.47) in a transformed domain is written as

$$\hat{\varepsilon}_{ij} = (1+\nu)\hat{D}\hat{S}_{ij} + \frac{(1-2\nu)}{3}\delta_{ij}\hat{D}\hat{\sigma}_{kk}, \tag{3.39}$$

which is mathematically similar to the constitutive relation for a linear elastic isotropic material. Detailed discussions on the Laplace-Carson transform for viscoelastic problems for composite materials can be found in Li et al. (2006). Via the correspondence principle, the micromechanical models developed for the elastic problems can be expressed in the transformed domain for the corresponding viscoelastic problems. A total formulation in terms of linearized relations of the nonlinear polarized piezoelectric constitutive relations (Equations (2.1) and (2.2)) is chosen and written as:

$$\Xi_{iJ} = O_{iJMn}\, T_{Mn}, \tag{3.40}$$

where

$$\Xi_{iJ} = \begin{cases} \varepsilon_{ij}, & J = 1,2,3, \\ D_i, & J = 4, \end{cases} \tag{3.41}$$

$$O_{iJMn} = \begin{cases} \tilde{s}_{ijmn}, & J, M = 1,2,3, \\ \tilde{d}'_{nij}, & J = 1,2,3;\ M = 4, \\ \tilde{d}_{imn}, & J = 4;\ M = 1,2,3, \\ \tilde{\kappa}_{in}, & J, M = 4, \end{cases} \tag{3.42}$$

$$T_{Mn} = \begin{cases} \sigma_{mn}, & M = 1,2,3, \\ E_n, & M = 4. \end{cases} \tag{3.43}$$

The components, $\tilde{s}_{ijmn}$, $\tilde{d}'_{nij}$, $\tilde{d}_{imn}$, and $\tilde{\kappa}_{in}$, in Equation (3.42) are:

$$\tilde{s}_{ijmn} = s_{ijmn}, \tag{3.44}$$

$$\tilde{d}'_{nij} = d_{nij} + \frac{1}{2} f_{nlij} E_l, \tag{3.45}$$

$$\tilde{d}_{imn} = d_{imn}, \tag{3.46}$$

$$\tilde{\kappa}_{in} = \kappa_{in} + \frac{1}{2} \chi_{ink} E_k. \tag{3.47}$$

For a two-phase polarized piezocomposite, the volume-average field variables in transformed domain are written as

$$\hat{\bar{\mathbf{T}}} = \sum_{r=0}^{1} c_r \hat{\mathbf{T}}_r, \tag{3.48}$$

$$\hat{\bar{\boldsymbol{\Xi}}} = \sum_{r=0}^{1} c_r \hat{\boldsymbol{\Xi}}_r, \tag{3.49}$$

where c_r is volume fraction of the r^{th} phase and the overbar denotes the volume average of a given term. $r = 0$ indicates the polymeric matrix and $r = 1$ represents the polarized piezoceramic inhomogeneity. In an average sense, the transformed constitutive relation for the polarized piezocomposite is expressed as

$$\hat{\bar{\boldsymbol{\Xi}}} = \hat{\bar{\mathbf{O}}}\hat{\bar{\mathbf{T}}}, \tag{3.50}$$

and for the r^{th} phase is

$$\hat{\boldsymbol{\Xi}}_r = \hat{\mathbf{O}}_r \hat{\mathbf{T}}_r. \tag{3.51}$$

where the effective generalized compliance $\hat{\bar{\mathbf{O}}}$ will be determined in terms of a concentration tensor that relates the average field variables and field variables in each phase. Following Hill (1963), if the RVE in a composite can be defined, there is a unique dependence of the average field variables in the r^{th} phase upon the overall field variables in the polarized piezocomposite. This dependence is defined using a transformed concentration tensor $\hat{\mathbf{B}}_r$:

$$\hat{\mathbf{T}}_r = \hat{\mathbf{B}}_r \hat{\bar{\mathbf{T}}}. \tag{3.52}$$

Using Equations (3.48)-(3.52), the effective generalized compliance of the polarized piezocomposite in transformed domain is

$$\hat{\bar{\mathbf{O}}} = \sum_{r=0}^{1} c_r \hat{\mathbf{O}}_r \hat{\mathbf{B}}_r. \tag{3.53}$$

The transformed concentration tensor of the MT model is

$$\hat{\mathbf{B}}_r = \hat{\mathbf{B}}_r^{dil} \left[c_0 \mathbf{I} + c_1 \hat{\mathbf{B}}_1^{dil} \right]^{-1}, \tag{3.54}$$

where

$$\hat{\mathbf{B}}_r^{dil} = \left[\mathbf{I} + \hat{\mathbb{S}}_r \hat{\mathbf{O}}_0^{-1} \left(\hat{\mathbf{O}}_r - \hat{\mathbf{O}}_0 \right) \right]^{-1}. \tag{3.55}$$

Detailed formulations of the MT model can be found in Mori and Tanaka (1973), Weng (1984) and Benvensite (1987). In Equations (3.54) and (3.55) $\mathbf{I}$ is the combination of the

second- and fourth-order identity tensors, and $\hat{\mathbb{S}}_r$ is the transformed Eshelby's tensor of the r^{th} phase. Since the geometries of inhomogeneities considered here are unidirectional fibers with circular cross section or spherical particles and the corresponding elastic matrix is isotropic, Eshelby's tensor will only depend on Poisson's ratio of the corresponding viscoelastic matrix. Furthermore, due to the time-independent Poisson's ratio for the polymeric matrix (see Equation (2.47)), the transformed Eshelby's tensor is identical to the one for the elastic matrix, i.e.,

$$\hat{\mathbb{S}}_r = \mathbb{S}_r. \tag{3.56}$$

Equation (3.56) greatly simplifies the evaluation of the transformed concentration tensor $\hat{\mathbf{B}}_r$ in Equation (3.54). Evaluation of Eshelby's tensors for polarized piezocomposites with linear elastic matrix can be found in Dunn and Taya (1993b) in which the independent field variable pair ($\boldsymbol{\varepsilon}$, $\mathbf{E}$) were used to derive Eshelby's tensors, while for the Equation (3.55) the independent field variable pair ($\boldsymbol{\sigma}$, $\mathbf{E}$) is chosen. A useful procedure to formulate Eshelby's tensors from different independent field variable pair was provided by Li and Dunn (2001b). Due to the nonlinear responses of the polarized piezoelectric inhomogeneities, the linearization procedure provided in Equation (3.40) leads to an implicit problem: $\hat{\mathbf{B}}_r$ depends on the linearized property $\hat{\mathbf{O}}_r$ and the linearized property is a function of $\hat{\mathbf{T}}_r$, which also depends on $\hat{\mathbf{B}}_r$. This implicit problem can be expressed in a residual vector using Equation (3.52) and it should be defined at current time t:

$$\left\{\mathbf{R}^{t}\right\} = \mathcal{L}^{-1}\begin{Bmatrix}\hat{\mathbf{T}}_0 - \hat{\mathbf{B}}_0\hat{\bar{\mathbf{T}}} \\ \hat{\mathbf{T}}_1 - \hat{\mathbf{B}}_1\hat{\bar{\mathbf{T}}}\end{Bmatrix}, \tag{3.57}$$

where the operator $\mathcal{L}^{-1}$ is the inversion of Laplace-Carson transform of a given transformed function $\hat{f}(s)$ and defined as

$$\mathcal{L}^{-1}\left[\hat{f}(s)\right] = \frac{1}{2\pi i}\int_{\gamma-i\infty}^{\gamma+i\infty}\frac{\hat{f}(s)}{s}\exp[st]ds, \tag{3.58}$$

In Equation (3.57), the error should be corrected at each instant of time t. A trial solution for the unknown $\mathbf{T}_r$ together with a fixed-point iterative method is used to minimize the residual vector at each time step. Once the residual vector has been minimized, the transformed concentration tensor $\hat{\mathbf{B}}_r$, the fields $\hat{\mathbf{T}}_r$ and $\hat{\boldsymbol{\Xi}}_r$ in each phase, the effective generalized compliance $\hat{\bar{\mathbf{O}}}$ and the effective field $\hat{\bar{\boldsymbol{\Xi}}}$ for the piezocomposite can be determined from Equations (3.54), (3.52), (3.51), (3.53) and (3.49), respectively; and further, using the inverse Laplace-Carson transform to obtain the corresponding field variables at each time step. In Equation (3.58), the integration is solved by the Cauchy residue theorem. When the expression for $\hat{f}(s)/s$ is rather complicated, it might not be possible to analytically evaluate the integral in Equation (3.58). A numerical method based on a special sequence acceleration of the Gaver functional, recently developed by Abate and Valkó (2004), is used in the current study in order to evaluate the Laplace-Carson inversion. It is noted that different independent field variables, e.g., ($\boldsymbol{\varepsilon}$, $\mathbf{E}$) can be chosen to reformulate MT model following a similar procedure.

CHAPTER IV

NONLINEAR ELECTRO-MECHANICAL ANALYSES OF POLARIZED 1-3 AND 0-3 PIEZOCOMPOSITES[6]

This chapter presents the overall response of the fiber and particle-unit-cell models formulated in Chapter III. The overall electro-mechanical responses from the UC models are compared to experimental data available in literature followed by parametric studies in order to examine the effects of shapes and compositions of the constituents, and prescribed boundary conditions on the overall time-dependent and nonlinear electromechanical responses of polarized 1-3 and 0-3 piezocomposites. The constitutive relations in Equations (2.1), (2.2), (2.3), and (2.4) are used for the polarized piezoceramics while those in Equations (2.47) and (2.48) are considered for the inactive viscoelastic mediums. MT estimations are also presented for comparison purpose.

4.1 Comparison with Experimental Data

Most of experimental data for piezocomposites with polarized piezoelectric fiber or particle inhomogeneities embedded in a polymeric matrix consider mainly linear electromechanical responses. The fiber and particle-unit-cell models with nonlinear and

[6] Parts of this chapter are taken from: Lin, C.-H., and A. Muliana. 2013a. "Micromechanics Models for the Effective Nonlinear Electro-mechanical Responses of Piezoelectric Composites," *Acta Mech.*, 224(7):1471-1492 and reprinted with permission of Springer Publishing, Inc. Copyright 2013 by Springer Publishing, Inc. and from: Lin, C.-H., and A. Muliana. 2013b. "Micromechanical Models for the Effective Time-dependent and Nonlinear Electromechanical Responses of Piezoelectric Composites," *J Intel. Mat. Syst. Str.*, doi:10.1177/1045389X13504477 and reprinted with permission of Sage Publications, Inc. Copyright 2013 by Sage Publications, Inc.

time-dependent responses should be capable in predicting the overall linear electromechanical properties of piezocomposites. Chan and Unsworth (1989) experimentally studied responses of the polarized 1-3 piezocomposite with continuous polarized PZT-7A fibers embedded in an Araldite D matrix. The properties of the constituents, which are reported by Dunn and Taya (1993a) and Chan and Unsworth (1989), are listed in Table 4.1.

Table 4.1 Electro-mechanical material properties for the PZT-7A and Araldite D

	c_{1111} GPa	c_{1122} GPa	c_{1133} GPa	c_{3333} GPa	c_{2323} GPa	d_{311} pm/V	d_{333} pm/V	d_{113} pm/V	$\frac{\kappa_{11}}{\kappa_0}$ [c]	$\frac{\kappa_{33}}{\kappa_0}$
PZT-7A [a]	148	76.2	74.2	131	25.4	−60	150	362	840	460
Araldite D [b]	8	4.4	4.4	8	1.8	0	0	0	4	4

[a] Dunn and Taya (1993a). Transversely isotropic PZT-7A with longitudinal axis and poling direction along the x_3-axis.
[b] Chan and Unsworth (1989). Elastic (instantaneous) isotropic properties.
[c] $\kappa_0 = 8.85\times10^{-12}$ (F/m) denotes vacuum permittivity.

Chan and Unsworth (1989) discussed that the manufacturer's data of the bulk electromechanical properties of the polarized PZT-7A vary significantly from different samples. For example, d_{333} for polarized PZT-7A is 150 pm/V in the data sheet but the measured value is randomly between 163-167 pm/V. The piezoelectric strain coefficient d_{333} to 167 pm/V based on a measured value is used for the numerical prediction. The

numerical results from the UC and MT models together with SC model[7] comparing with experimental data are shown in Figure 4.1. For the effective piezoelectric strain coefficient $\overline{d}_{333}$ and the relative permittivity $\overline{\kappa}_{33}/\kappa_0$ shown in Figure 4.1a and Figure 4.1b, respectively. The predictions from the micromechanics models are in good agreements with the experimental data over the range of volume fractions considered. For the coupling parameter $\overline{k}_p$ and compliance $\overline{s}_{1111}+\overline{s}_{1122}$ shown in Figure 4.1c and Figure 4.1d, respectively, the UC and MT models give nearly identical estimations but the predictions from the SC model slightly deviate from the ones obtained using the UC and MT models. These discrepancies are probably due to the large contrast in the properties of the inhomogeneity and matrix constituents. In such situation, the SC model overestimates the inhomogeneity interaction especially for higher inhomogeneity volume fractions.

[7] For the purpose of comparison, the predictions using the self-consistent (SC) model are presented only for linear piezoelectric constitutive relations. The transformed concentration tensor of the SC model is $\hat{\mathbf{B}}_r^{SC}=\left[\mathbf{I}+\hat{\overline{\mathbb{S}}}_r\hat{\overline{\mathbf{O}}}^{-1}\left(\hat{\mathbf{O}}_r-\hat{\overline{\mathbf{O}}}\right)\right]^{-1}$. An overbar on the transformed Eshelby's tensor indicates that its components are evaluated by using the effective transformed generalized compliance $\hat{\overline{\mathbf{O}}}$ instead of the transformed generalized compliance of the matrix $\hat{\mathbf{O}}_0$.

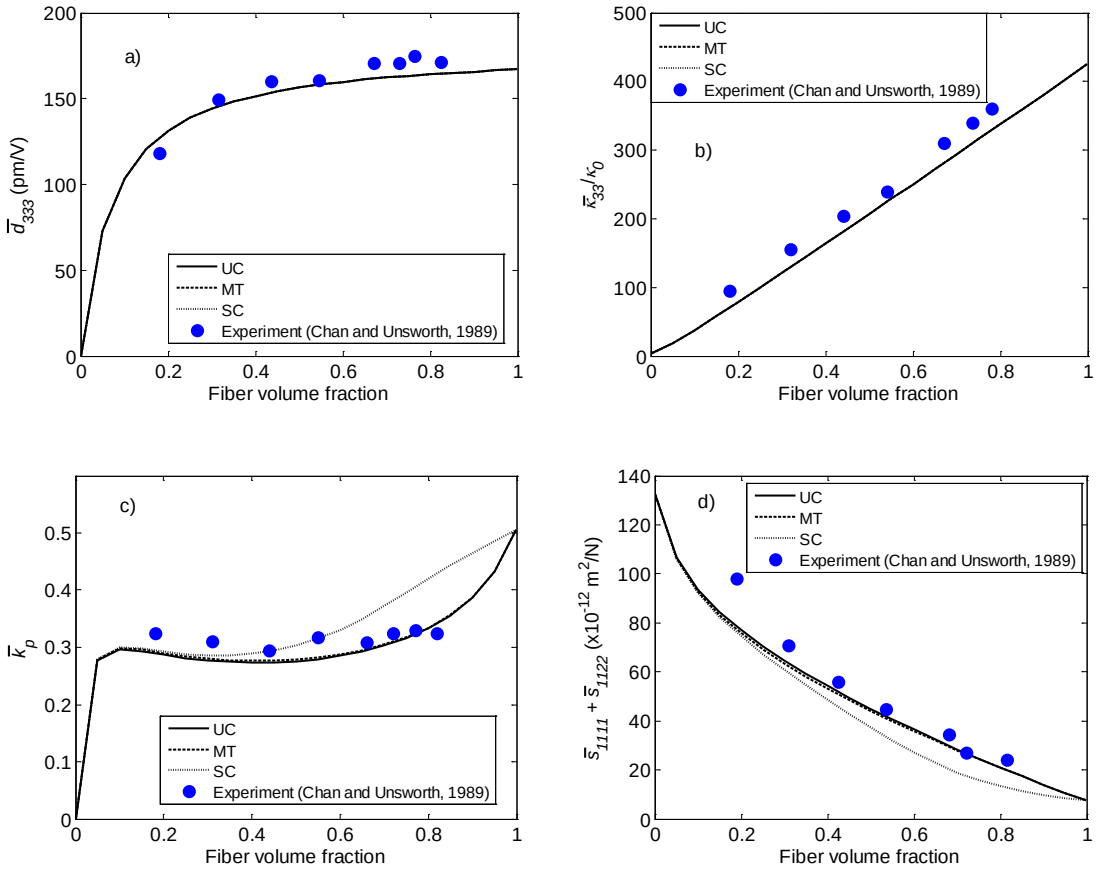

Figure 4.1 Comparison of various micromechanical predictions to the experimental data (Chan and Unsworth, 1989) for the effective a) piezoelectric strain coefficient $\bar{d}_{333}$, b) relative permittivity $\bar{\kappa}_{33}/\kappa_0$, c) coupling parameter $\bar{k}_p = [(1-\bar{\kappa}^{\varepsilon}_{33}\bar{c}^{D}_{3333})/\bar{\kappa}_{33}\bar{c}_{3333}]^{0.5}$, and d) compliance $\bar{s}_{1111}+\bar{s}_{1122}$ for the PZT-7A/Araldite D polarized 1-3 piezocomposite as a function of polarized PZT-7A fiber VF. c^{D}_{ijkl} is the elastic stiffness at a constant reference electric displacement.

Figure 4.2 depicts the micromechanical predictions of the polarized 0-3 piezocomposite, which was experimentally studied by Furukawa et al. (1976). The polarized 0-3 piezocomposite consists of spherical polarized PZT-5 particles embedded in an epoxy I medium. The properties of the constituents used for the numerical

prediction was reported by Dunn and Taya (1993a) and are listed in Table 4.2. The UC and MT predictions are nearly identical for the entire range of particle volume fractions and the MT estimation gives the closest agreement with the experimental data up to around 0.3 particle volume fraction. Again, the SC prediction significantly deviates from the UC and MT estimations at higher particle volume fractions.

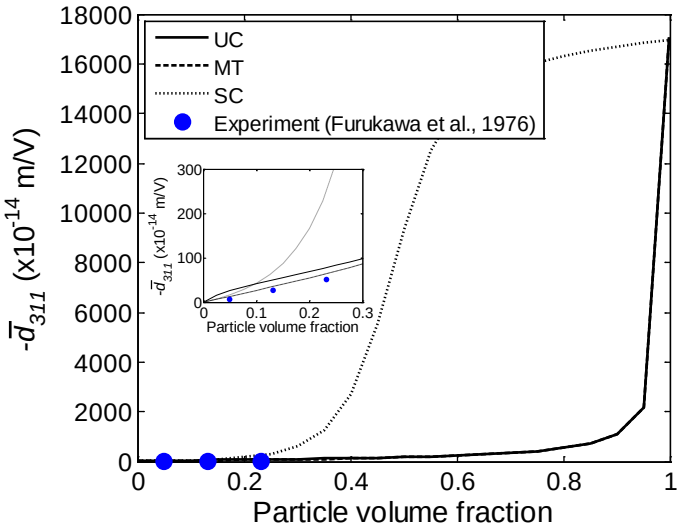

Figure 4.2 Comparison of various micromechanical predictions to the experimental data (Furukawa et al., 1976) for the effective piezoelectric strain coefficient $-\bar{d}_{311}$ for the PZT-5/epoxy I polarized 0-3 piezocomposite as a function of polarized PZT-5 particle VF.

Table 4.2 Electro-mechanical material properties for the PZT-5 and Epoxy I

	c_{1111} GPa	c_{1122} GPa	c_{1133} GPa	c_{3333} GPa	c_{2323} GPa	d_{311} pm/V	d_{333} pm/V	d_{113} pm/V	$\frac{\kappa_{11}}{\kappa_0}$	$\frac{\kappa_{33}}{\kappa_0}$
PZT-5 [a]	121	75.4	75.2	111	21.1	−171	374	584	1700	1730
Epoxy I [b]	8	4.4	4.4	8	1.8	0	0	0	4.2	4.2

[a] Dunn and Taya (1993a). Transversely isotropic PZT-5 with poling direction along the x_3-axis.

[b] Dunn and Taya (1993a). Elastic (instantaneous) isotropic properties.

Another experiment was conducted by Zeng et al. (2002) to investigate the effective relative dielectric constant $\bar{\kappa}_{33}/\kappa_0$ of the polarized 0-3 piezocomposite with spherical polarized PZTs (Navy type II) particles embedded in a P(VDF-TrFE) matrix. The properties of the composition, which were reported by Zeng et al. (2002) and by manufacturer's data sheet for the polarized PZT (Navy type II) powder PKI502 supplied by Piezo Kinetics, are listed in Table 4.3. Figure 4.3 shows that the agreement of the UC and MT estimations and experimental findings is quite good. SC prediction deviates from the UC and MT estimations at higher particle volume fractions. In general, the effective properties of the composites obtained from the UC and MT models match very well and give good predictions of the experimental data. Since, the experimental data for polarized piezocomposites that show the time-dependent behaviors are not available to validate the overall nonlinear time-dependent electromechanical responses of polarized piezocomposites, to examine the effects of viscoelastic matrices on the overall nonlinear

electromechanical responses of polarized piezocomposites, we conduct parametric studies (Section 4.2).

Table 4.3 Electro-mechanical material properties for the PZT (Navy Type II) and P(VDF-TrFE)

	c_{1111} GPa	c_{1122} GPa	c_{1133} GPa	c_{3333} GPa	c_{2323} GPa	d_{311} pm/V	d_{333} pm/V	d_{113} pm/V	$\frac{\kappa_{11}}{\kappa_0}$	$\frac{\kappa_{33}}{\kappa_0}$
PZT (Navy type II) [a]	98.2	44.1	44.1	98.2	27	−175	400	580	1800	1800
P(VDF-TrFE) [b]	4.8	3.2	3.2	4.8	0.8	0	0	0	9.9	9.9

[a] Manufacturer's data sheet for powder PKI502 supplied by Piezo Kinetics. Transversely isotropic PZT (Navy type II) with poling direction along the x_3-axis.
[b] Zeng et al. (2002). Elastic isotropic properties.

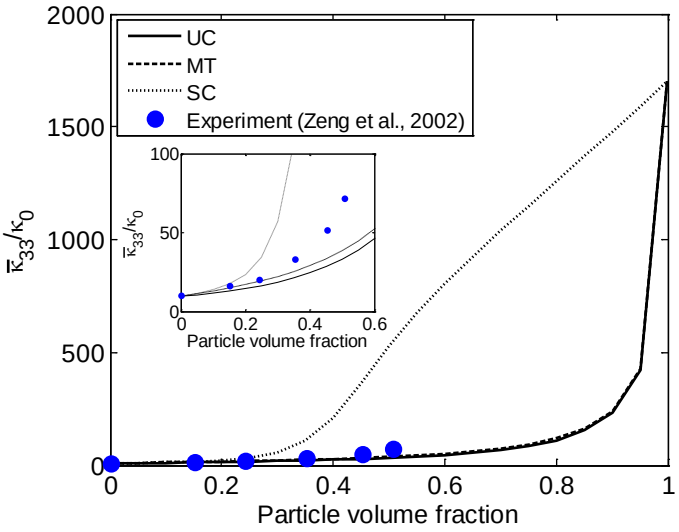

Figure 4.3 Comparison of various micromechanical predictions to the experimental data (Zeng et al., 2002) for the effective relative permittivity $\bar{\kappa}_{33}/\kappa_0$ for the PZT (Navy type II)/P(VDF-TrFE) polarized 0-3 piezocomposite as a function of polarized PZT (Navy type II) particle VF.

4.2 Parametric Studies

Since the experimental data for polarized piezocomposites that show nonlinear or time-dependent behavior are currently not available, to examine the effects of shapes and compositions of the inclusions, and prescribed boundary conditions on the overall time-dependent and nonlinear electromechanical responses of polarized 1-3 and 0-3 piezocomposites, parametric studies are conducted.

As the illustration in Figure 1.1, polarized PZT-G1195 exhibits strong nonlinearity when subject to a high electric field stimulation. Thus, the following polarized PZT-G1195 is considered for the active inclusions in the 1-3 and 0-3 piezocomposites. The properties of the polarized PZT-G1195 ceramic are obtained from

Crawley and Anderson's (1990) experiment. The nonlinear response with $d_{311} = d_{322} =$ -180 pm/V and $f_{3311} = f_{3322} = -6\times10^{-16}$ m^2/V^2 match the experimental data in Figure 1.1. The manufacturer's specifications for the remaining properties of the polarized PZT-G1195 (poling direction is along x_3-axis) are $c_{1111} = 63$, $c_{3333} = 49$ and $c_{1313} = 22$ GPa, $d_{333} = 360$ and $d_{113} = 540$ pm/V, $\kappa_{11}/\kappa_0 = 1700$ and $\kappa_{33}/\kappa_0 = 1700$ which can be found in Anderson (1989) and in order to complete the material properties for the numerical simulations we further assume[8] $c_{1122} = 34$ and $c_{1133} = 31$ GPa, $f_{3333} = 12\times10^{-16}$ and $f_{2223} =$ $f_{1113} = 18\times10^{-16}$ m^2/V^2, $\chi^{\varepsilon}_{111} = \chi^{\varepsilon}_{222} = \chi^{\varepsilon}_{333} = 0$ F/V.

4.2.1 Nonlinear responses of polarized 1-3 and 0-3 piezocomposites

Figure 4.4 shows the effective transverse strain $\overline{\varepsilon}_{11}$ and longitudinal strain $\overline{\varepsilon}_{33}$ due to an applied electric field $\overline{E}_3$ along the poling direction up to 1 MV/m for a stress free polarized 1-3 piezocomposite with polarized PZT-G1195 fiber VF = 0.5 in an Araldite D matrix. There are significant differences in the effective responses when the nonlinear

---

[8] The elastic constants at a constant reference electric field $c_{1111} = 63$, $c_{3333} = 49$ are determined by taking $\nu_{12} = 0.332$, $\nu_{13} = 0.423$ and $\nu_{31} = 0.320$, which are common for polarized PZT materials. The ratios of the fourth order to the third order piezoelectric strain coefficients are assumed to be the same for all other components (i.e., $f_{3333} = (d_{333}/d_{311})\, f_{3311}$ and $f_{1113} = (d_{113}/d_{311})\, f_{3311}$). In order to determine the nonlinear parameters it is necessary to have experimental data available for each direction. With limited data available, we believe keeping the same ratios would be a reasonable assumption. Crawley and Anderson (1990) did not equally provide the nonlinear electric displacement responses of the polarized PZT-G1195 due to electric field inputs and also we did not find any comparable experimental data for the polarized PZT-G1195 in literatures, the third-order dielectric coefficient χ^{ε}_{ijk} measured at a constant reference strain is assumed zero in this study. Because χ_{ijk} and χ^{ε}_{ijk} have the relation, $\chi_{ijk} = \chi^{\varepsilon}_{ijk} + e_{imn}\, f_{ikmn}$ (refer to Equation (2.9)), χ_{ijk} is non-zero due to non-zero terms, e_{imn} and f_{ikmn}, for the polarized PZT-G1195.

(solid lines) and linear (dotted lines) responses are considered especially for high electric field. For both the linear and nonlinear case the UC and MT predictions match very well.

For a stress free polarized 0-3 piezocomposite with polarized PZT-G1195 particle VF = 0.5 in an Araldite D matrix subject to an applied electric field $\overline{E}_3$ up to 1 MV/m, the effective actuation strains $\overline{\varepsilon}_{11}$ and $\overline{\varepsilon}_{33}$ are shown in Figure 4.5. The UC and MT models result in similar responses for both linear and nonlinear cases. This is due to the fact that in the 0-3 piezocomposite the elastic matrix dominates the overall responses of the 0-3 piezocomposite. In contrast to the 1-3 piezocomposite the nonlinear polarized piezoelectric fiber dominates the overall responses (Figure 4.4).

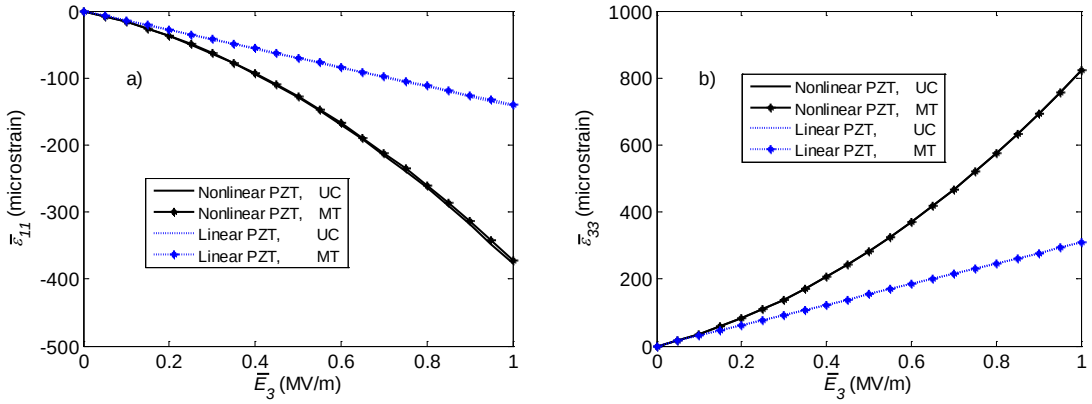

Figure 4.4 Effective a) transverse strain $\overline{\varepsilon}_{11}$ and b) longitudinal strain $\overline{\varepsilon}_{33}$ responses for the stress free PZT-G1195/Araldite D polarized 1-3 piezocomposite with polarized PZT-G1195 fiber VF = 0.5 due to an applied electric field $\overline{E}_3$ along the poling direction.

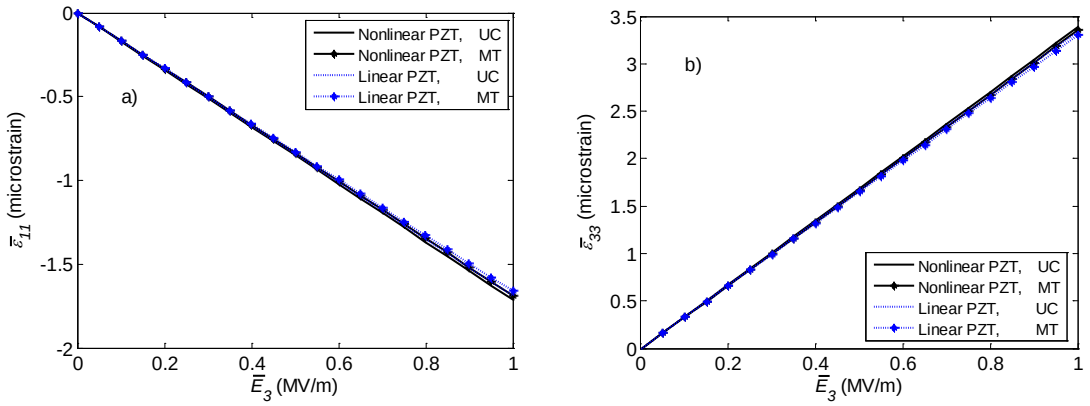

Figure 4.5 Effective a) transverse strain $\bar{\varepsilon}_{11}$ and b) longitudinal strain $\bar{\varepsilon}_{33}$ responses for the stress free PZT-G1195/Araldite D polarized 0-3 piezocomposite with polarized PZT-G1195 particle VF = 0.5 due to an applied electric field $\bar{E}_3$ along the poling direction.

The effective transverse strains $\bar{\varepsilon}_{11}$ from the UC and MT models at an electric field E_3 = 1 MV/m applied to stress free polarized 1-3 and 0-3 piezocomposites are plotted as a function of polarized piezoelectric fiber and particle volume fractions, as shown in Figure 4.6. For the polarized 1-3 piezocomposite there are significant differences between the linear and nonlinear responses (see Figure 4.6a) even for low fiber volume fractions. When the polarized 1-3 piezocomposite are subjected to large electric fields, a small amount of polarized piezoelectric fibers can induce feasible changes in the overall responses of the polarized piezocomposites. For the polarized 0-3 piezocomposite, the differences between the linear and nonlinear responses are noticeable only when the volume contents of polarized piezoelectric particles are relatively high (see Figure 4.6b). It is noted that only a small fraction of the applied

electric field reaches the polarized piezoelectric particles as the elastic matrix with low dielectric constant dominates the response. However, when the dielectric constants of the matrix are relatively high, more pronounced electro-mechanical coupling responses are observed in the particle composites. For example a conductive metal, i.e., silver, is considered as homogeneous matrix in 0-3 polarized piezocomposites. Dielectric constants of conductive metals, in general, are considered as infinite. For comparison and simulation purpose, we assume the silver matrix has relatively high dielectric constant, i.e., 89×10^{-9} F/m (i.e., ten thousand times of vacuum permittivity). The properties of the silver are referred to Davis (1998) and are listed in Table 4.4. The effective transverse strains $\overline{\varepsilon}_{11}$ from the UC and MT models at an electric field $E_3 = 1$ MV/m applied to stress free PZT-G1195/Silver polarized 0-3 piezocomposites are plotted as a function of polarized piezoelectric particle volume fractions, as shown in Figure 4.7. Significant differences in the responses are observed in the linear and nonlinear cases even for lower polarized piezoelectric particle volume fraction. The UC and MT models, in general, give close predictions of the effective electromechanical coupling response. The fiber- and particle-UC models presented in this study are shown capable of capturing the nonlinear electromechanical responses of active composites.

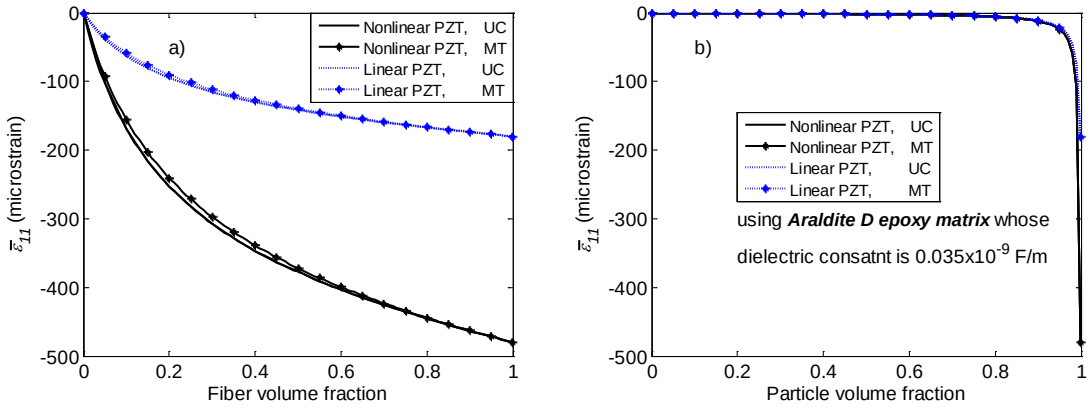

Figure 4.6 Effective strain $\bar{\varepsilon}_{11}$ responses for the stress free PZT-G1195/Araldite D polarized a) 1-3 and b) 0-3 piezocomposites at an applied electric field $\bar{E}_3$ = 1 MV/m along the poling direction as a function of polarized PZT-G1195 inhomogeneity VF.

Table 4.4 Mechanical and electrical properties of the silver (Davis, 1998)

	Silver
Young's modulus, E (GPa)	74
Poisson's ratio, ν	0.37
Dielectric coefficient[a], $\kappa_{11} = \kappa_{22} = \kappa_{33}$ (nF/m)	89

[a] This dielectric coefficient which is ten thousand times of vacuum permittivity is assumed for comparison and simulation purpose because dielectric constants of conductive metals, in general, are considered as infinite.

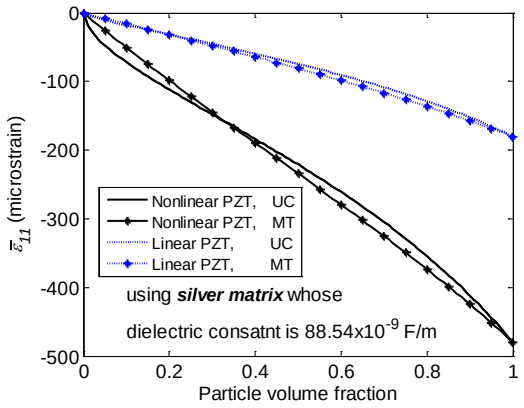

Figure 4.7 Effective strain $\bar{\varepsilon}_{11}$ responses for the stress free PZT-G1195/Silver polarized 0-3 piezocomposites at an applied electric field $\bar{E}_3$ = 1 MV/m along the poling direction as a function of polarized PZT-G1195 inhomogeneity VF.

4.2.2 Time-dependent responses of polarized 1-3 and 0-3 piezocomposites

Figure 4.8 shows the effective time-dependent strains[9] for a PZT-G1195/934 epoxy polarized 1-3 piezocomposite due to constant electric fields $\bar{E}_3$ =1 and 0.75 MV/m applied along the poling direction, which is along the longitudinal axis, i.e., x_3 -axis, of the polarized piezoelectric fiber. The property of the viscoelastic 934 epoxy is listed in Table 4.5. The 1-3 piezocomposite has polarized PZT-G1195 fiber with VF = 0.5 and is unconstrained on its surfaces. It is seen that there are significant differences in the effective time-dependent strains between the nonlinear (solid lines) and linear (dotted lines) electromechanical constitutive relations. More pronounced nonlinear responses are

[9] The time-dependent effective strains are due to the viscoelastic matrix. The electric field-induced internal stresses to the piezoelectric inhomogeneities and viscoelastic matrix due maintaining compatibility conditions for the overall deformations.

shown when higher electric field ($\bar{E}_3$ =1 MV/m) is applied, which is expected. For the longitudinal strains $\bar{\varepsilon}_{33}$ in Figure 4.8a, the UC and MT predictions are almost on top of each other. This indicates that the effect of fiber geometries on the longitudinal strains is negligible, while for the transverse time-dependent strains $\bar{\varepsilon}_{11}$ in Figure 4.8b, the mismatches between the UC and MT estimations could be associated to the fiber geometries. It is noted that the UC and MT predictions for the effective initial piezoelectric strain coefficients $\bar{d}_{311}$ are slightly different while for the $\bar{d}_{333}$ they are nearly same, as illustrated in Figure 4.9. For the polarized 1-3 piezocomposites, the estimations from various micromechanical models on the longitudinal material parameters (e.g., $\bar{d}_{333}$, $\bar{\kappa}_{33}$ and etc.) are, in general, closer than the transverse and shear properties (see Odegard, 2004).

Table 4.5 Time-dependent compliance, instantaneous (elastic) compliance, Poisson's ratio and dielectric coefficient for the viscoelastic 934 epoxy at 22°C (The coefficients of Prony series are determined from Yancey and Pindera, 1990)

n	λ_n (min^{-1})	D_n (GPa^{-1})
1	1	0.0150
2	10^{-1}	0.0050
3	10^{-2}	0.0120
D_0 = 0.2217 (GPa^{-1})		
ν = 0.311		
Dielectric coefficient[a], $\kappa_{11} = \kappa_{22} = \kappa_{33}$ = 0.06 (nF/m)		

[a] This dielectric coefficient which is common for polymer materials is assumed.

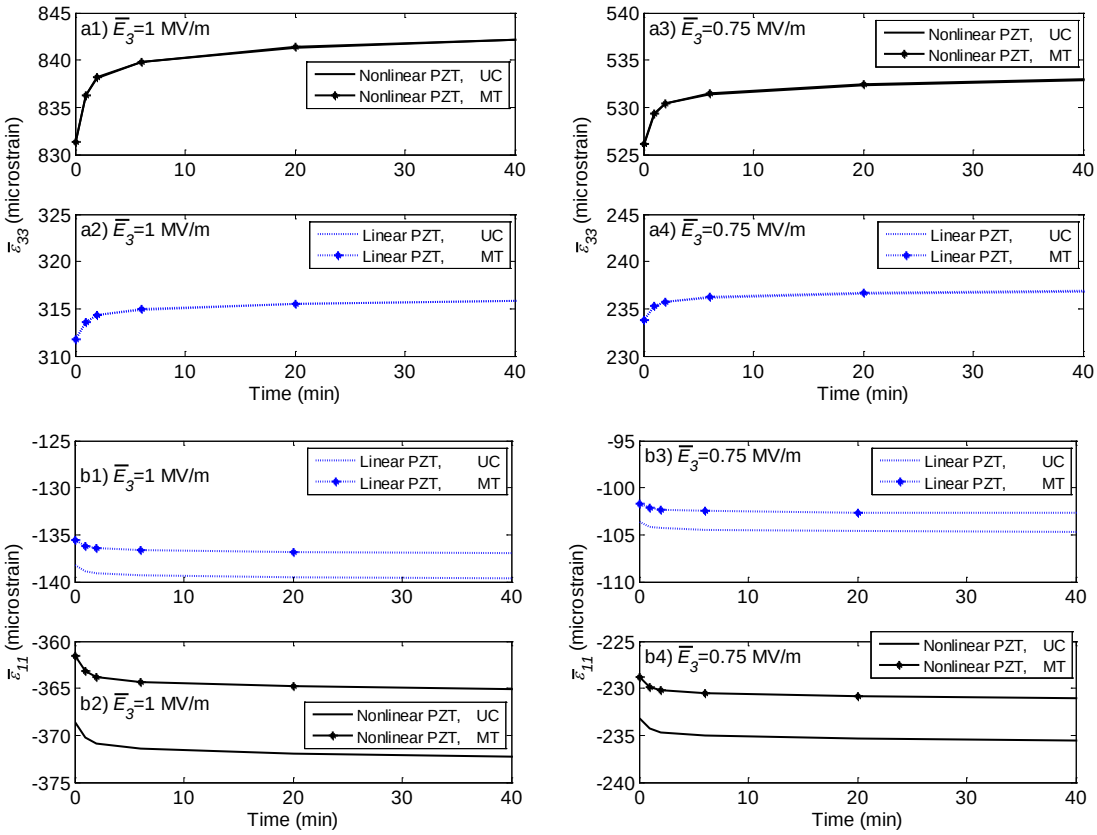

Figure 4.8 Effective longitudinal strain $\overline{\varepsilon}_{33}$ and transverse strain $\overline{\varepsilon}_{11}$ responses for the stress free PZT-G1195/934 epoxy 1-3 piezocomposite with VF = 0.5 due to applied electric fields $\overline{E}_3$ = 1 MV/m and $\overline{E}_3$ = 0.75 MV/m.

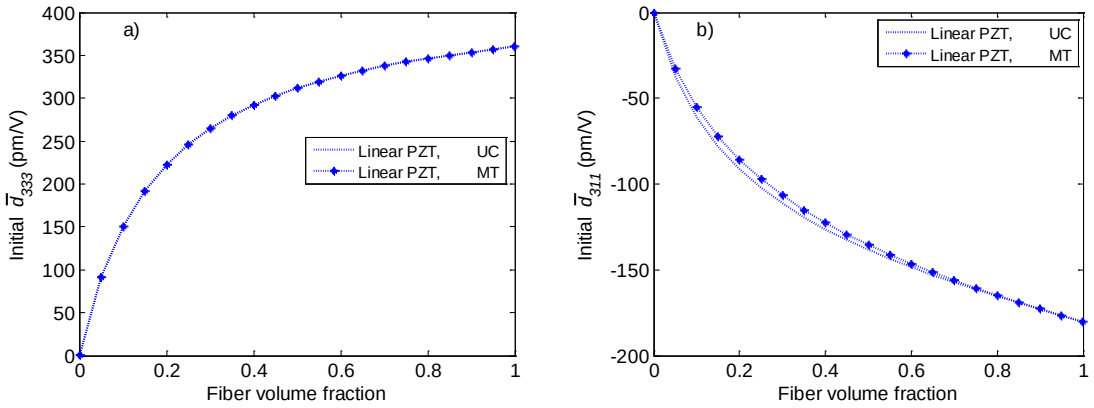

Figure 4.9 Effective initial piezoelectric strain coefficients a) $\bar{d}_{333}$ and b) $\bar{d}_{311}$ for the PZT-G1195/934 epoxy polarized 1-3 piezocomposite as a function of polarized PZT- G1195 fiber VF

The responses for a PZT-G1195/934 epoxy 0-3 piezocomposite with polarized PZT-G1195 particle VF = 0.5 subject to constant electric fields $\bar{E}_3$ =1 and 0.75 MV/m are shown in Figure 4.10. It is seen that the time-dependent strains predicted from the UC and MT models are very close both for the linear and nonlinear cases. The absolute value of the time-dependent strains $\bar{\varepsilon}_{33}$ and $\bar{\varepsilon}_{11}$, of the polarized 0-3 piezocomposite (Figure 4.10) are much smaller than those of the polarized 1-3 piezocomposite (Figure 4.8) under the same applied electric fields. This is due to the fact that in the polarized 0-3 piezocomposite, the polymeric matrix, which has low dielectric constants, dominates the overall responses and as a result only a small fraction of the applied electric field reaches the polarized piezoelectric particles. Figure 4.11 illustrates the amount of electric field reaches the polarized PZT-G1195 fibers and particles when subject to electric field $\bar{E}_3$

=1 MV/m. It is seen that the electric field in the particles are less than 0.03 MV/m (Figure 4.11b) while the one in the fiber is 1 MV/m (Figure 4.11a). It is also noted that the electric field is applied along the fiber axis ($\overline{E}_3$) and the microstructural arrangement in the polarized 1-3 piezocomposite allows for conducting this electric field directly through the polarized piezoelectric fibers, while in the case of polarized 0-3 piezocomposite, the non-conductive matrix limits the electric field in reaching the polarized piezoelectric particles. The differences in the strains $\overline{\varepsilon}_{33}$ and $\overline{\varepsilon}_{11}$, between the linear and nonlinear cases are < 5 % for the polarized 0-3 piezocomposite (Figure 4.10), which is expected; while for the polarized 1-3 piezocomposite the differences in the nonlinear and linear responses are > 100 % (Figure 4.8). Moreover, the differences in the strains $\overline{\varepsilon}_{33}$ and $\overline{\varepsilon}_{11}$ between the UC and MT predictions for the polarized 0-3 piezocomposite (Figure 4.10) are both visible. This might be due to the different assumption on the reinforcement geometry in UC (with cubic particle) and MT (with spherical particle) models.

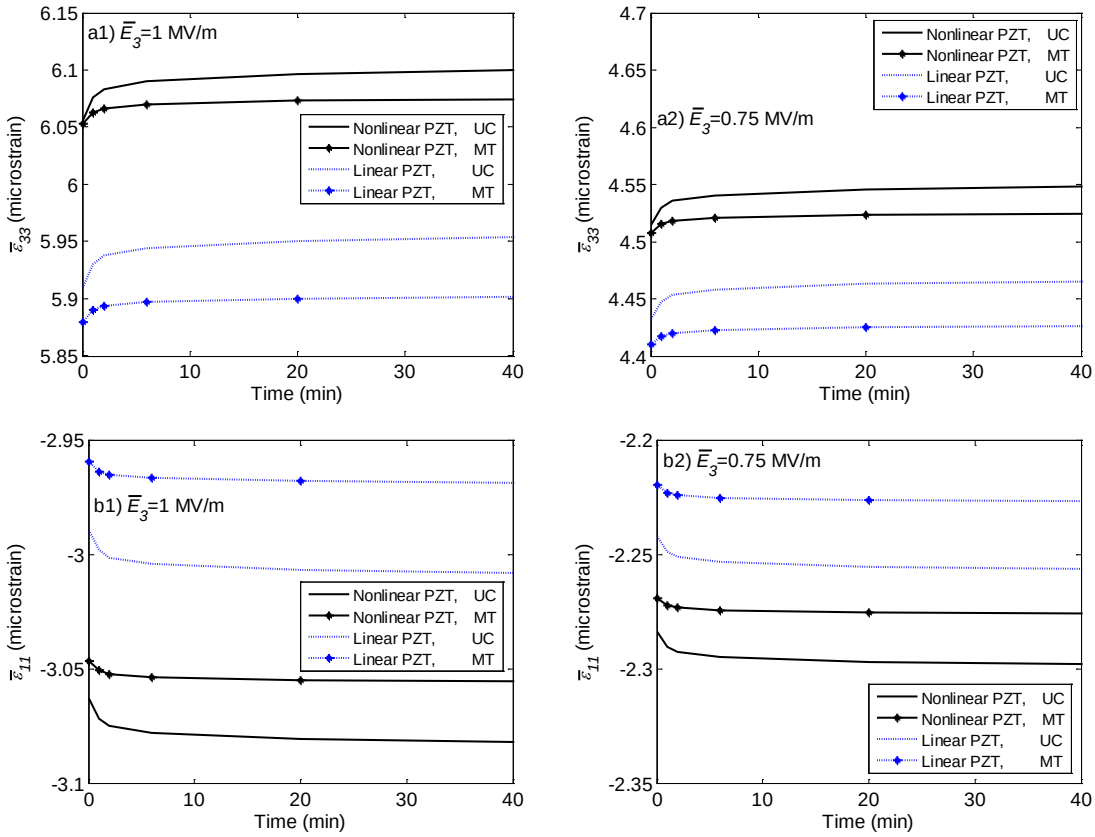

Figure 4.10 Effective strain $\bar{\varepsilon}_{33}$ and $\bar{\varepsilon}_{11}$ responses for the stress free PZT-G1195/934 epoxy polarized 0-3 piezocomposite with VF = 0.5 due to applied electric fields $\bar{E}_3$ = 1 MV/m and $\bar{E}_3$ = 0.75 MV/m.

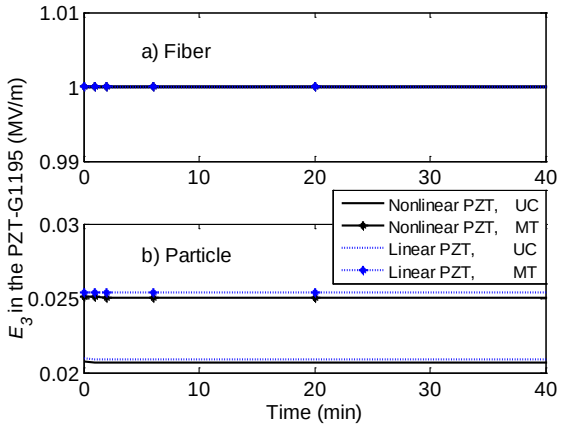

Figure 4.11 Average electric field E_3 in the PZT-G1195 inhomogeneity for the stress free PZT-G1195/934 epoxy polarized a) 1-3 and b) 0-3 piezocomposites with polarized PZT-G1195 inhomogeneity VF = 0.5 due to an applied electric field $\overline{E}_3$ = 1 MV/m along the poling direction.

We now consider fully constrained displacement conditions for polarized 1-3 and 0-3 piezocomposites, with inhomogeneity VF = 0.5. Figure 4.12 depicts the effective stresses for PZT-G1195/FM73 piezocomposites due to a constant electric field $\overline{E}_3$ =1 MV/m. The property of the viscoelastic FM73 polymer is listed in Table 4.6. The UC and MT predictions are close to each other for both linear and nonlinear cases for the polarized 1-3 piezocomposite, shown in Figure 4.12a. The differences on the transverse relaxation stresses $\bar{\sigma}_{11}$between the UC and MT predictions for either linear or nonlinear case are due to the different reinforcement geometry on fiber cross section (circle vs. square) which has more significant influence on the transverse responses than the longitudinal responses for the polarized 1-3 piezocomposite. For the polarized 0-3 piezocomposite, which is matrix-dominated responses, small differences between the

linear and nonlinear predictions are observed, as shown in Figure 4.12b, but some differences between the UC and MT predictions are shown as explained above.

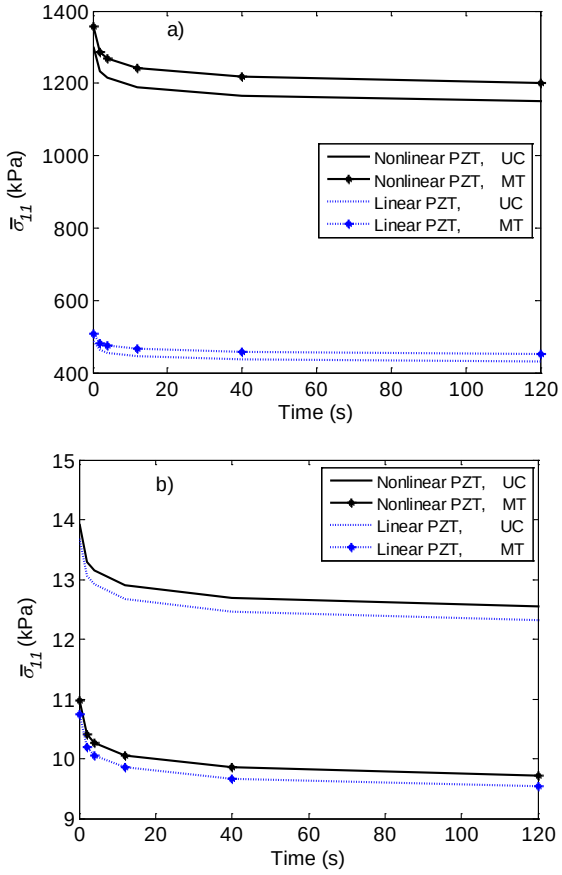

Figure 4.12 Effective stress $\bar{\sigma}_{11}$ responses for the fully constrained PZT-G1195/FM73 polymer polarized a) 1-3 and b) 0-3 piezocomposite with polarized PZT-G1195 inhomogeneity VF = 0.5 under $\overline{E}_3$ = 1 MV/m.

Table 4.6 Time-dependent compliance, instantaneous (elastic) compliance, Poisson's ratio and dielectric coefficient for the viscoelastic FM73 polymer at 30~60°C (Muliana and Khan, 2008)

n	λ_n (sec^{-1})	D_n (GPa^{-1})
1	1	0.0210
2	10^{-1}	0.0216
3	10^{-2}	0.0118
4	10^{-3}	0.0159
5	10^{-4}	0.0216
6	10^{-5}	0.0200
D_0 = 0.369 (GPa^{-1})		
ν = 0.35		
Dielectric coefficient[a], $\kappa_{11} = \kappa_{22} = \kappa_{33}$ = 0.04 (nF/m)		

[a] This dielectric coefficient which is common for polymer materials is assumed.

Now, the effect of frequency on the hysteretic electromechanical response is examined. The UC predictions of the cyclic electric loadings, $\bar{E}_3(t) = -0.5\cos(2\pi ft)+0.5$ MV/m with the frequencies f = 0.5, 1 and 10 Hz along the poling direction, on a fully constrained PZT-G1195/FM73 polymer polarized 1-3 piezocomposite with polarized PZT-G1195 fiber VF = 0.5 are shown in Figure 4.13. Only nonlinear constitutive

relations, i.e., Equations (2.3) and (2.4), are considered for the polarized piezoelectric PZT-G1195 fibers in the following discussion. For the frequency f = 0.5, the transverse stress, $\bar{\sigma}_{11}$, (Figure 4.13b) shows more significant hysteresis than the longitudinal stress, $\bar{\sigma}_{33}$, (Figure 4.13a) does because the transverse response is dominated by the viscoelastic matrix. The same trends are also observed for the other frequencies f = 1 and 10 Hz (Figure 4.13c, d and Figure 4.13e, f), respectively. Due to the viscoelastic matrix, the lower frequency (slower loading) shows the broader hysteretic loop (Figure 4.13b, d and f) since slower loading rates give enough time for the matrix to undergo more pronounced creep deformation (or stress relaxation), resulting in higher energy dissipation in one cycle. In this case, the maximum tensile transverse stress $\bar{\sigma}_{11}$ (i.e., $\bar{\sigma}_{11}$ amplitude) occurs when the periodic loading $\bar{E}_3 = -0.5\cos(2\pi ft)+0.5$ MV/m reaches 1 MV/m in the first cycle. The maximum stress decreases with increasing number of cycles and reaches to a steady value.

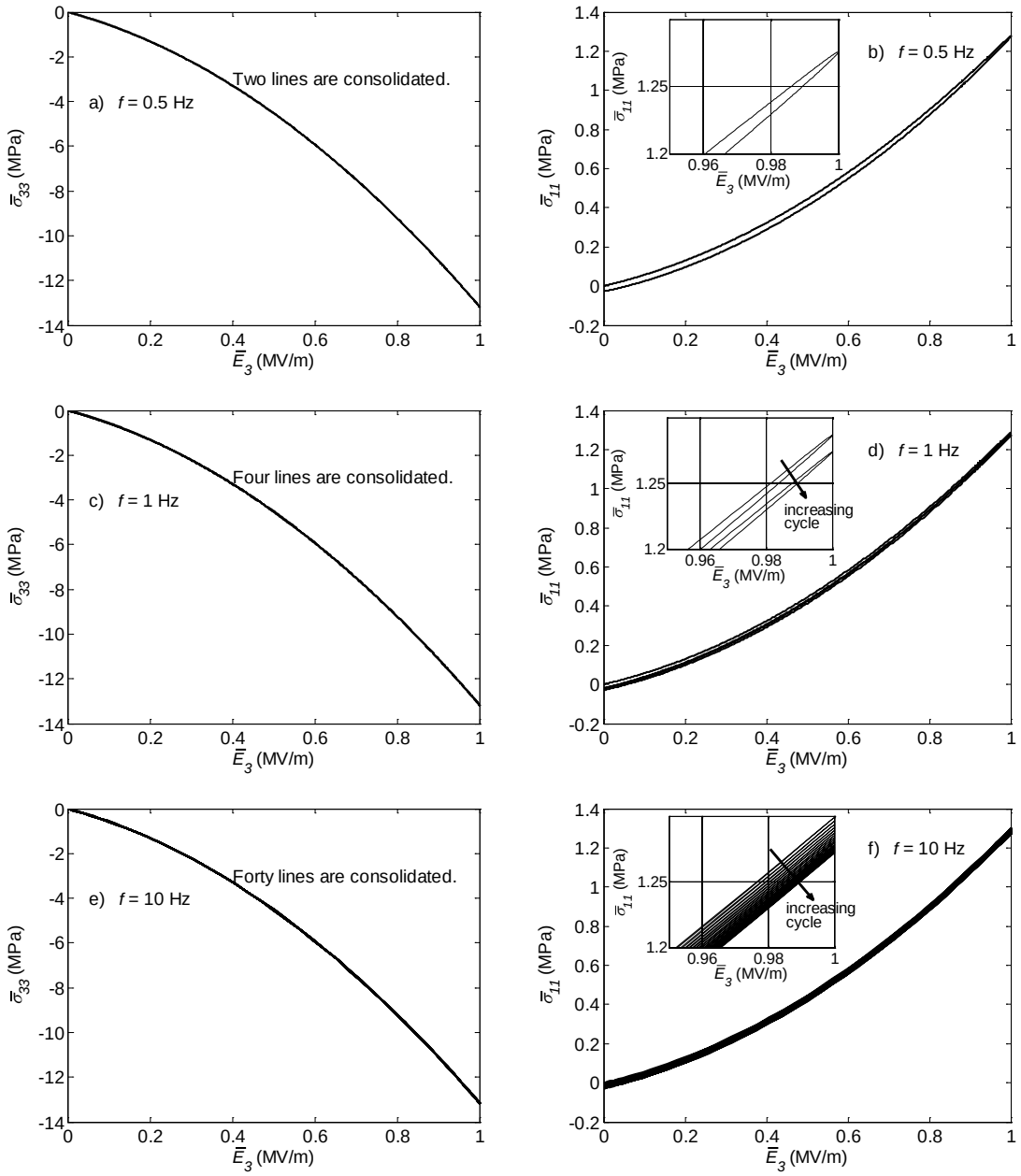

Figure 4.13 UC responses of the effective stresses for the fully constrained PZT-G1195/FM73 polymer polarized 1-3 piezocomposite with VF = 0.5 subjected to a cyclic electric loading $\bar{E}_3(t) = -0.5\cos(2\pi ft)+0.5$ MV/m with various. Total time to complete the analyses is two seconds.

Figure 4.14 depicts the $\bar{\sigma}_{11}$ amplitude in the first cycle versus frequency. Lower frequency results in lower $\bar{\sigma}_{11}$ amplitude. Thus, a relatively slow electric loading (i.e., lower frequency) gives sufficient time for the stress to experience relaxation behaviors. The stress amplitude (or maximum stress) as a function of number of cycles at different loading frequencies is shown in Figure 4.15. As the number of cycles increase (longer duration of loading), the stress amplitude decreases until it reaches a steady value. The higher fthe requency is the more cycle is needed to reach the steady state (i.e., fully relaxed stress state), which is expected.

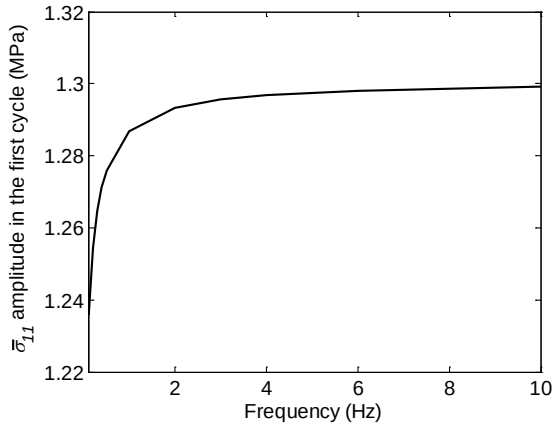

Figure 4.14 UC response on the effective stress σ_{11} amplitude in the first cycle vs. frequency for the fully constrained PZT-G1195/FM73 polymer 1-3 piezocomposite with VF = 0.5 subjected to a cyclic electric loading with various frequencies.

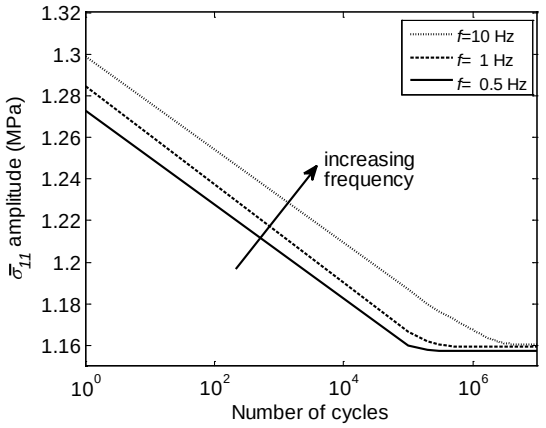

Figure 4.15 UC responses of the effective stress σ_{11} amplitude vs. number of cycles for a fully constrained PZT-G1195/FM73 polymer 1-3 piezocomposite with VF = 0.5 subjected to a cyclic electric loading. (Logarithmic scale on the horizontal axis)

We also study the influence of the piezoelectric volume fraction on the overall creep deformations of the polarized 1-3 and 0-3 piezocomposites undergoing high electric field inputs. Only nonlinear constitutive relations, i.e., Equations (2.1) and (2.2), are considered for the polarized piezoelectric inhomogeneities in the following discussion. Figure 4.16 depicts the effective time-dependent strains for the polarized 1-3 piezocomposites with different polarized PZT-G1195 fiber volume fractions (i.e., VF = 0.3~0.7) subject to a constant electric field $\bar{E}_3$ =1 MV/m. The responses from the UC and MT models are presented. More significant time-dependent strains are observed for composites with smaller polarized piezoelectric fiber volume fractions, which are expected because there is larger fraction of viscoelastic matrix as opposed to polarized piezoelectric fibers.

The time-dependent strains of the polarized 0-3 piezocomposites are illustrated in Figure 4.17, which show less significant time-dependent deformations. This is because only a small portion of applied electric fields reaches the polarized piezoelectric particles and consequently the polymeric matrix undergoes small mechanical stimuli. The effects of different reinforcement geometry are more visible at the VF = 0.1 than those at the VF=0.5 for the polarized 0-3 piezocomposites (Figure 4.17) or similarly those at the VF = 0.3 than those at the VF=0.7 for the polarized 1-3 piezocomposites (Figure 4.16b). The mismatches between the UC and MT predictions gradually change as VF changes which also depend on the response being studied.

For the polarized 1-3 piezocomposites, Figure 4.18a shows the effective initial transverse strain and it is seen that the UC and MT predictions on the effective transverse strain (Figure 4.16b) get closer from VF=0.3 to 0.7. For the polarized 0-3 piezocomposites, the effective initial transverse strain in Figure 4.18b shows that the UC and MT estimations are closer from VF=0.1 to 0.5.

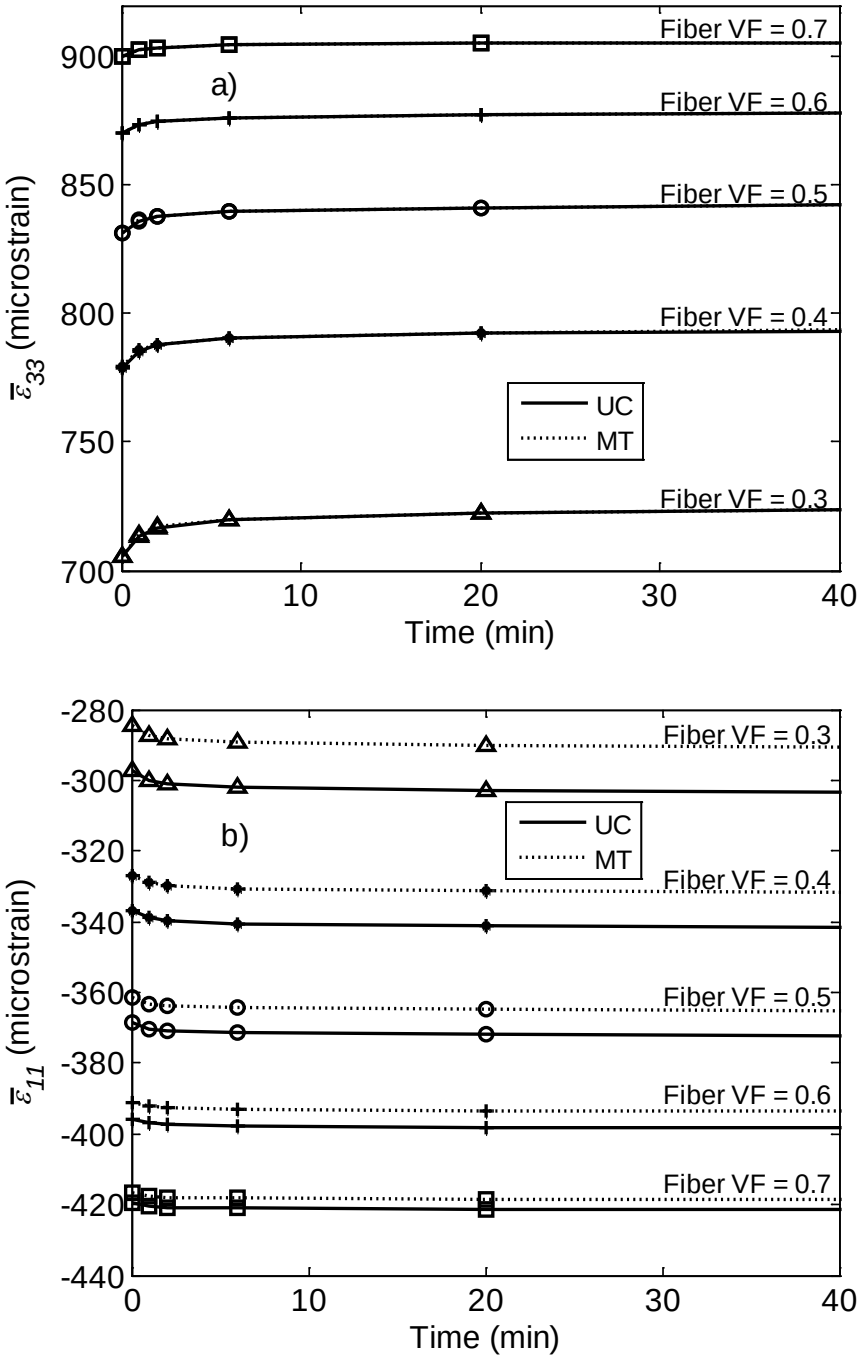

Figure 4.16 Effective strain a) $\bar{\varepsilon}_{33}$ and b) $\bar{\varepsilon}_{11}$ responses for the stress free PZT-G1195/934 epoxy 0-3 piezocomposite with various particle VF = 0.1, 0.2, 0.3, 0.4, and 0.5 due to an applied electric field $\bar{E}_3$ = 1 MV/m along the poling direction.

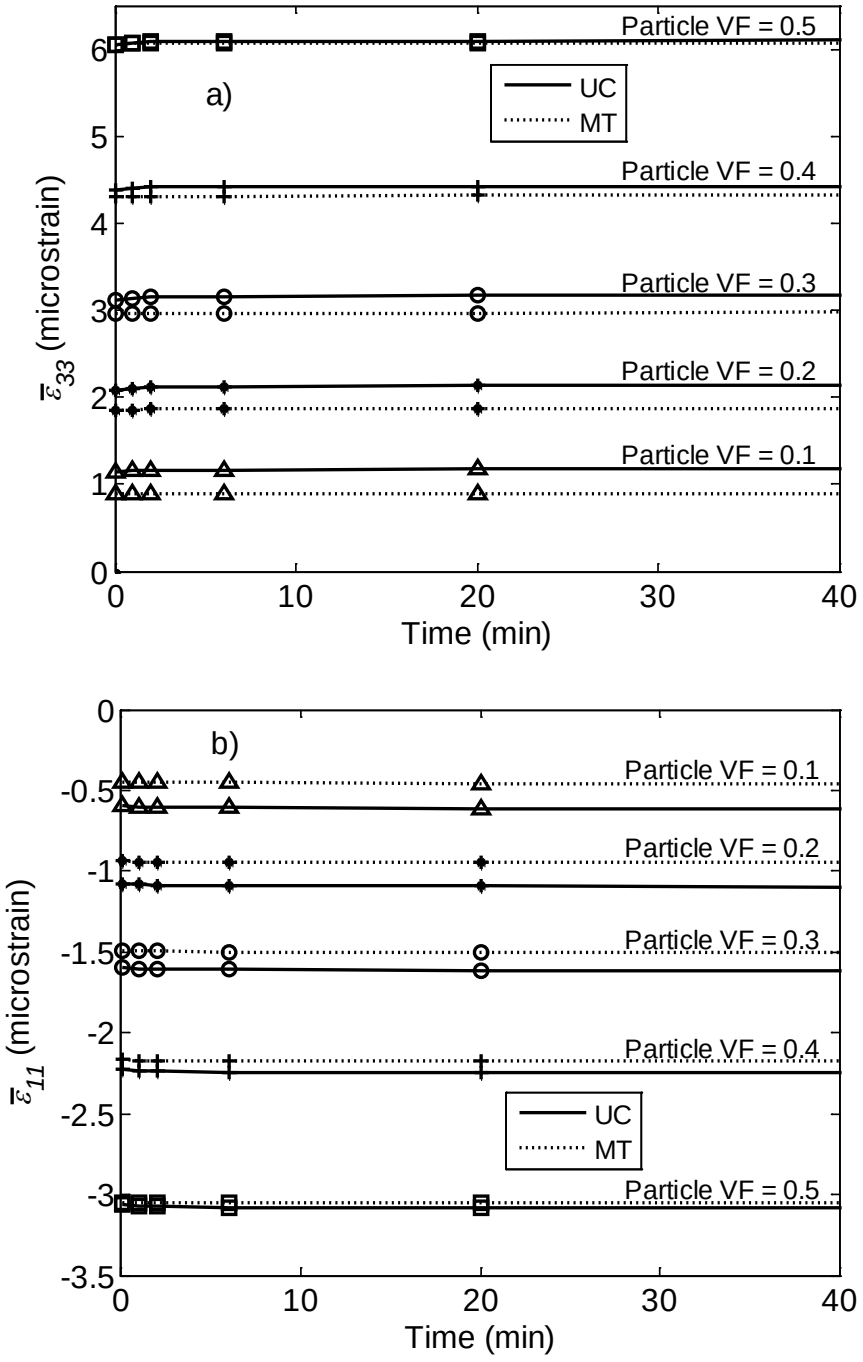

Figure 4.17 Effective a) longitudinal strain $\bar{\varepsilon}_{33}$ and b) transverse strain $\bar{\varepsilon}_{11}$ responses for the stress free PZT-G1195/934 epoxy 1-3 piezocomposite with various VF = 0.3, 0.4, 0.5, 0.6, and 0.7 due to an applied electric field $\bar{E}_3$ = 1 MV/m along the poling direction.

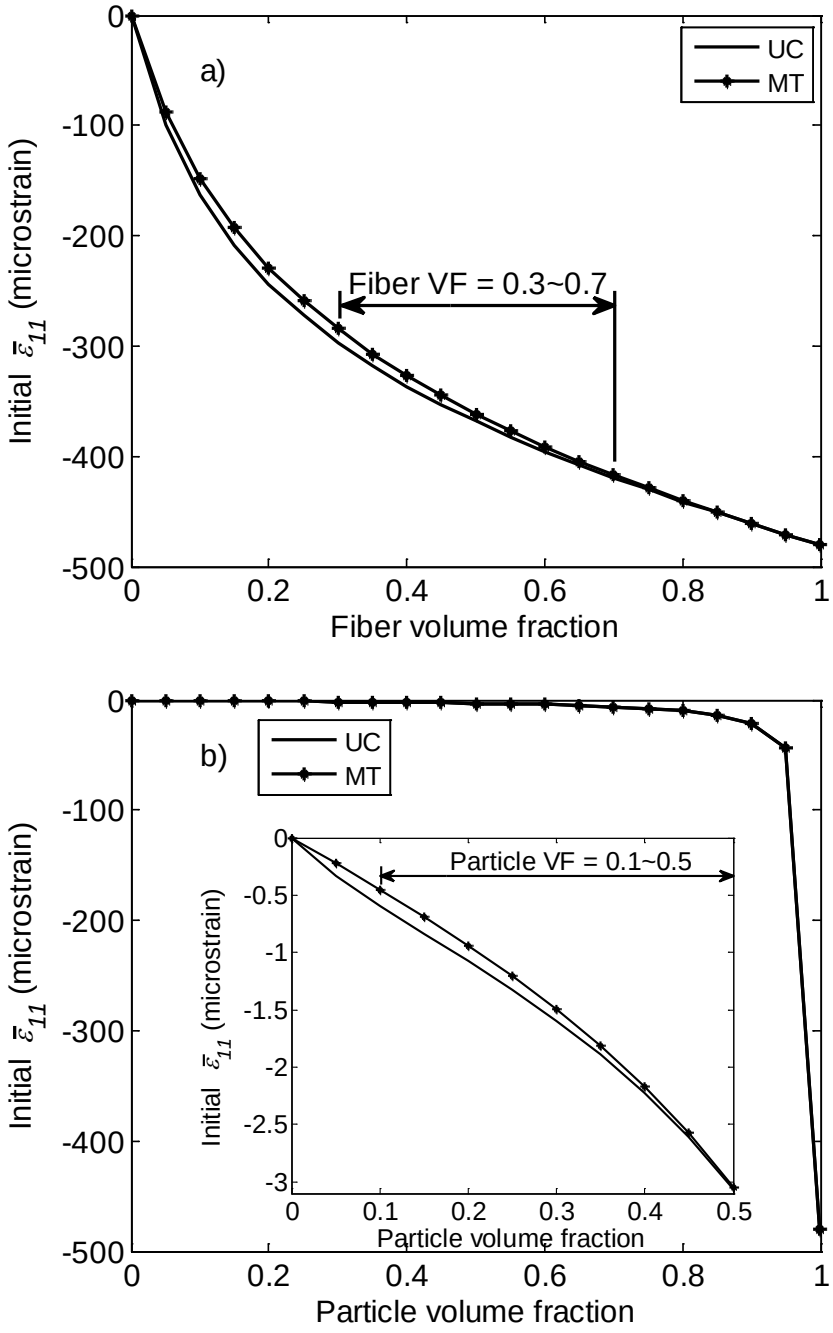

Figure 4.18 Effective initial strain $\overline{\varepsilon}_{11}$ responses for the stress free PZT-G1195/934 epoxy a) 1-3 and b) 0-3 piezocomposite due to an applied electric field $\overline{E}_3$ = 1 MV/m along the poling direction as a function of PZT- G1195 inhomogeneity VF.

It is seen that the polymeric matrix dominates the overall responses of the polarized 0-3 piezocomposite and we further examine the responses of a polarized 0-3 piezocomposite by reversing the particle and matrix constituents. The reversed-phase piezocomposite is formed by 934 epoxy particles embedded in a polarized PZT-G1195 matrix. Figure 4.19 compares the predictions from the UC model on the effective initial (instantaneous) strain, $\bar{\varepsilon}_{33}$, between the reversed-phase and original 0-3 piezocomposites. The results for the reversed-phase 0-3 piezocomposite are only obtained from the UC model. The response for the reversed-phase 0-3 piezocomposite significantly depends on the volume fraction of the polarized PZT matrix while the response for the original 0-3 piezocomposite is almost invariant until 85% of the volume fraction of the polarized PZT particle reinforcements. A large portion of the applied electric field reaches the matrix in the polarized 0-3 piezocomposite. Thus, for the reversed-phase 0-3 piezocomposite a relatively large magnitude of strain, $\bar{\varepsilon}_{33}$, is observed when the electric field is applied to the composites even for a small amount of the polarized PZT.

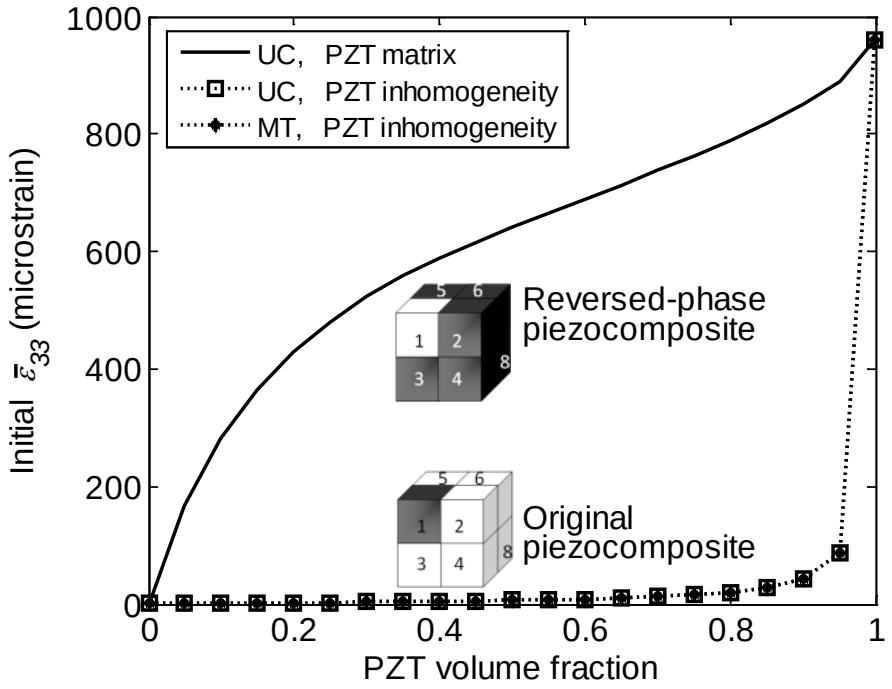

Figure 4.19 Effective initial strain $\bar{\varepsilon}_{33}$ vs. polarized PZT-G1195 VF for the stress free polarized 0-3 piezocomposites undergoing an electric field $\bar{E}_3$ =1 MV/m along the poling direction. The upper line indicates the prediction on the initial response for the reversed-phase piezocomposite having 934 epoxy particles in a polarized PZT-G1195 matrix while the lower lines denote the estimations on the initial responses for the original piezocomposite having polarized PZT-G1195 particles in a 934 epoxy matrix. For each representative unit cell, the black subcell represents the polarized PZT-G1195 constituent and the white the 934 epoxy.

CHAPTER V

POLARIZATION SWITCHING RESPONSES OF 1-3 AND 0-3 PIEZOCOMPOSITES

This chapter uses the fiber- and particle-UC models presented in Chapter III to investigate the effective polarization switching responses of 1-3 and 0-3 piezocomposites. Experimental validations are first provided and parametric studies are then performed to illustrate the effects of microstructural geometry and volume content of the piezoceramic inhomogeneities as well as loading history on the overall hysteretic responses of the 1-3 and 0-3 piezocomposites. The constitutive relations in Equations (2.22) and (2.23) are used for simulating the polarization switching response of piezoceramics while those in Equations (2.47) and (2.48) are applied to inactive viscoelastic constituent.

5.1 Comparison with Experimental Data

Jayendiran and Arockiarajan (2013) conducted experiments on studying the effective hysteretic polarization and butterfly strain responses of PZT-5A1/epoxy II 1-3 piezocomposite with various PZT-5A1 fiber volume fractions under cyclic electric field with amplitude of $\bar{E}_3 = \pm 2$ MV/m, along the poling direction (x_3 direction). Since Jayendiran and Arockiarajan (2013) did not include the information regarding the number of cycles after which the data are collected, initial cycle or saturated state, and loading rate of the electric field for simplicity we shall assume that PZT-5A1

experiences *time-independent* polarization switching, in which $\kappa_1 = 0$ in Equation (2.40). The material properties of the PZT-5A1 are first calibrated from the experimental data of PZT-5A1 (100% fiber content) under a cyclic electric field, shown in Figure 5.1.

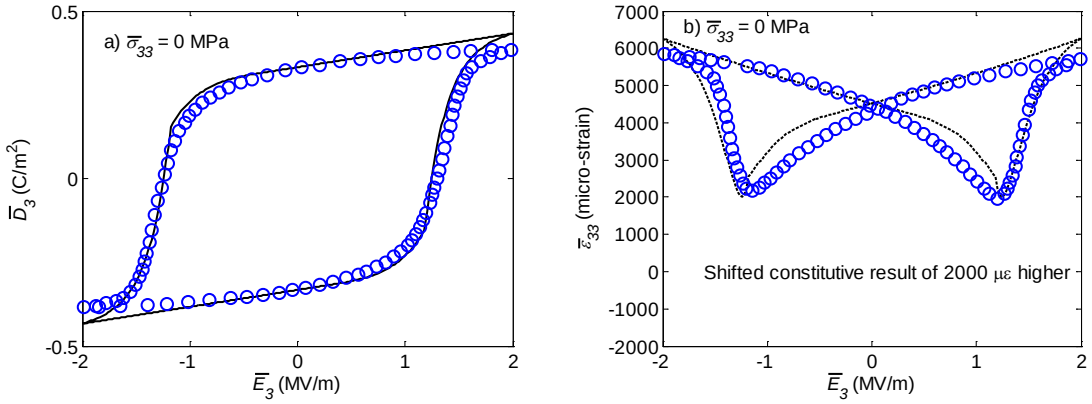

Figure 5.1 a) Hysteretic polarization and b) butterfly strain responses for the stress free PZT-5A1 due to a cyclic electric field.

The remanent polarization P_r =0.33 C/m^2 is determined at zero electric field upon removal of the electric field input, shown in Figure 5.1a. The coercive electric field in absence of mechanical stresses E_c^0 =1.19 MV/m is estimated when the polarization is zero (Figure Figure 5.1a), which also corresponds to the lowest strains as shown in Figure 2b. The material parameters κ_0, λ, n, μ, and ω are obtained by fitting the $\bar{D}_3$ vs. $\bar{E}_3$ curve in Figure 5.1a and they are listed in Table 5.1.

Table 5.1 Material parameters for the time-dependent polarization of PZT-5A1

	E_c^0	κ_0	κ_1	τ_1	λ	n	μ	ω
	(MV/m)	($\times 10^{-9}$ F/m)		(sec)	($\times 10^{-6}$ F/m)		($\times 10^{-6}$ F/m)	
PZT-5A1	1.19	50	0	−	0.50	4	2.8	6

The parameter κ_0 is determined from the unloading path (removal of the electric field to zero value), the parameters λ and n are calibrated from the loading path when the electric field is less than the coercive limit, and the parameters μ and ω are calibrated from the loading path when the electric field is larger than the coercive limit. In order to capture the butterfly strain response we need the piezoelectric coefficient g_{ijk}^t that the depends on the polarization state P_3^t, and the following function is assumed:

$$g_{ijk}^t = \alpha \frac{P_3^t}{P_r} g_{ijk}^r, \tag{5.1}$$

Here $\mathbf{g}^r = \boldsymbol{\kappa}^{-1}\mathbf{d}^r.$, where $\mathbf{d}^r$ is the direct piezoelectric constant measured at remanent polarization. The parameters d_{333}^r, d_{311}^r, and κ_{33}^r are taken from the values reported by Jayendiran and Arockiarajan (2013) and κ_{11}^r=16.7×10^{-9} F/m is assumed[10]. The material parameter α needs to be calibrated from experiment. We further calibrate α to 0.14 by

[10] This value is assumed since it is not reported in Jayendiran and Arockiarajan (2013). The κ_{33}^r =16.4×10^{-9} F/m of the PZT-5A1 reported by Jayendiran and Arockiarajan (2013) is close to the κ_{33}^r =15.3×10^{-9} F/m of PZT-5A obtained from the manufacture data sheet of Morgan Electro Ceramics. The ratio of κ_{33}^r to κ_{11}^r of the PZT-5A1 is assumed to be same as the one of the PZT-5A.

fitting $\bar{\varepsilon}_3$ vs. $\bar{E}_3$ curve shown in Figure 5.1b. The electro-mechanical coupling parameters are listed in Table 5.2.

Table 5.2 Electro-mechanical coupling parameters for PZT-5A1

	d^r_{333}	d^r_{311}	κ^r_{11}	κ^r_{33}	P_r	α
	($\times 10^{-12}$ m/V)		($\times 10^{-9}$ F/m)		(C/m^2)	
PZT-5A1	440	−185	16.7	16.4	0.330	0.14

It is seen in Figure 5.1b that the experimental strain for pure PZT-5A1in absence of mechanical stress is about 2000 $\mu\varepsilon$ at the coercive electric field, while one would expect that in absence of external mechanical stresses and for stress-free boundary conditions, at the coercive electric field strains would generally be nearly zero since depolarization has occurred in the ferroelectric ceramics at the coercive electric field. The material parameters are calibrated after shifting 2000 $\mu\varepsilon$ higher. The elastic material parameters, i.e.,Young's moduli E_{11} = 59.62, E_{33} = 48.97, shear moduli G_{12} =21.85, G_{31} =21 GPa, and Poisson's ratios v_{12} =0.364 and v_{31} =0.474 listed in Table 5.3 are determined by assuming a transversely isotropic PZT-5A1 from the linear elastic constants c_{3333} =116.8 and c_{1133} =87.1 GPa reported by Jayendiran and Arockiarajan (2013).

Table 5.3 Mechanical engineering constants for PZT-5A1

	$E_{11}=E_{22}$ (GPa)	E_{33} (GPa)	G_{12} (GPa)	$G_{31}=G_{32}$ (GPa)	v_{12}	$v_{31}=v_{32}$
PZT-5A1	59.62	48.97	21.85	21.00	0.364	0.474

Figure 5.1 shows that the polarization switching model and the calibrated material parameters of the PZT-5A1 discussed above are able to capture the hysteretic polarization and butterfly strain responses.

Jayendiran and Arockiarajan (2013) also reported the experimental results for the pure PZT-5A1 subject to both a cyclic electric field and a constant mechanical stress (i.e., $\bar{\sigma}_{33}$= −15 MPa) shown in Figure 5.2 (circles). The existence of the compressive stresses influences the polarization response of materials. The coercive electric field under a constant compressive stress 15 MPa, E_c =0.76 MV/m, is determined when the polarization is zero as shown in Figure 5.2a. From the experimental evidences the coercive electric fields vary with the compressive stresses. We assume the coercive electric fields *linearly* vary with the compressive stresses, which can be described by the following function:

$$E_c = \begin{cases} E_c^0 - 0.029\left|\sigma_{33}^t\right|, & \sigma_{33}^t < 0, \\ E_c^0, & \sigma_{33}^t \geq 0. \end{cases} \tag{5.2}$$

We further assume the coercive stress limit is 12 MPa. The material parameters above the coercive stress limit λ, n, μ, and ω are obtained by fitting $\bar{D}_3$ vs. $\bar{E}_3$ curve shown

in Figure 5.2a and they are listed in Table 4. The parameter α =0.1 is calibrated from the butterfly curve in Figure3b after shifting the strain response 2500 με higher and listed in Table 5.4. All the calibrated material parameters from Table 5.1 to Table 5.4 are used for the PZT-5A1 fibers in the micromechanics model.

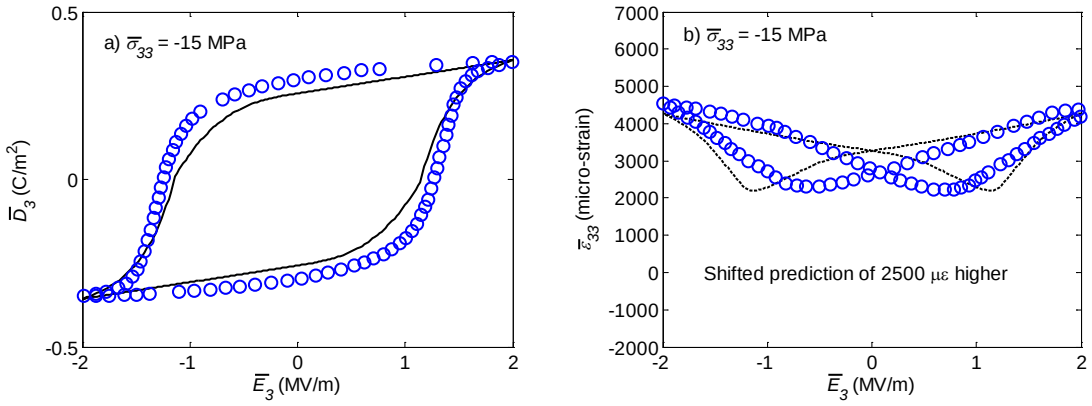

Figure 5.2 a) Hysteretic polarization and b) butterfly strain responses for the PZT-5A1 due to a cyclic electric field and a constant compressive stress.

Table 5.4 Material parameters above the coercive stress limit for PZT-5A1

	σ_c (MPa)	α	λ ($\times 10^{-6}$ F/m)	n	μ ($\times 10^{-6}$ F/m)	ω
PZT-5A1	12	0.1	0.5	2	1.2	4

In order to predict response of the composites, the epoxy II matrix is assumed as an elastic isotropic solid with elastic modulus 2.9 GPa, Poisson's ratio 0.3 and dielectric

constant 0.040×10^{-9} F/m as reported by Jayendiran and Arockiarajan (2013) listed in Table 5.5.

Table 5.5 Mechanical and electrical properties of the epoxy II (Jayendiran and Arockiarajan, 2013)

	Epoxy II
Young's modulus, E (GPa)	2.9
Poisson's ratio, ν	0.3
Dielectric coefficient, $\kappa_{11} = \kappa_{22} = \kappa_{33}$ (nF/m)	0.04

The micromechanical predictions for a stress free PZT-5A1/epoxy II 1-3 active composite with PZT-5A1 fiber VF = 0.8 are shown in Figure 5.3. The predictions of the effective hysteretic polarization are in good agreements with experimental data (Figure 5.3a) while the prediction of the effective butterfly strain response show significant mismatch with the experimental result (Figure 5.3b). We are not sure about the reason that the experimental measurements of the effective butterfly strain responses at the coercive electric field drifted upward above zero for the pure PZT-5A1 (Figure 5.1b) but shifted downward below zero for the 1-3 active composites (Figure 5.3b), which shows that the height of the butterfly strain response of the experimental measurements of the active composite (Figure 5.3b) is larger than the one of the pure PZT-5A1 (Figure 5.1b). One would also expect that the height of the hysteretic polarization (saturated

polarization) decreases as the volume content of the active fiber decreases (Figure 5.1b to Figure 5.3b) and similarly for the strain in the butterfly strain curves. However, the strains do not show certain trend with regards to the height of the butterfly strains (Figure 5.1b to Figure 5.3b). It is noted that other experimental data reported by Nelson (2003) on polarization switching of active fiber composites indicated that the saturated polarization and saturated strain values decrease with decreasing contents of PZT. According to Jayendiran and Arockiarajan (2013), the reason as to why the butterfly strain curves of the 1-3 active composites with VF = 0.8 (Figure 5.3b) have larger hysteretic response than the one of pure PZT (Figure 5.1b) is probably caused by the bias stress-induced ferroelectric switching which promotes in-plane to out-of-plane 90º polarization switching (Burcsu et al. 2004 and Shieh et al., 2007).

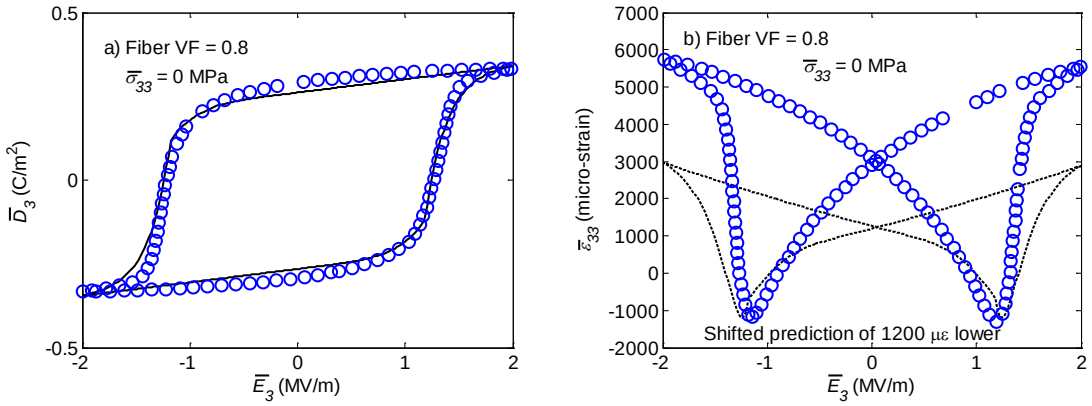

Figure 5.3 Comparison of micromechanical predictions (solid and dashed lines) to experimental data (circles) of Jayendiran and Arockiarajan (2013) for the a) hysteretic polarization and b) butterfly strain responses for the stress free PZT-5A1/epoxy II 1-3 active composite with PZT-5A1 fiber VF=0.8.

Figure 5.4 depicts the average nonzero stresses and electric field in the PZT-5A1 fiber of the active composite with PZT-5A1 fiber VF = 0.8, determined from the micromechanics model.

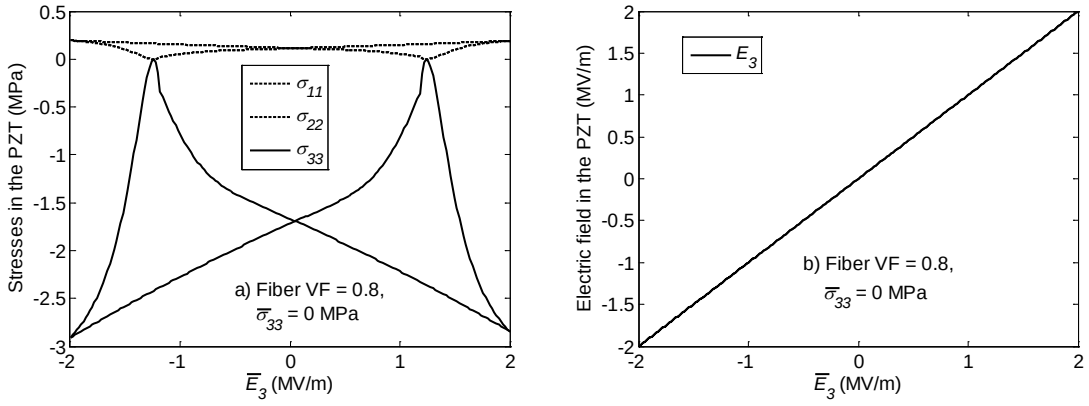

Figure 5.4 Average nonzero stresses and electric field in the PZT-5A1 fiber for the stress free boundary condition of a PZT-5A1/epoxy II 1-3 active composite with PZT-5A1 fiber VF=0.8 subject to the cyclic electric loading.

Jayendiran and Arockiarajan (2013) further examined the effects of compressive stresses on the overall nonlinear electro-mechanical hysteresis of 1-3 active composites. The effective responses are recorded by applying both constant compressive stresses, $\bar{\sigma}_{33} = -15, -30$ and -45 MPa, and a cyclic electric field with amplitude of $\bar{E}_3 = \pm 2$ MV/m along the poling direction on the PZT-5A1/epoxy II 1-3 composites with PZT-5A1 fiber VF = 0.8. Figure 5.5 depicts the comparisons between the micromechanical predictions and experimental data. The agreements on the effective hysteretic polarization between the micromechanical predictions and experimental data are good

for each compressive stress (Figure 5.5a, c, e) while the estimations of the effective butterfly strain responses show some discrepancies with the experimental results in Figure 5.5b with a similar trend as in Figure 5.3b. The compressive stresses limit the amount of polarization to be generated from the electric field inputs; as a result smaller hysteretic polarization and butterfly strain curves are observed both in the micromechanical predictions and in the experimental data when higher compressive stress is applied. In order to compare the butterfly strains, we shift the initial values of the butterfly strains to the ones of the experimental data, shown in Figure 5.5b, d, and f. It is seen that the micromechanical predictions are able to qualitatively capture the heights of the butterfly strain curves of the experiment data.

Jayendiran and Arockiarajan (2013) also investigated the effects of PZT-51 fiber VFs on the overall nonlinear electro-mechanical hysteresis of 1-3 active composites subject to both a cyclic electric field with amplitude of $\bar{E}_3 = \pm 2$ MV/m along the poling direction and a constant compressive stress, $\bar{\sigma}_{33} = -15$ MPa. The predictions of the effective hysteretic polarization are in good agreements with experimental results (Figure 5.6a, c and e) while the predictions of the effective butterfly strain responses show some mismatches with the experimental results (Figure 5.6b, d and f) as already discussed above.

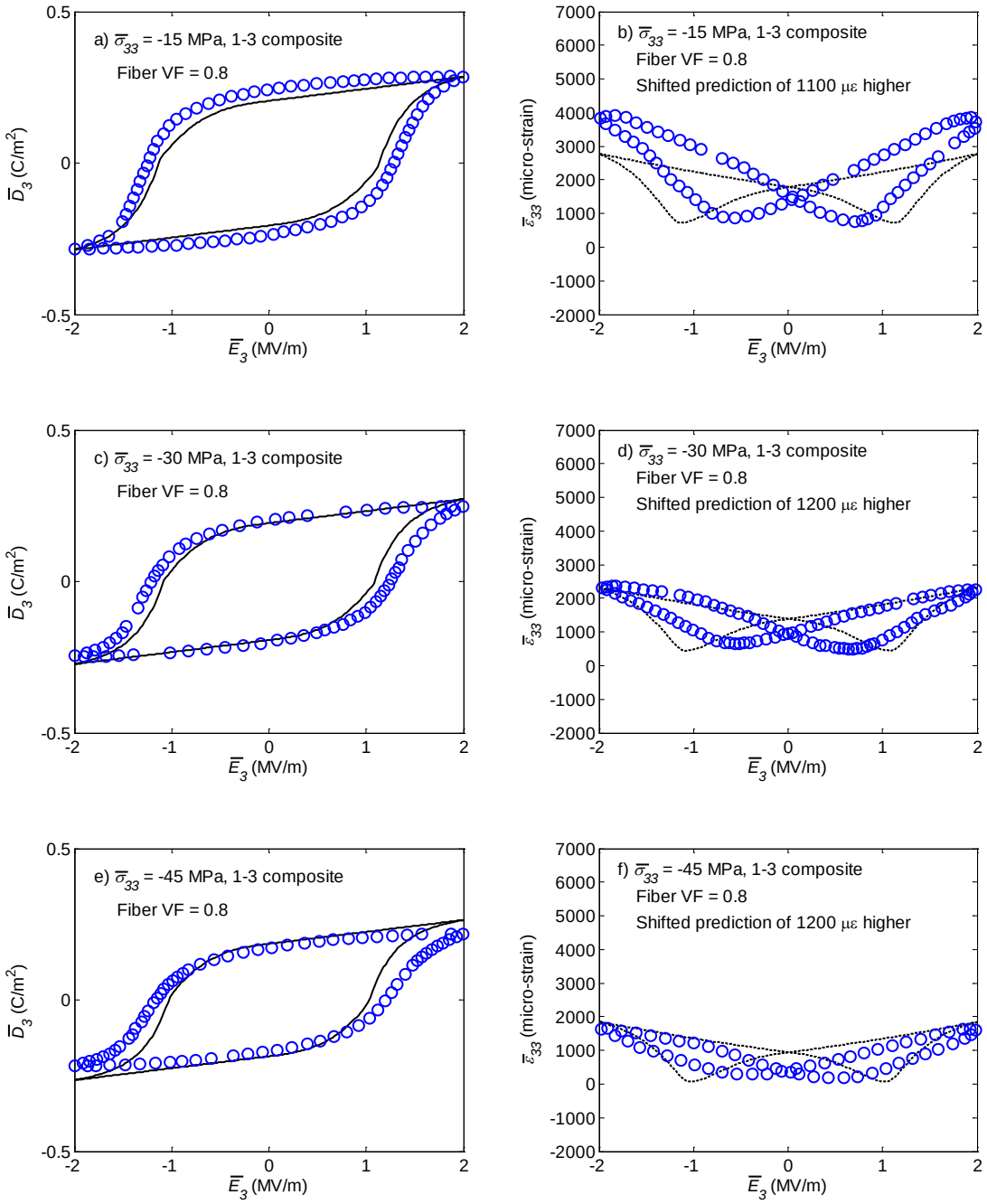

Figure 5.5 Comparison of micromechanical predictions (solid and dashed lines) to experimental data (circles) of Jayendiran and Arockiarajan (2013) for the hysteretic polarization and butterfly strain responses for the PZT-5A1/epoxy II 1-3 active composite with PZT-5A1 fiber VF = 0.8 subjected to both a cyclic electric field and various constant mechanical stresses.

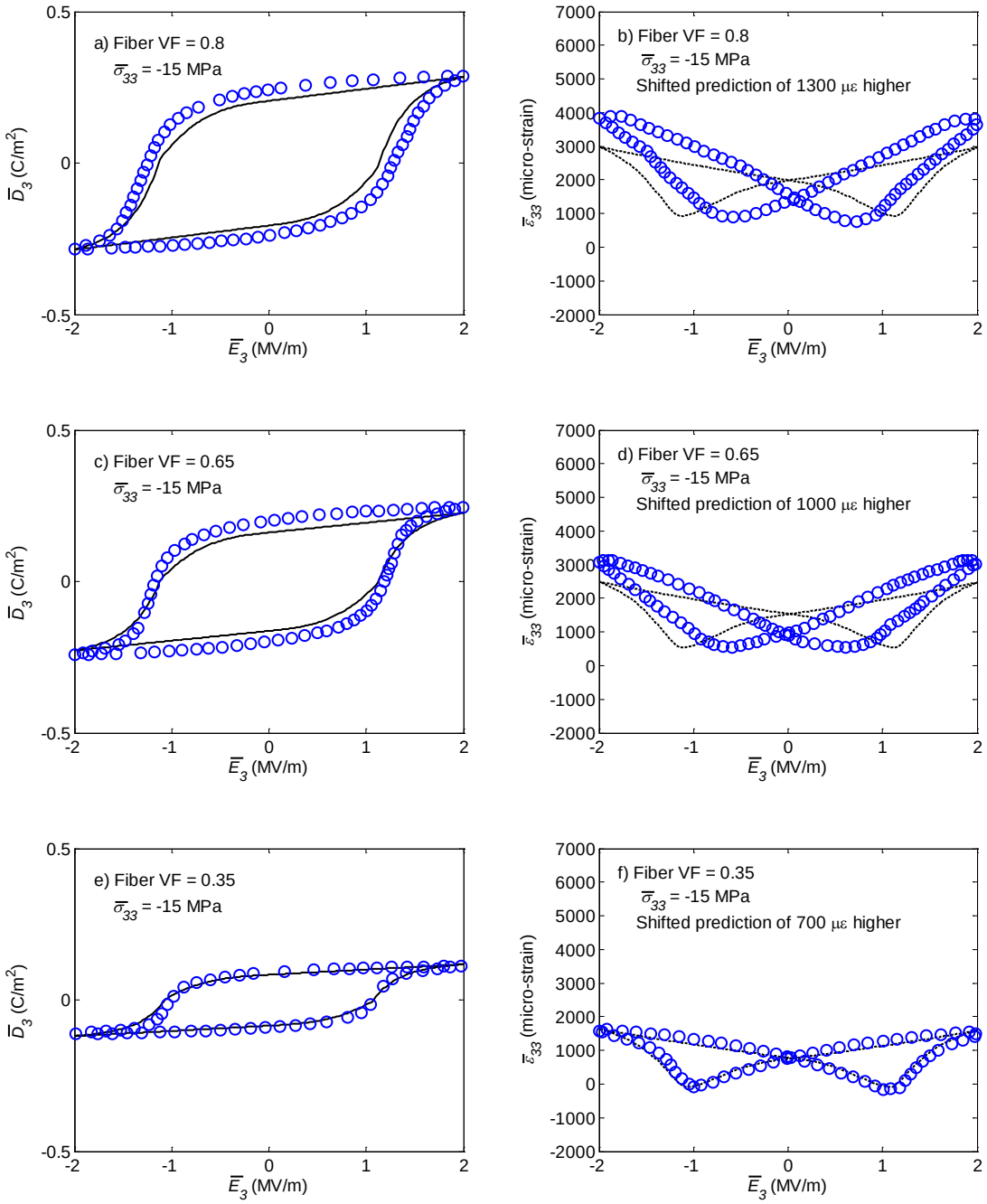

Figure 5.6 Comparison of micromechanical predictions (solid and dashed lines) to experimental data (circles) of Jayendiran and Arockiarajan (2013) for the hysteretic polarization and butterfly strain responses for the PZT-5A1/epoxy II 1-3 active composite with various PZT-5A1 fiber VFs subjected to both a cyclic electric field and a constant mechanical stress.

5.2 Parametric Studies

Since experimental data on nonlinear and time-dependent electromechanical hysteresis of 0-3 active composites are not available we conduct parametric studies on investigating the effects of the constituent compositions and properties and loading histories on the overall performance of both 1-3 and 0-3 active composites. Effective polarization switching responses of 0-3 piezocomposites and a special emphasis on the effect of dielectric constants of the matrix of 0-3 piezocomposites will be discussed in Section 5.2.1. Section 5.2.2 discusses the effect of loading history on the overall time-dependent polarization switching responses of 1-3 piezocomposites.

5.2.1 Polarization switching responses of 0-3 piezocomposites

We first examine the effect of constituent compositions for 0-3 active composites. For the purpose of comparison, we choose the 0-3 piezocomposites having the same properties of the constituents as the 1-3 piezocomposites discussed in the previous section, i.e., Section 5.1. The effective nonlinear electromechanical hysteretic responses for a stress free PZT-5A1/epoxy II 0-3 piezocomposites with various PZT-5A1 particle VFs = 0.65 and 0.35 under both a cyclic electric field with amplitude of $\bar{E}_3 = \pm 2$ MV/m along the poling direction (x_3 direction) and a constant compressive stress, $\bar{\sigma}_{33} = -15$ MPa are shown in Figure 5.7. Insignificant hysteretic responses are observed. This is due to the fact that in the 0-3 piezocomposites, the polymeric matrix, which has low dielectric constant (non-conductive), dominates the overall responses and as a result the epoxy matrix is unable to pass significant amount of electric charges to the active piezoelectric particles, accordingly small amount of polarization is experienced by

the piezoelectric particles. Unlike the responses of the 1-3 piezocomposites with the longitudinal fiber axis in x_3-direction, the piezoelectric fibers are directly subjected to the applied electric stimuli and consequently stronger hysteretic responses are observed.

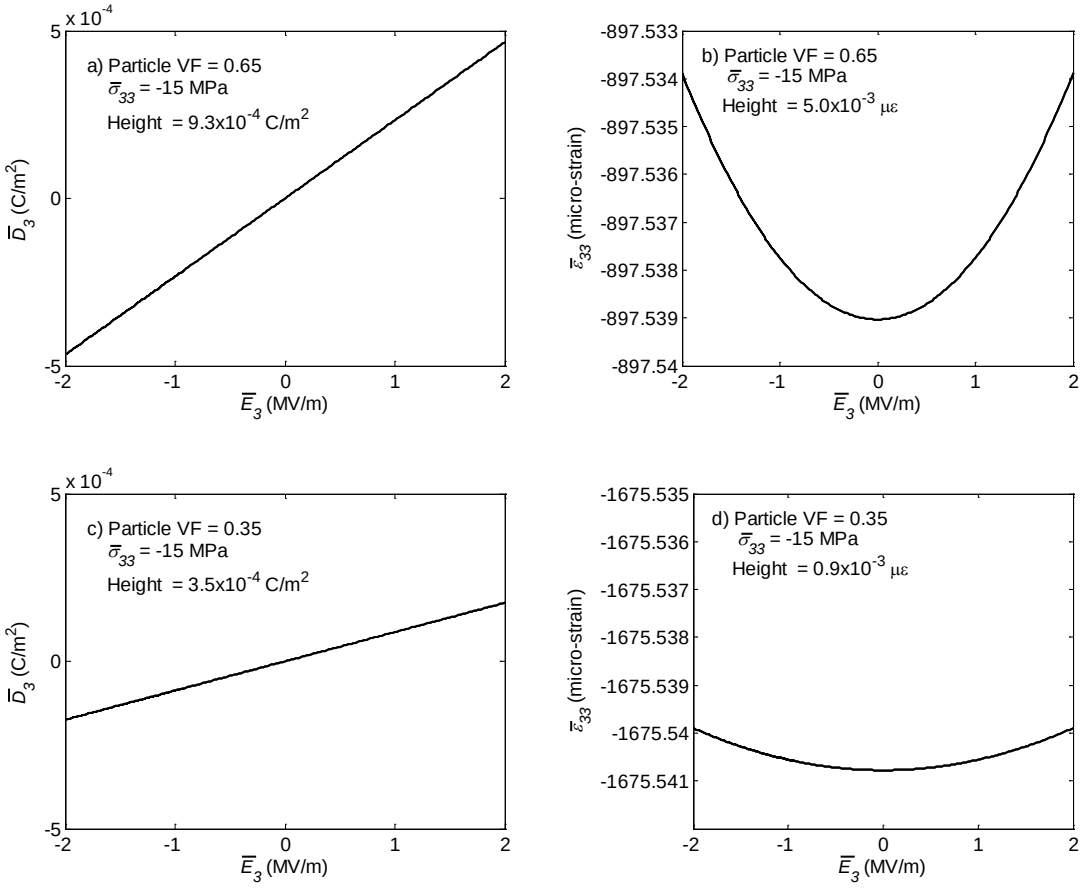

Figure 5.7 The effective polarization and strain responses for the stress free PZT-5A1/epoxy II 0-3 active composite with matrix dielectric constant of 0.04×10^{-9} F/m

Bent and Hagood (1997) mentioned that improving the inactive matrix materials by incorporating conductive fillers could reduce the needed voltage for poling and operation of active composites. In order to examine the influence of the dielectric constant of the homogeneous matrix, a matrix with high dielectric constant, i.e., 16.4×10^{-9} F/m, is considered while maintaining the same values for the remaining properties of the constituents. Figure 5.8 shows the effective nonlinear electro-mechanical hysteretic responses for a stress free 0-3 active composite with VF = 0.35 PZT-5A1 particles in the dielectric improved matrix under both a cyclic electric field with amplitude of $\overline{E}_3 = \pm 2$ MV/m and a constant compressive stress, $\overline{\sigma}_{33} = -15$ MPa. As expected more significant hysteretic responses are observed.

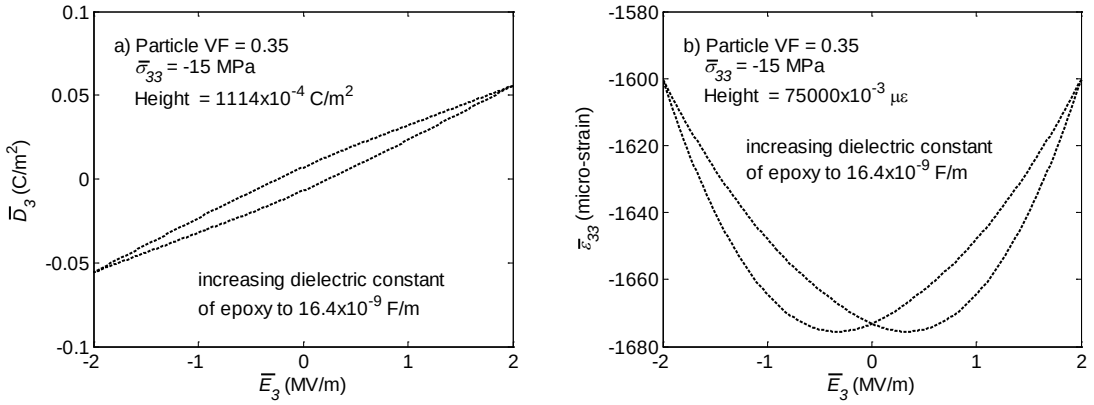

Figure 5.8 Effective hysteretic polarization and butterfly strain responses for the stress free PZT-5A1/epoxy II 0-3 active composite with PZT-5A1 particle VF = 0.35 with matrix dielectric constant of 16.4×10^{-9} F/m. The dielectric constant of the epoxy II matrix has been increased from 0.04×10^{-9} to 16.4×10^{-9} F/m.

We also present a parametric study by considering conductive metal, i.e., silver, as homogeneous matrix in 0-3 piezocomposites is also studied. The properties of the silver are referred to Davis (1998) and are listed in Table 4.4.The micromechanical predictions on effective hysteresis of a PZT-5A1/silver 0-3 active composite with PZT-5A1 particle VF = 0.35 and 0.1 subjected to both a constant compressive stress, $\bar{\sigma}_{33}$ = −45 MPa, and a cyclic electric field with amplitude of $\bar{E}_3 = \pm 2$ MV/m along the poling direction are shown in Figure 5.9. Even though the compressive stress can suppress the amount of polarization, the significant hysteretic responses are still observed. This confirms that high dielectric constant of the conductive matrix makes the electric charges easily pass through the conductive matrix and eventually large amount of electric fields reaches the PZT-5A1 particles. It is also seen that higher concentration of ferroelectric particles leads to stronger hysteretic responses, which is expected.

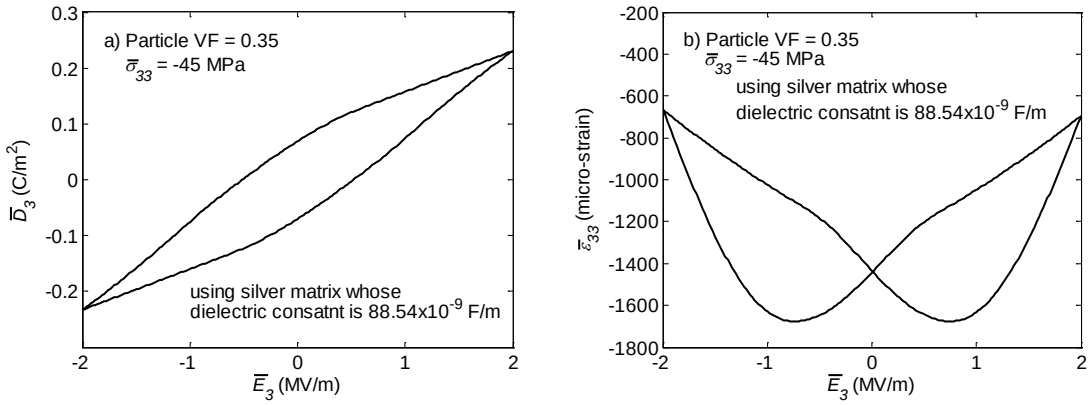

Figure 5.9 Effective hysteretic polarization and butterfly strain responses for the PZT-5A1/silver 0-3 active composite with PZT-5A1 particle undergoing both a cyclic electric field and a constant mechanical stress $\bar{\sigma}_{33}$ = −45 MPa.

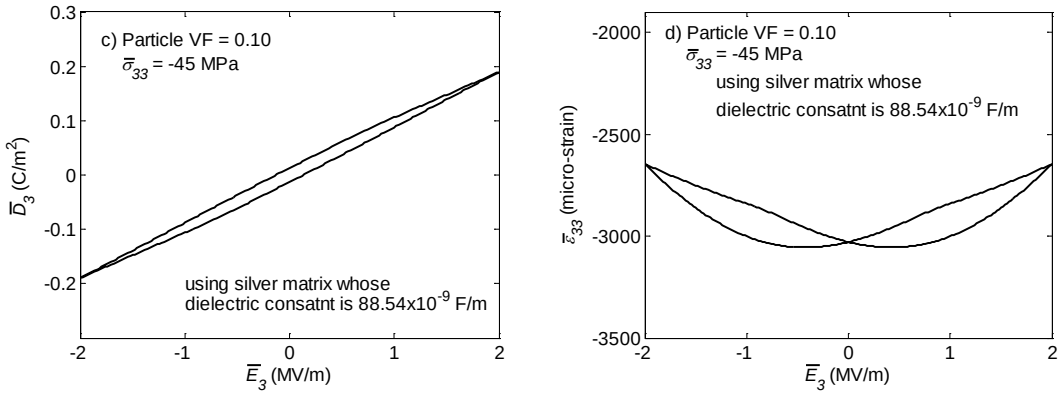

Figure 5.9 Continued.

5.2.2 Time-dependent and polarization switching responses of 1-3 piezocomposites

In order to examine the effect of loading history, i.e., various loading frequency and viscoelastic matrix, we consider a 1-3 active composite having rate-dependent PZT-51 fibers in a time-dependent FM73 polymer. The material properties of the PZT-51 inhomogeneities and the FM73 polymer are listed in from Table 5.6 to Table 5.9 and Table 4.6[11], respectively. The relation of the coercive electric field and the compressive stress is

$$E_c = \begin{cases} E_c^0 - 0.0041\left|\sigma_{33}^t\right|, & \sigma_{33}^t < 0, \\ E_c^0, & \sigma_{33}^t \geq 0. \end{cases} \tag{5.3}$$

[11] We only consider the first two terms of the series of exponential functions to the viscoelastic FM73 polymer in discussions on Section 5.2.2. This simplification will not affect us to qualitatively understand the influence of the viscoelastic constituent to the overall responses of piezocomposites but it will dramatically reduce computational cost.

Table 5.6 Material parameters for the time-dependent polarization of PZT-51 (Sohrabi and Muliana, 2013)

	E_c^0	κ_0	κ_1	τ_1	λ	η	μ	ω
	(MV/m)	($\times 10^{-9}$ F/m)		(sec)	($\times 10^{-6}$ F/m)		($\times 10^{-6}$ F/m)	
PZT-51	0.67	70	225	1	0.35	3	1.6	4

Table 5.7 Electro-mechanical coupling parameters for the time-dependent polarization of PZT-51 (Sohrabi and Muliana, 2013)

	d_{333}^r	d_{311}^r	κ_{11}^r	κ_{33}^r	P_r	C_1
	($\times 10^{-12}$ m/V)		($\times 10^{-9}$ F/m)		(C/m^2)	
PZT-51	1520	−570	38.0	42.0	0.194	0.19

Table 5.8 Elastic constants for the time-dependent polarization of PZT-51 (Sohrabi and Muliana, 2013)

	$E_{11} = E_{22}$	E_{33}	G_{12}	$G_{31} = G_{32}$	ν_{12}	
	(GPa)	(GPa)	(GPa)	(GPa)		$\nu_{31} = \nu_{32}$
PZT-51	34.48	33.00	13.19	12.37	0.307	0.334

Table 5.9 Material parameters above the coercive stress limit for the time-dependent polarization of PZT-51 (Sohrabi and Muliana, 2013)

	σ_c (MPa)	C_2	λ ($\times 10^{-6}$ F/m)	n	μ ($\times 10^{-6}$ F/m)	ω
PZT-51	25	0.3	0.40	3	1.1	4

The effective hysteretic responses of a stress free PZT-51/FM73 polymer 1-3 active composite with PZT-51 fiber VF = 0.5 subject to cyclic electric loadings $\bar{E}_3$ = 1.2sin($2\pi ft$) along the poling axis with different frequencies f = 0.5, 1 and 10 Hz are shown inFigure 5.10. It is seen that lower frequency loading leads to larger hysteretic response since slower loading allows for the materials to experience more pronounced time-dependent response. In this analysis, PZT-51 fibers experiences time-dependent polarization response and the matrix exhibits viscoelastic deformation. For the higher frequency loading, smaller hysteretic responses are seen and saturated (steady-state) condition is reached after the first cycle, indicating negligible time-dependent response. In the high frequency loading case the hysteretic response is mainly due to the irreversible polarization during polarization switching.

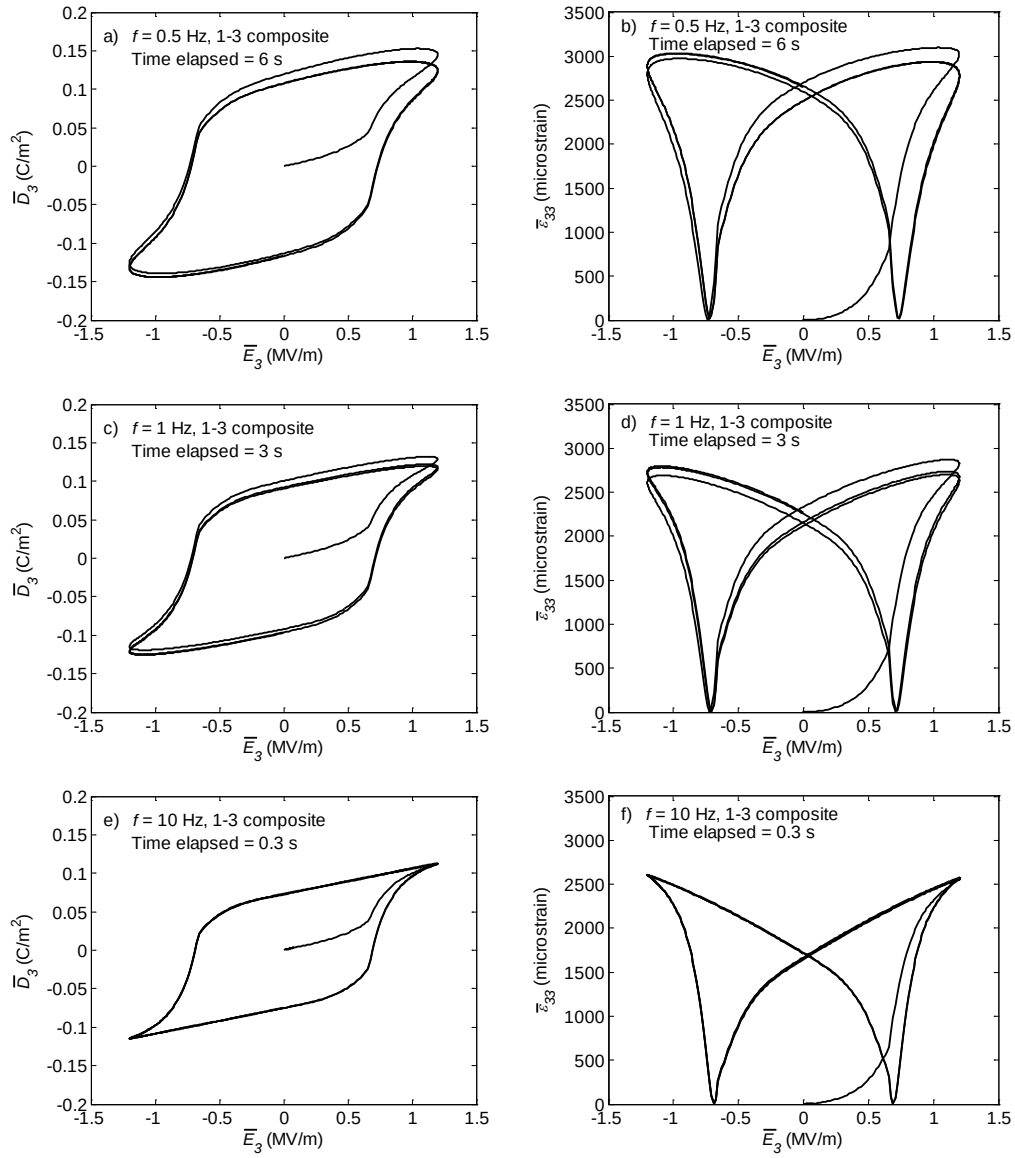

Figure 5.10 Frequency effect on the effective dielectric hysteresis and butterfly strain responses for the stress free PZT-51/FM 73 polymer 1-3 piezocomposite with VF = 0.5 undergoing a cyclic sinusoidal electric field. Only the first three cycles are plotted.

In order to examine the saturated condition for each excitation frequency, Figure 5.11 illustrates the amplitudes (maximum values) of the dielectric hysteresis and

butterfly strain responses against number of cycles. The initial drops in the effective amplitudes are due to time-dependent polarization effect in the PZT-51 fibers and then the amplitudes increase at later cycles because of the creep deformation effect in the FM73 polymer constituent. As the frequency increases, both the initial drops and subsequent creep-like responses are quite insignificant because of the short duration of loading. The different responses in the PZT-51 and FM73 polymer leads to complex hysteretic response of the active composites and several cycles are required to reach steady state.

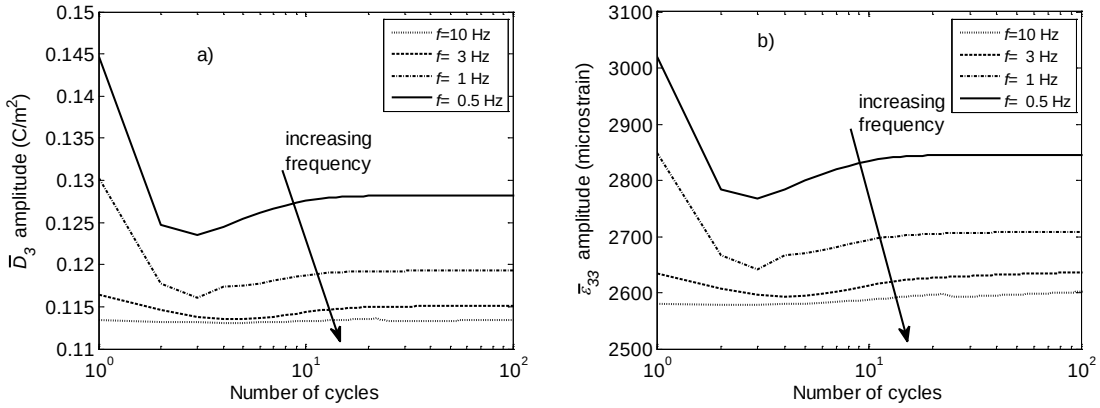

Figure 5.11 Effective amplitude of a) dielectric hysteresis and b) butterfly strain responses vs. number of cyclers for the stress free PZT-51/FM 73 polymer 1-3 piezocomposite with PZT-51 fiber VF = 0.5 undergoing a cyclic sinusoidal electric input. (Logarithmic scale on the horizontal axis)

CHAPTER VI

MICROMECHANICAL ANALYSES OF HYBRID PIEZOCOMPOSITES

This chapter illustrates the performance of the hybrid-unit-cell model by comparing the UC estimations to experimental findings from available literatures following by parametric studies in order to examine the effects of different responses of the constituents, microstructural arrangements, and loading histories on the overall nonlinear and hysteretic electromechanical responses of hybrid piezocomposites. The constitutive relations in Equations (2.1), (2.2), (2.3), and (2.4) are used for polarized piezoceramics and those in Equations (2.22) and (2.23) are used for simulating the polarization switching response of piezoceramics while those in Equations (2.47) and (2.48) are applied to inactive viscoelastic mediums.

6.1 Comparison with Experimental Data

Available experimental data for hybrid composites were primarily focused on the overall mechanical properties. The presented nonlinear hybrid-unit-cell model should be capable of predicting the overall properties of the hybrid composites without electromechanical coupling effect. Hussain et al. (1996) reported the effective longitudinal Young's modulus of a hybrid composite with unidirectional carbon fibers dispersed in an alumina/epoxy III matrix with the alumina particle VF = 0.1. Figure 6.1a depicts the comparisons of the longitudinal elastic moduli of the hybrid composite and a 1-3 composite obtained from the hybrid unit-cell model and experimental data.

For the 1-3 composite, a hybrid unit-cell with zero percent particle volume content is considered. Adding particle to the polymeric matrix slightly improves the effective longitudinal moduli of the hybrid composite. Since Hussain et al. (1996) did not report the constituent properties, we calibrate the transverse and longitudinal moduli (E_{22} *and* E_{33}) for the carbon fiber and the modulus (E) for the epoxy III by using the experimental data on the 1-3 composite with the carbon fiber VF = 0.41 shown in Figure 6.1a. The constituent properties used in the simulation are listed in Figure 6.1. The experimental data for the effective transverse moduli shown in Figure 6.1b were obtained from Hussain et al. (2000). Using the carbon fiber VF = 0.4 with the alumina particle VF = 0.1 shown in Figure 6.1a we further calibrate the elastic modulus of the alumina, which is 416 GPa[12]. The calibrated material properties are then used to evaluate the effective longitudinal and transverse moduli of the hybrid composite with different fiber volume contents, as shown in Figure 6.1 (indicated by solid lines). The hybrid unit-cell model can reasonably predict the effective elastic moduli of the hybrid and 1-3 composites. It is seen that adding stiffer particles to the polymeric matrix can significantly enhance the transverse modulus. Hussain et al. (2000) did not report the experimental data for the transverse moduli of the hybrid composite.

[12] Munro's (1997) experimental examination shown that the elastic modulus of the alumina is between 338 and 416 GPa.

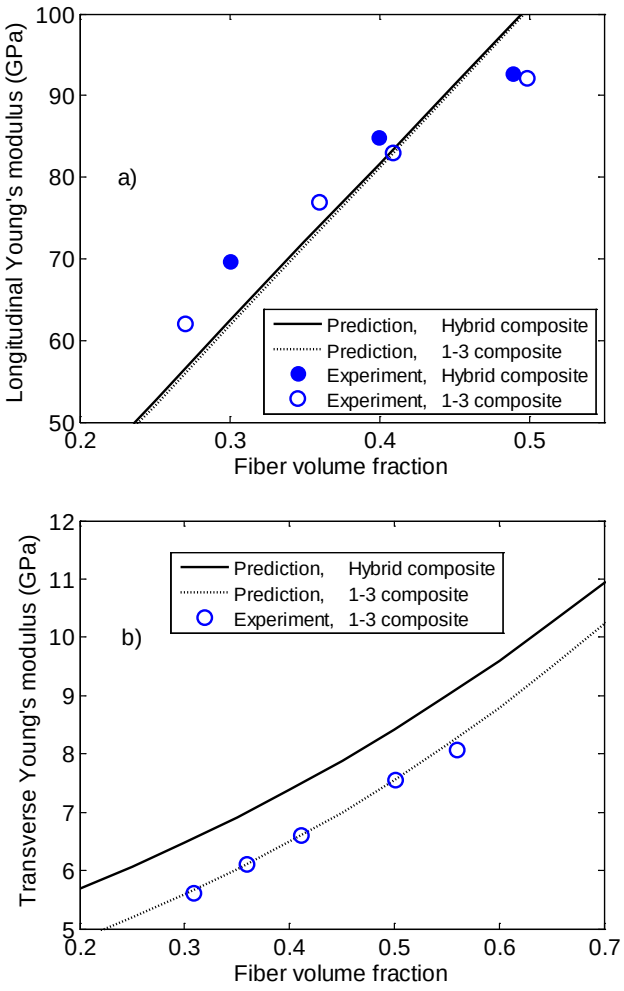

Figure 6.1 Comparison of the micromechanical predictions to the experimental data, a) Hussain et al. (1996) and b) Hussain et al. (2000), for the effective longitudinal elastic moduli for the carbon fiber/[alumina/epoxy III] hybrid (solid lines) and carbon fiber/epoxy III 1-3 (dotted lines) composites as a function of fiber volume fraction.

Table 6.1 Mechanical properties of the carbon fiber, epoxy III and alumina (The material properties are determined from Hussain et al., 1996 and 2000)

	Carbon fiber	
Longitudinal Young's modulus, E_{33} (GPa)	198	
Transverse Young's modulus, E_{22} (GPa)	16	
Major Poisson's ratio, v_{31}	0.20	
In-plane Poisson's ratio, v_{12}	0.25	
Longitudinal shear modulus, G_{31} (GPa)	28	
	Epoxy III	Alumina
Young's modulus, E (GPa)	3.4	416
Poisson's ratio, v	0.35	0.23

Since the experimental data for hybrid piezocomposites are not available, we conduct parametric studies (Section 6.2) on investigating the effects of constituent compositions and loading histories on the overall performance of hybrid piezocomposites.

6.2 Parametric Studies

Effective nonlinear responses of polarized hybrid piezocomposites are discussed in Section 6.2.1 and following by effective time-dependent responses due to viscoelastic constituent (i.e., FM73 polymer) of polarized hybrid piezocomposites, which are examined in Section 6.2.2. Time-dependent and polarization switching responses of

piezocomposites are presented in Section 6.2.3. The material used for parametric studies are polarized PZT-G1195, Araldite D, FM73 polymer, and PZT-51, and their material parameters have been listed in the previous chapters.

6.2.1 Nonlinear responses of polarized hybrid piezocomposites

We examine the effect of constituent compositions on the overall nonlinear electromechanical responses of a polarized hybrid piezocomposite subjected to large electric fields (i.e., 1 MV/m) but lower than coercive electric field (i.e., the constitutive relations in Equations (2.1) and (2.2) are used for polarized PZT fibers and particles). The matrix of the hybrid piezocomposite is first considered as elastic solid such as Araldite D while the polarized PZT-G1195 is used for the inhomogeneities. The material properties of the Araldite D and polarized PZT-G1195 used for simulations have been listed in Table 4.1 and discussed in Section 4.2, respectively.

Figure 6.2 shows the effective transverse stress $\overline{\sigma}_{11}$ and longitudinal stress $\overline{\sigma}_{33}$ due to an applied electric field $\overline{E}_3$ along the poling direction, which is the longitudinal fiber direction (x_3 axis) up to 1 MV/m for a fully constrained displacement of the PZT-G1195/[PZT-G1195/Araldite D] polarized hybrid piezocomposite with polarized PZT-G1195 fiber VF = 0.4 and several polarized PZT-G1195 particle VFs = 0-0.5. The linear response for the piezocomposite with zero content of polarized PZT-G1195 fillers is also shown for comparison. Figure 6.2a shows that as the filler VF increases the effective transverse stress $\overline{\sigma}_{11}$ is significantly enhanced while the effective longitudinal stress $\overline{\sigma}_{33}$ is insensitive to the existence of polarized piezoelectric fillers even for higher particle

contents, as shown in Figure 6.2b. This is due to the fact that the transverse stress $\bar{\sigma}_{11}$ is a matrix-dominated response and high stiffness of the polarized PZT-G1195 fillers increases the stiffness of the overall matrix. In contrast, the longitudinal stress $\bar{\sigma}_{33}$ is a fiber-dominated response and insignificant improvements in the longitudinal properties are shown with adding polarized PZT-G1195 fillers. Thus, dispersing stiffer fillers into a softer matrix in a 1-3 piezocomposite will be useful for improving the blocked stress for the 3-1 operating mode.

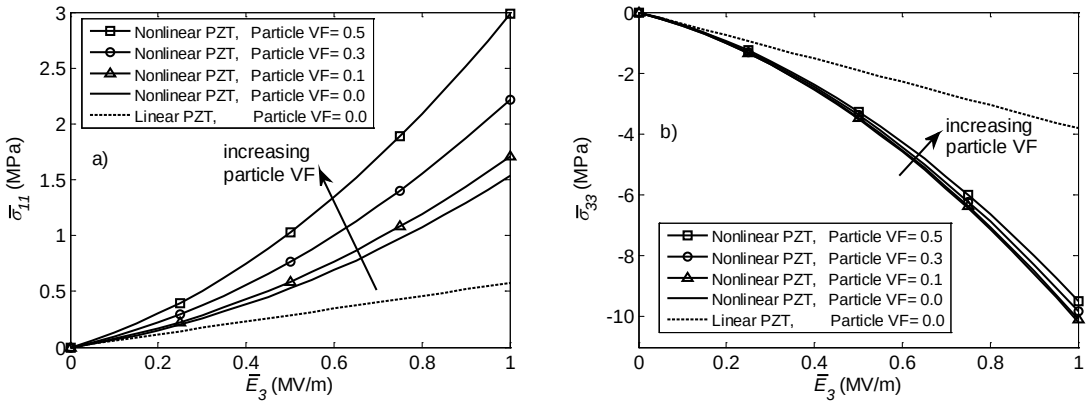

Figure 6.2 Effective a) transverse stress $\bar{\sigma}_{11}$ and b) longitudinal stress $\bar{\sigma}_{33}$ responses for the fully constrained displacement of the PZT-G1195/[PZT-G1195/Araldite D] polarized hybrid piezocomposite with a PZT-G1195 fiber VF = 0.4 and various PZT-G1195 particle VFs under an applied electric field $\bar{E}_3$

We also consider a stress free boundary condition for a PZT-G1195/[PZT-G1195/Araldite D] polarized hybrid piezocomposite with polarized PZT-G1195 fiber VF = 0.4 and polarized PZT-G1195 particle VF varies from 0 to 0.5, subjected to an applied

electric field $\overline{E}_3$ along the poling direction up to 1 MV/m. Figure 6.3 depicts the effective transverse strain $\overline{\varepsilon}_{11}$ and longitudinal strain $\overline{\varepsilon}_{33}$. The absolute values of the effective strains $\overline{\varepsilon}_{11}$ and $\overline{\varepsilon}_{33}$ both decrease as the polarized PZT-G1195 fillers increase. This is because adding polarized PZT-G1195 particles in the matrix increases the stiffness of the matrix and leads to a stiffer polarized hybrid piezocomposite, which causes less actuation strains under the same electric field input. It is known that in piezoelectric materials larger blocked stresses are accompanied by smaller free strains, and vice versa. Adding stiffer fillers, i.e., PZTs, into a relatively soft matrix, i.e., polymer, in a 1-3 piezocomposite is done to improve the transverse blocked stress.

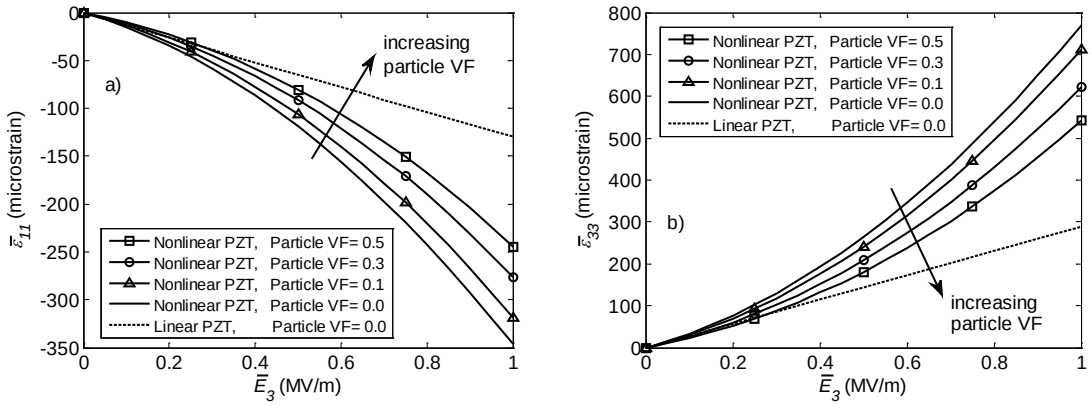

Figure 6.3 Effective a) transverse strain $\overline{\varepsilon}_{11}$ and b) longitudinal strain $\overline{\varepsilon}_{33}$ responses for the stress free PZT-G1195/[PZT-G1195/Araldite D] polarized hybrid piezocomposite with a PZT-G1195 fiber VF = 0.4 and various PZT-G1195 particle VFs, under an applied electric field $\overline{E}_3$.

6.2.2 Time-dependent responses of polarized hybrid piezocomposites

In order to study the time-dependent responses due a viscoelastic constituent in a polarized hybrid piezocomposite, viscoelastic FM73 polymer is used for the polymer constituent. It should be noted that for the viscoelastic FM73 polymer, only the first two terms of the series of exponential functions are considered in this Section 6.2.2 in order to reduce computational cost. Fully constrained PZT-G1195/[PZT-G1195/FM73 polymer] polarized hybrid piezocomposites with polarized PZT-G1195 fiber VF = 0.4 and polarized PZT-G1195 particle filler VFs = 0 and 0.5 are subjected to a cyclic electric field, $\bar{E}_3(t) = -0.5\cos(2\pi ft)+0.5$ MV/m along the poling direction with various frequencies f = 0.5, 1 and 10 Hz. The response of the effective transverse stress $\bar{\sigma}_{11}$ amplitude (maximum stress) as a function of number of cycles at different loading frequencies is shown in Figure 6.4. As the number of cycles increase (longer duration of loading), the stress amplitude decreases until it reaches steady value, i.e., fully relaxed stress state. Higher frequency leads to more cycles needed to reach steady state, which is expected since slow input would give enough time for the viscoelastic polymers to experience stress relaxation. The polarized hybrid piezocomposite (Figure 6.4a) and the polarized 1-3 piezocomposite (Figure 6.4b) experience the same trends under cyclic loading with higher effective blocked stress $\bar{\sigma}_{11}$ in the polarized hybrid piezocomposite.

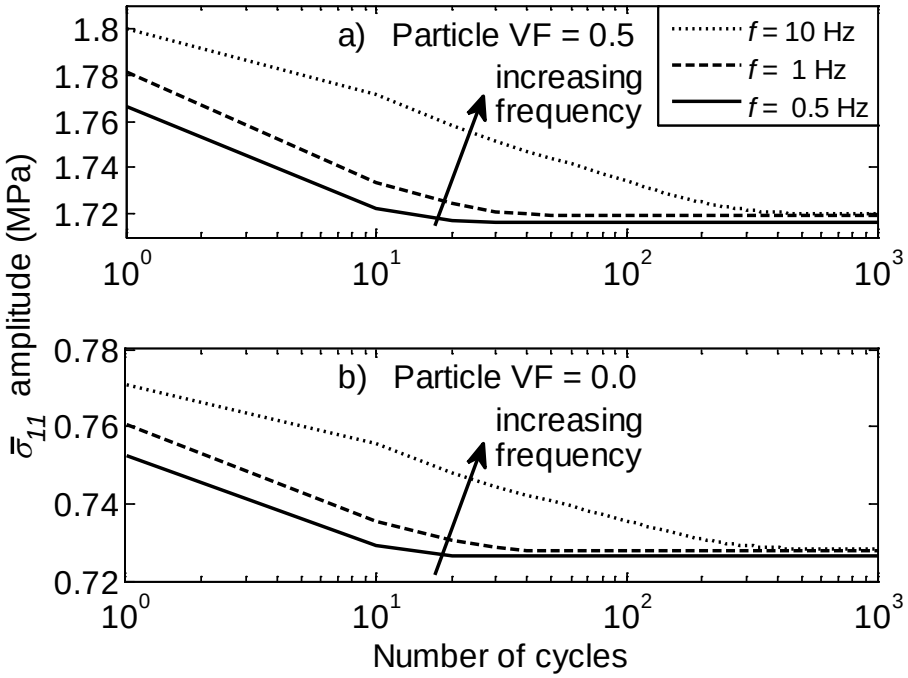

Figure 6.4 Effective transverse stress $\bar{\sigma}_{11}$ amplitude vs. number of cycles for the fully constrained displacement of the PZT-G1195/[PZT-G1195/FM73 polymer] hybrid piezocomposite with PZT-G1195 fiber VF = 0.4 and various polarized PZT-G1195 particle VFs, a) 0.0 and b) 0.5, due to a cyclic electric field with various frequencies *f* = 0.5, 1 and 10 Hz along the poling direction.

6.2.3 Time-dependent and polarization switching responses of hybrid piezocomposites

This section discusses the overall hysteretic polarization switching and butterfly strain responses of a hybrid piezocomposite with various constituent compositions and under different loading histories. The constitutive relations in Equations (2.22) and (2.23) are used for polarization switching response of PZT-51 fibers and particles. The matrix of the hybrid piezocomposite is considered as FM73 polymer. Again, for the

viscoelastic FM73 polymer, only the first two terms of the series of exponential functions are considered in this section.

Figure 6.5depicts steady state electric displacement and longitudinal strain responses of a stress free boundary condition for a PZT-51/[PZT-51/FM73 polymer] hybrid piezocomposite with PZT-51 fiber VF = 0.4 and PZT-51 particle VFs = 0.0, 0.2 and 0.4, subject to a cyclic electric loading $\bar{E}_3 = 1.2\sin(2\pi ft)$ MV/m along the longitudinal fiber direction (x_3 direction) with the frequency f = 1 Hz. It is expected that the heights of the butterfly curves (Figure 6.5b, d, f) of the hybrid piezocomposite decrease as PZT-51 particles increase because PZT-51 fillers increase the overall stiffness of the matrix. In contrast, the polarization responses (Figure 6.5a, c, e) are only slightly influenced by the adding the active fillers since the response is dominated by the fibers. At the saturated (steady state) condition, the strains in the butterfly curves at the coercive electric field limit are slightly higher than zero, which are due to the time-dependent PZT-51 and FM73 polymer materials. Even though the hybrid composites are under stress-free boundary conditions, the heterogeneity in the composites leads to existence of internal stresses when an electric field is applied. Several discontinuities in the hysteretic polarization and butterfly curves are observed in Figure 6.5g and h, respectively, when PZT-51 particle VF increases to 0.55. These discontinuities occur when the magnitude of compressive stress σ_{33}^t in the PZT-51 fiber exceeds the coercive stress limit (σ_c = 25 MPa for PZT-51) either from $\sigma_{33}^t > -\sigma_c$ to $\sigma_{33}^t \le -\sigma_c$ or from $\sigma_{33}^t \le -\sigma_c$ back to $\sigma_{33}^t > -\sigma_c$. When the compressive stress σ_{33}^t in the PZT-51 fiber is greater than the coercive stress limit, polarization switching occurs, whose effect is

incorporated in Equations (2.32) and (2.33). Changes in the material parameters, when a compressive stress is higher than the coercive stress limit, lead to discontinuities in the electromechanical responses. This issue has been discussed in Sohrabi and Muliana (2013).

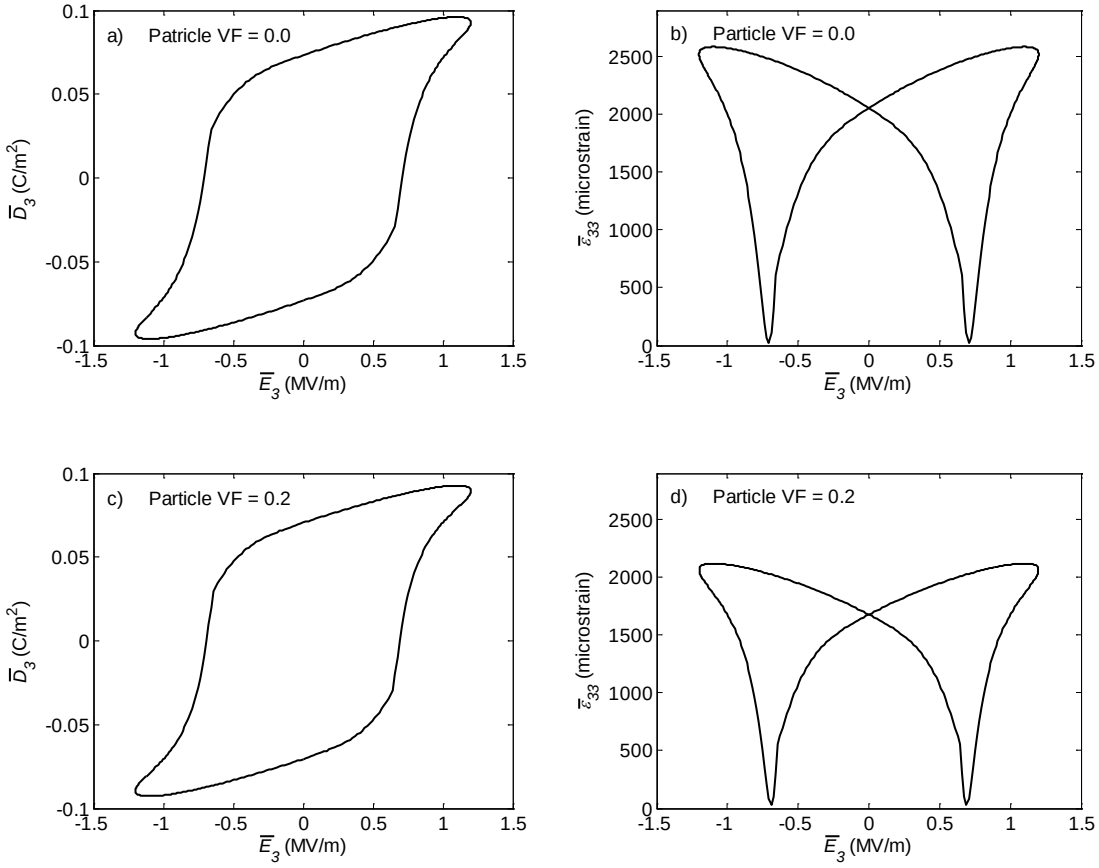

Figure 6.5 Effective a, c, e, g) electric displacement $\bar{D}_3$ and b, d, f, h) longitudinal strain $\bar{\varepsilon}_{33}$ responses for the stress free PZT-51/[PZT-51/FM73 polymer] hybrid piezocomposite with a PZT-51 fiber VF = 0.4 and various PZT-51 particle VFs due to a cyclic electric loading with frequency *f* = 1 Hz. 100 cycles are needed to reach steady state.

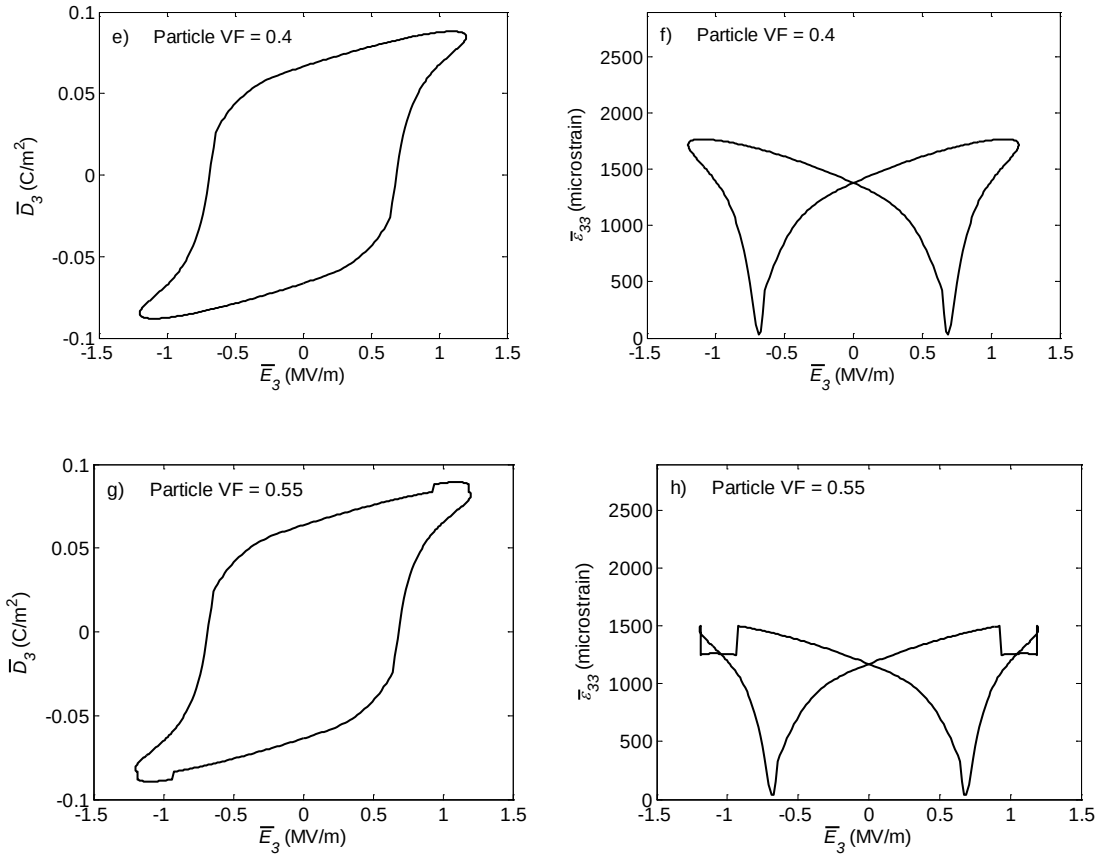

Figure 6.5 Continued.

Next, this study examines the effect of prescribing compressive stresses on the overall nonlinear rate-dependent hysteretic electromechanical responses of a PZT-51/[PZT-51/FM73 polymer] hybrid piezocomposite with PZT-51 fiber VF = 0.4 and PZT-51 particle VF = 0.2, subjected to a cyclic electric loading $\bar{E}_3 = 1.2 \sin(2\pi ft)$ MV/m along the fiber direction with the frequency $f = 1$ Hz and constant compressive stresses $\bar{\sigma}_{33} = 0, -15$ and -30 MPa. Figure 6.6 shows the steady state electric displacement and longitudinal strain responses after 100 cycles. The compressive stresses limit the amount

of polarization to be generated from electric field inputs, as a result smaller hysteretic polarization and butterfly strain curves are observed when higher compressive stress is applied.

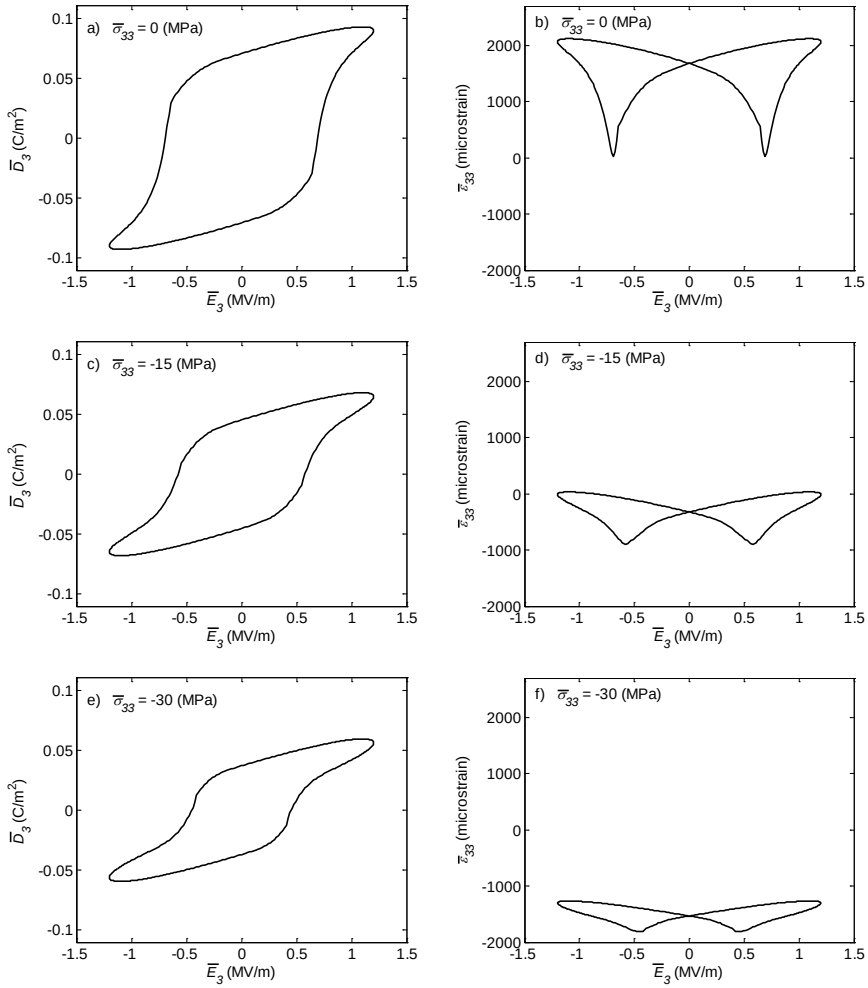

Figure 6.6 Effective a, c, e) electric displacement $\bar{D}_3$ and b, d, f) longitudinal strain $\bar{\varepsilon}_{33}$ responses for the PZT-51/[PZT-51/FM73 polymer] hybrid piezocomposite with PZT-51 fiber VF = 0.4 and PZT-51 particle VF = 0.2 subjected to both a cyclic electric loading with frequency *f* = 1 Hz and various constant mechanical stresses. Around 100 cycles are needed to reach steady state.

This study also presents the effect of frequencies on the overall hysteretic electromechanical responses of a hybrid piezocomposite. A stress free PZT-51/[PZT-51/FM73 polymer] hybrid piezocomposite with PZT-51 fiber VF = 0.4 and PZT-51 particle VF = 0.2 subjected to cyclic electric loadings $\bar{E}_3 = 1.2 \sin(2\pi ft)$ along the fiber axis with different frequencies f = 0.5, 1 and 10 Hz is considered. Figure 6.7 depicts the responses of the polarization and longitudinal strain for the first six cycles. Lower frequency loading leads to larger hysteretic response since slower loading allows for the materials to experience more pronounced time-dependent response. In this analysis, PZT fibers and particles experiences creep-like polarization response while the matrix exhibits viscoelastic deformation. For the higher frequency loading, smaller hysteretic responses are seen and saturated (steady-state) condition is reached after a first few cycle, indicating negligible time-dependent response. In high frequency loading cases, the hysteretic response is mainly due to the irreversible polarization during polarization switching as discussed in Section 5.2.2.

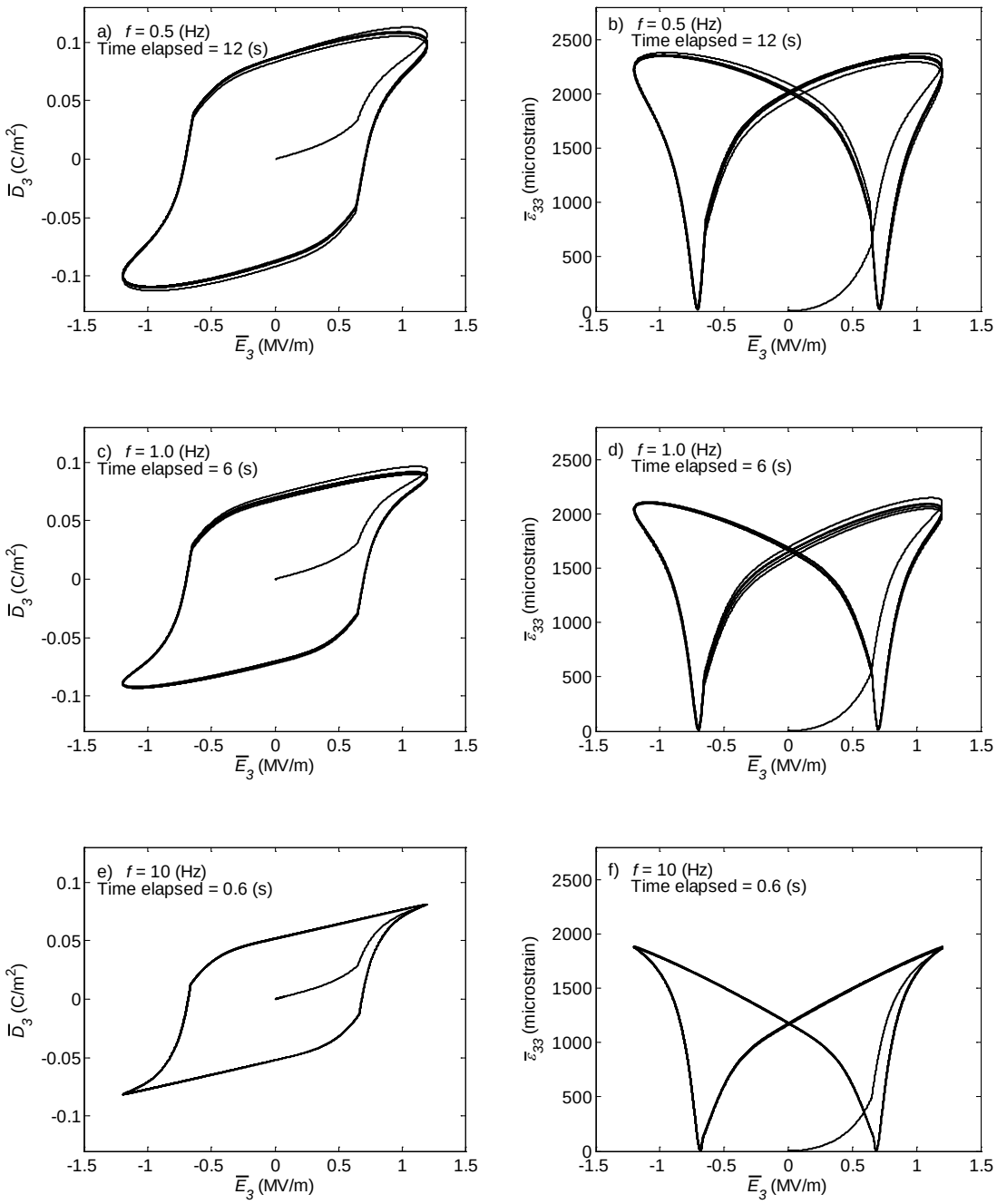

Figure 6.7 Effective a, c, e) electric displacement $\overline{D}_3$ and b, d, f) longitudinal strain $\overline{\varepsilon}_{33}$ responses for the stress free PZT-51/[PZT-51/FM73 polymer] hybrid piezocomposite with PZT-51 fiber VF = 0.4 and PZT-51 particle VF = 0.2 subjected to a cyclic electric loading with various frequencies *f*. The first six cycles are plotted.

The evolution of the amplitude of the effective strain of the butterfly strain response at various cycles is studied. A PZT-51/[PZT-51/FM73 polymer] hybrid piezo-composite with PZT-51 fiber VF = 0.4 and PZT-51 particle VF = 0.2 under a cyclic electric loading $\overline{E}_3(t) = 1.2 \sin(2\pi ft)$ MV/m with frequency $f = 1$ Hz is used in the analysis. Figure 6.8 depicts the normalized effective strain amplitude[13] at various cycles. The initial drop in the normalized effective strain amplitude is due to time-dependent polarization effect in the PZT-51 fibers and then the strain amplitude increases at later cycles because of the creep deformation effect in the FM73 polymer.

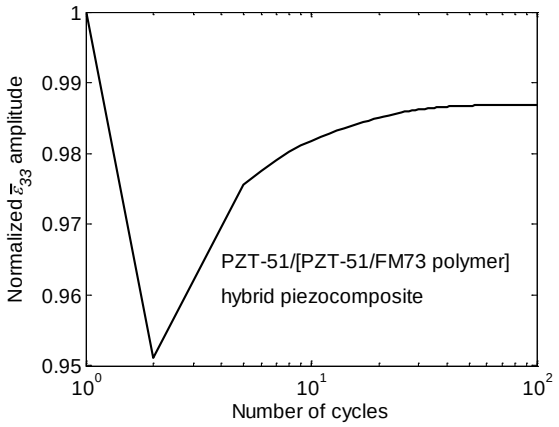

Figure 6.8 Normalized effective longitudinal strain $\overline{\varepsilon}_{33}$ amplitude vs. number of cyclers for the stress free PZT-51/[PZT-51/FM73 polymer] hybrid piezocomposite with PZT-51 fiber VF = 0.4 and PZT-51 particle VF = 0.2 due to a cyclic electric loading with frequency $f = 1$ Hz

[13] The normalized strain $\overline{\varepsilon}_{33}$ amplitude is normalized with respect to the maximum strain $\overline{\varepsilon}_{33}$ in the first cycle.

For further explanation, it is seen in Figure 6.9a that the strain amplitude in the PZT-51 constituent under cyclic electric field decreases before reaching steady state, while the strain amplitude in the FM73 polymer matrix constituent (Figure 6.9b) under cyclic stress input increases with increasing number of cycles. The different responses in the PZT-51 and FM73 polymer leads to complex hysteretic responses of the hybrid composites and higher number of cycles is required to reach steady state.

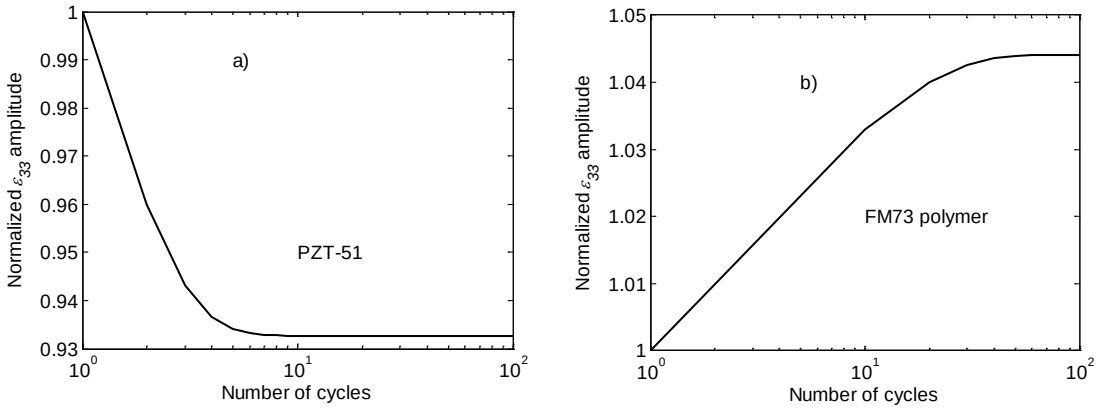

Figure 6.9 Normalized strain amplitude vs. number of cyclers. a) Pure PZT-51 subject to a cyclic electric loading with frequency *f* = 1 Hz. b) Pure FM73 polymer subject to a cyclic mechanical loading with frequency *f* = 1 Hz.

CHAPTER VII

ANALYSES OF FUNCTIONALLY GRADED PIEZOELECTRIC BEAMS

One type of the piezoelectric beams is a piezoelectric bimorph beam, which is formed by bonding two piezoelectric ceramic plates. An actuating mechanism is in the form of the lateral deflection of the bimorph beam, which results from one piezoelectric ceramic plate elongating due to a positive electric field while another one contracting from a negative electric field. Large bending displacements make the piezoelectric bimorph beam a good candidate in actuating applications. However, the large bending displacement achieved by large relative deformation (tension/compression) of the two piezoelectric ceramic plates, which is induced by large applied electric field leads to high stresses generated at the interface between the two piezoelectric ceramic plates. The high stresses at the interface can cause debonding of the two piezoelectric ceramic plates and eventually failure of the piezoelectric bimorph beam. Functionally graded material (FGM) appears one of the solutions to relieve the high stresses at the interface of piezoelectric ceramic plates by introducing gradual changes in the compositions of the piezoelectric ceramic plates, for example, Wu et al. (1996) and Takagi et al. (2003). Due to insignificant stress discontinuities at the interfaces in FGM, failures due to debonding or from high stresses developed in a conventional piezoelectric bimorph beam are avoided.

7.1 Formulation of Piezocomposite Beams

The effective response of functionally graded piezoelectric beams is determined by using laminate plate theory. This section summaries the equations that govern the deformations of functionally graded piezoelectric beams, which are adopted from Ballas (2007) for modeling multilayer piezocomposite beams. We consider the problem of the beam bending in one plane only and assume that the beam deflection follows the Euler-Bernoulli beam theory. Figure 7.1 depicts a functionally graded piezoelectric beam. In order to incorporate the electro-mechanical response, the unit-cell model of particulate composites is used to estimate the effective properties of each polarized piezocomposite lamina (macro level) and then the electric fields are applied to laminate plate theory to determine the curvature referring to the x_1-axis and the deflection with respect to x_3-axis of the beam (structural level).

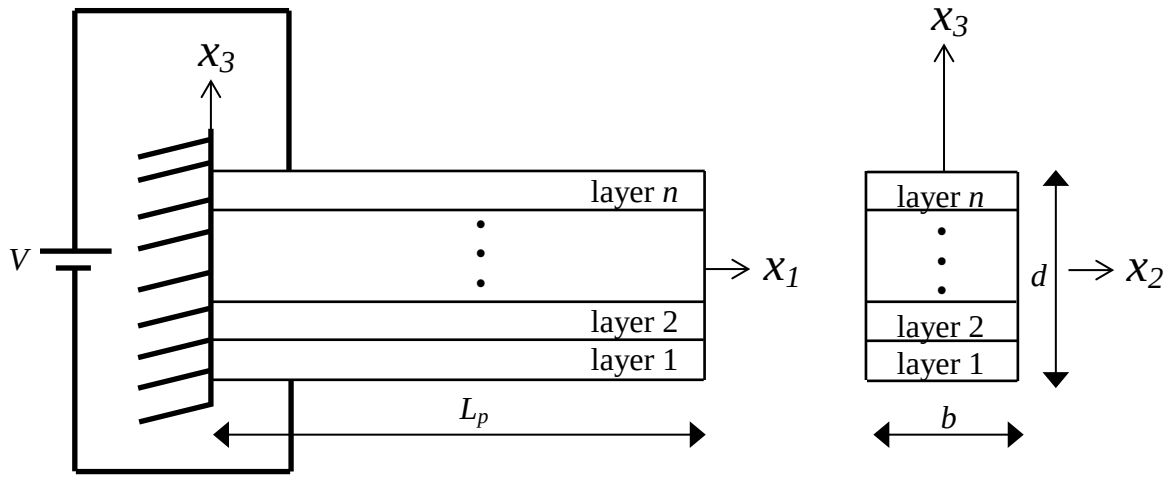

Figure 7.1 Sketch of the functionally graded piezoelectric bender.

Appling the conservation of linear and angular momenta along the x_1-axis and with respect to the x_2-axis, respectively, gives

$$\sum_{k=1}^{n} \int \sigma_{11}^{(k)} dA^{(k)} = N_1, \tag{7.1}$$

$$\sum_{k=1}^{n} \int \sigma_{11}^{(k)} x_3 dA^{(k)} = M_2, \tag{7.2}$$

where the superscript k indicates the kth lamina and n is the number of total lamina. $A^{(k)}$ is the area of cross section of the kth lamina with unit normal direction is in the x_1 axis. N_1 and M_2 are the resulting internal force along the neutral axis and moment with respect to the x_2-axis, respectively. Using a linearized constitutive equation, Equations (7.1) and (7.2) can be rewritten as

$$\sum_{k=1}^{n} \int E_{11}^{(k)} \left(\varepsilon_{11}^{0} - x_3 \kappa_1 + {}^{e}\varepsilon_{11}^{(k)} \right) dA^{(k)} = N_1, \tag{7.3}$$

$$\sum_{k=1}^{n} \int E_{11}^{(k)} \left(\varepsilon_{11}^{0} - x_3 \kappa_1 + {}^{e}\varepsilon_{11}^{(k)} \right) x_3 dA^{(k)} = M_2, \tag{7.4}$$

where $E_{11}^{(k)}$ is elastic modulus along the x_1-direction of the kth lamina, ε_{11}^{0} is the elastic strain along the neutral axis (i.e., x_1-axis) of the beam, κ_1 is the curvature referring to the x_1-axis of the beam, ${}^{e}\varepsilon_{11}^{(k)}$ is the electric-induced strain of the kth lamina along the x_1-direction due to an applied electric field $E_3^{(k)}$ in the kth lamina, which is evaluated via

$${}^{e}\varepsilon_{11}^{(k)} = \tilde{d}'^{(k)}_{311} E_3^{(k)}, \tag{7.5}$$

where $\tilde{d}'^{(k)}_{311}$ is linearized piezoelectric strain coefficient of the k^{th} lamina. The unit-cell model is implemented in each lamina in order to determine the ${}^{e}\varepsilon_{11}^{(k)}$. Due to the rectangular cross-section of the beam, the integrations in Equations (7.3) and (7.4) are written in a matrix form as

$$\begin{bmatrix} A & -B \\ B & D \end{bmatrix} \begin{Bmatrix} \varepsilon_{11}^{0} \\ \kappa_1 \end{Bmatrix} = \begin{Bmatrix} N_1 - N_1^e \\ M_2 - M_2^e \end{Bmatrix}, \tag{7.6}$$

where

$$A = b\sum_{k=1}^{n} E_{11}^{(k)} \left(x_3^{(k)} - x_3^{(k-1)} \right), \tag{7.7}$$

$$B = \frac{b}{2}\sum_{k=1}^{n} E_{11}^{(k)} \left(x_3^{(k)^2} - x_3^{(k-1)^2} \right), \tag{7.8}$$

$$D = -\frac{b}{3}\sum_{k=1}^{n} E_{11}^{(k)} \left(x_3^{(k)^3} - x_3^{(k-1)^3} \right), \tag{7.9}$$

$$N_1^e = b\sum_{k=1}^{n} E_{11}^{(k)}\, {}^{e}\varepsilon_{11}^{(k)} \left(x_3^{(k)} - x_3^{(k-1)} \right), \tag{7.10}$$

$$M_2^e = \frac{b}{2}\sum_{k=1}^{n} E_{11}^{(k)}\, {}^{e}\varepsilon_{11}^{(k)} \left(x_3^{(k)^2} - x_3^{(k-1)^2} \right). \tag{7.11}$$

The upper right superscript e in Equations (7.10) and (7.11) indicates that the force N_1^e and the moment M_2^e are due to the electromechanical coupling effect. The parameter b is the width of the beam. It should be noted that the internal force N_1 is assumed to have been applied at the neutral axis. However, if this force is applied eccentrically, a

corresponding moment with respect to the x_2-axis must be added to compensate for the eccentricity. The curvature κ_1 can be determined through

$$\begin{Bmatrix} \varepsilon_{11}^0 \\ \kappa_1 \end{Bmatrix} = \begin{bmatrix} A & -B \\ B & D \end{bmatrix}^{-1} \begin{Bmatrix} N_1 - N_1^e \\ M_2 - M_2^e \end{Bmatrix}. \tag{7.12}$$

For a cantilever functionally graded piezocomposite beam, the maximum deflection determined by

$$\delta_{\max} = \frac{\kappa_1}{2} L_p^2 \tag{7.13}$$

where L_p is the length along the x_1-axis of the beam. The electric field in each lamina can be approximated by using a series combination of capacitors model, that is, the functionally graded piezoelectric beam is view as a circuit having a series combination of capacitors which represent the laminae together with a battery source which represents the total applied voltage across the laminae. Thus, the potential differences across the laminate and the *k*th lamina are written as:

$$V = Q \sum_{k=1}^{n} \frac{1}{C^{(k)}}, \tag{7.14}$$

$$V^{(k)} = Q \frac{1}{C^{(k)}}, \tag{7.15}$$

where Q is the charge which should be same in each lamina. $C^{(k)}$ is the capacitance of the *k*th lamina and is given by

$$C^{(k)} = \frac{\tilde{\kappa}_{33}^{(k)} A^{(k)}}{d^{(k)}}, \tag{7.16}$$

where $\tilde{\kappa}_{33}^{(k)}$ is the second-order dielectric coefficients in the x_3-direction calibrated at constant stresses, which is determined from the unit-cell morel and $d^{(k)}$ is thickness of the k^{th} lamina. The electric field in the x_3-direction over the k^{th} lamina is

$$E_3^{(k)} = \frac{V^{(k)}}{d^{(k)}}. \tag{7.17}$$

Substituting $V^{(k)}$ from Equation (7.15) into (7.17) gives

$$E_3^{(k)} = \frac{Q}{d^{(k)} C^{(k)}}. \tag{7.18}$$

Substituting Equation (7.14) into (7.18) to eliminate Q gives

$$E_3^{(k)} = \frac{V}{d^{(k)} C^{(k)} \sum_{k=1}^{n} \frac{1}{C^{(k)}}}. \tag{7.19}$$

Substituting $C^{(k)}$ from Equation (7.16) into (7.19) gives

$$E_3^{(k)} = \frac{V}{\tilde{\kappa}_{33}^{(k)} A^{(k)} \sum_{k=1}^{n} \frac{1}{\frac{\tilde{\kappa}_{33}^{(k)} A^{(k)}}{d^{(k)}}}}. \tag{7.20}$$

If $A^{(k)}$ is a constant for all lamina, Equation (7.20) can be further simplified to

$$E_3^{(k)} = \frac{V}{\tilde{\kappa}_{33}^{(k)} \sum_{k=1}^{n} \frac{d^{(k)}}{\tilde{\kappa}_{33}^{(k)}}}, \tag{7.21}$$

where

$$d^{(k)} = x_3^{(k)} - x_3^{(k-1)}. \tag{7.22}$$

Equation (7.21) is used to determine the average electric field in each lamina[14]. Due to the nonlinear polarized piezoelectric constitutive model, i.e., Equations (2.1) and (2.2) used for the piezoelectric phase, this formulation leads to an implicit problem: $E_3^{(k)}$ depends on the $\tilde{\kappa}_{33}^{(k)}$, and at the same time $\tilde{\kappa}_{33}^{(k)}$ depends on $E_3^{(k)}$. This implicit problem is solved with a fixed-point method. The convergence is achieved when the norm of $E_3^{(k),n} - E_3^{(k),n+1}$ is smaller than a threshold value 10^{-6}.

7.2 Comparison with Experimental Data

Alexander and Brei (2005) developed two functionally graded piezoelectric beams. Each layer of the beam is constituted of 0-3 piezocomposites, which are made by mixing PZT-856 and barium titanate (BT) powder by powder metallurgy. Two opposing sides of the beam were electroded with 1500 Å of AuPd. The poling direction of each layer is toward the x_3-axis. Figure 7.2 depicts the 0-3 compositions of each ply and the dimension of each beam. The properties of the PZT-856 which are reported by Alexander and Brei (2005) and referred to manufacturer's data sheet are listed in Table 7.1.

[14] Through the concentration tensor (e.g., (3.52)) we can further determine the average electric fields of each phase (i.e., inhomogeneity or matrix) via each lamina. However, how much electric field reaching each grain from each constituent phase or further how much electric field reaching each dipole from each grain are out of scope of this study. The electric fields in the grain or dipole are usually classified as internal electric fields in contrast with external electric fields of the constituent phase or lamina. In this study, we neglect the complex internal electric fields and only focus on the average electric fields over each constituent phase or lamina so-called external electric fields.

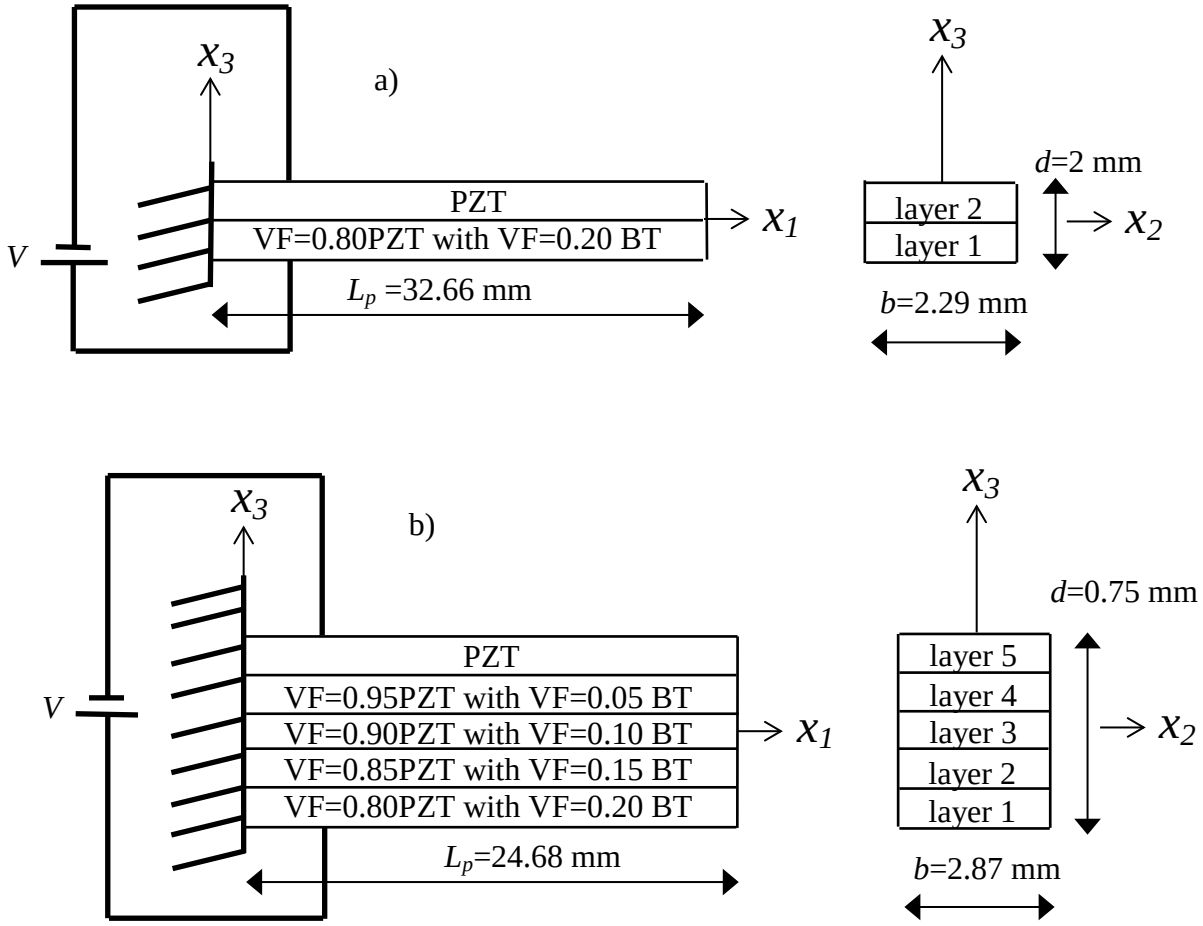

Figure 7.2 Sketch of the functionally graded piezoelectric bender with a) two layers and b) five layers of piezocomposites.

Table 7.1 Electro-mechanical material properties of polarized PZT-856

	PZT-856
Y_{11}^{E} [a] (GPa)	58
Y_{33}^{E} [b] (GPa)	45
G_{13}^{E} [c] (GPa)	12
ν_{12}^{E} [c]	0.30
ν_{31}^{E} [c]	0.33
d_{311} [a] (pm/V)	−260
d_{333} [a] (pm/V)	620
d_{113} [b] (pm/V)	710
κ_{11}/κ_0 [c, d]	3800
κ_{33}/κ_0 [a]	4100

[a] Alexander and Brei (2005).
[b] Manufacturer's data sheet from Giurgiutiu and Zagrai (2000).
[c] Assumed.
[d] $\kappa_0 = 8.85\times10^{-12}$ (F/m) denotes vacuum permittivity.

The BT has high dielectric constant, which enhances the conductibility of the 0-3 piezocomposites. Since Alexander and Brei (2005) did not report the mechanical properties of the BT, we further calibrate the properties from the experimental data of polarized 0-3 piezocomposites shown in Figure 7.3. Isotropic material symmetry and zero piezoelectric strain constant for BT are assumed due to the nature of non-polarized

barium titanate. Because no distinct phase for matrix was observed from the experiment, we choose BT as the matrix phase and PZT-856 as the particle phase (i.e., PZT-856/BT polarized 0-3 piezocomposite) to calibrate material properties. In Figure 7.3a, Young's modulus in the x_1-direction, 55 GPa, and Poisson's ratio, 0.35, of the BT matrix are calibrated by paralleling the trend line (dotted line) of the experimental data to particle-unit-cell prediction (solid line). Similarly, relative dielectric constant of the BT matrix is calibrated to 50000 shown in Figure 7.3b. It should be noted that the manufacturer supplied material data sheet reports Young's modulus in the x_1-direction of the PZT-856 particles is 58 GPa but the measurements from Alexander and Brei (2005) show 56.2-54.7 GPa. This discrepancy is observed in Figure 7.3a at PZT-856 particle VF=1. Figure 7.3c depicts the comparison of micromechanical predictions to the experimental data for the effective piezoelectric strain constant. Again, discrepancy between the data from data sheet and the measurements is observed at PZT-856 particle VF=1. The calibrated results of the BT matrix are listed in Table 7.2.

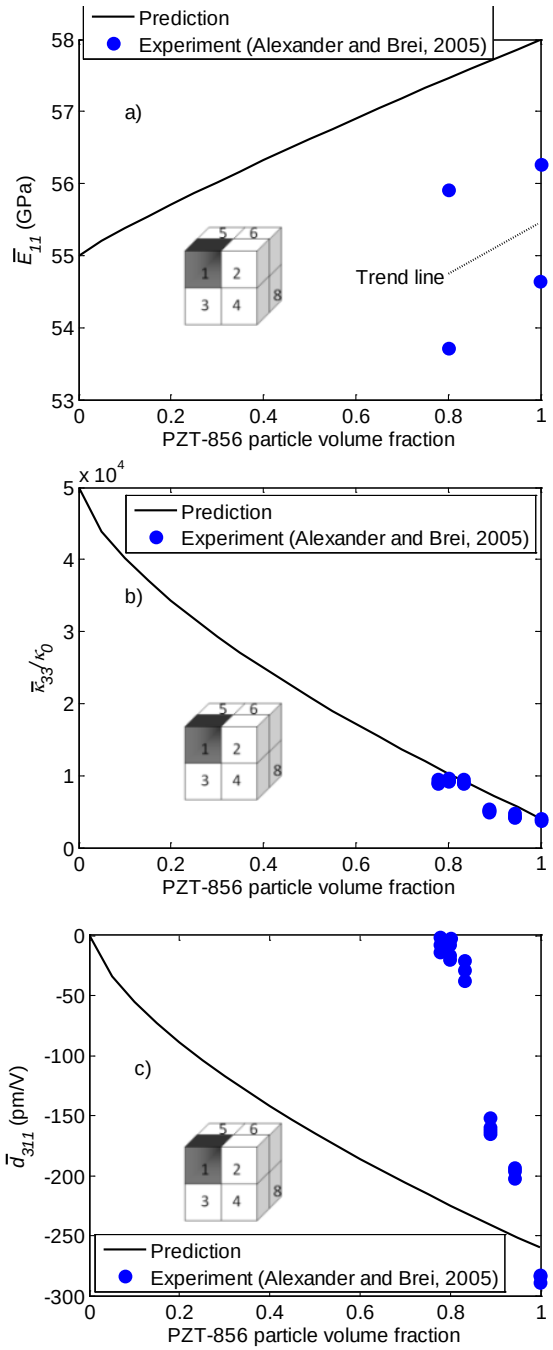

Figure 7.3 Comparison of micromechanical predictions to the experimental data (Alexander and Brei, 2005) for the effective a) relative dielectric constants $\bar{\kappa}_{33}/\kappa_0$, b) Young's modulus along the x_1-direction $\bar{E}_{11}$, c) and piezoelectric strain constant $\bar{d}_{311}$ for the PZT-856/BT polarized 0-3 piezocomposite as a function of polarized PZT-856 particle VF.

Table 7.2 Material properties of non-polarized barium titanate (calibrated from experimental data of Alexander and Brei, 2005)

	barium titanate
Young's modulus, Y (GPa)	55
Poisson's ratio, v	0.35
Relative dielectric constant	50000

Another combination of the polarized 0-3 piezocomposites is BT particles in a PZT-856 matrix (i.e., BT/PZT-856 polarized 0-3 piezocomposite). The material properties of the BT and PZT-856 phases used in the particle-unit-cell predictions use are listed in Table 7.1 and Table 7.2 which are calibrated in before. Comparisons between the experimental data and particle-unit-cell predictions on the effective properties of relative dielectric constants $\overline{\kappa}_{33}/\kappa_0$, Young's modulus along the x_1-direction $\overline{E}_{11}$, and piezoelectric strain constant $\overline{d}_{311}$ are shown in Figure 7.4. Although several discrepancies are observed, micromechanical estimations are able to qualitative capture the experimental measurements.

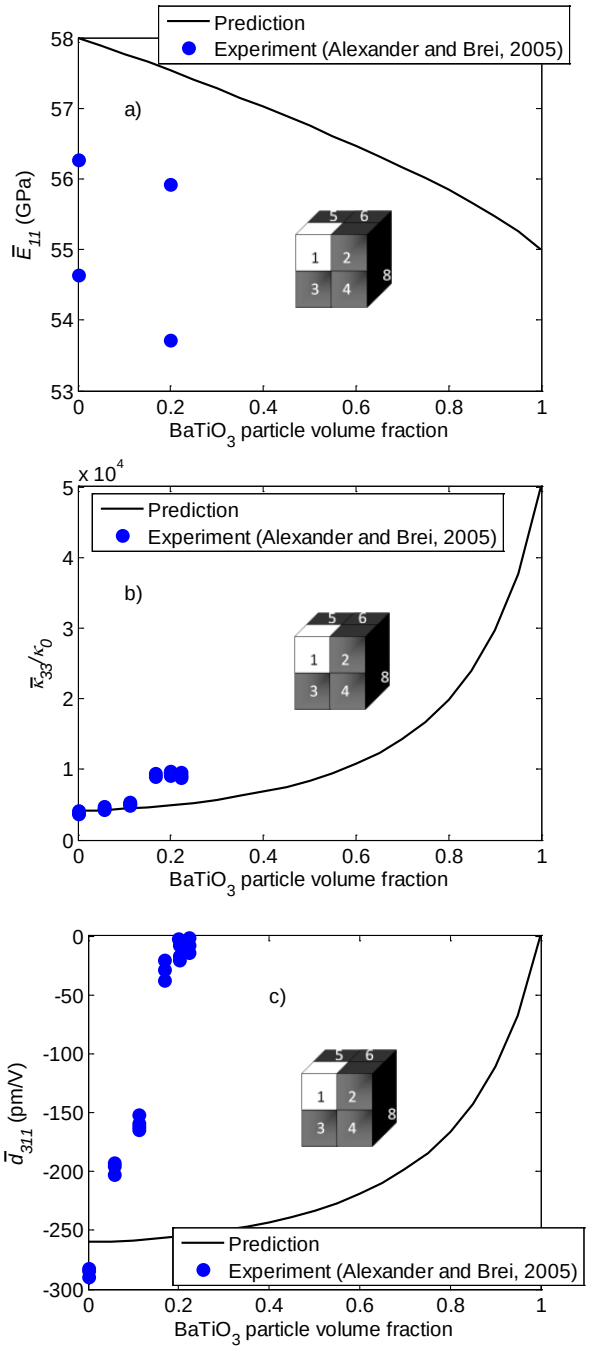

Figure 7.4 Comparison of micromechanical predictions to the experimental data (Alexander and Brei, 2005) for the effective a) relative dielectric constants $\bar{\kappa}_{33}/\kappa_0$, b) Young's modulus along the x_1-direction $\bar{E}_{11}$, c) and piezoelectric strain constant $\bar{d}_{311}$ for the BT/PZT-856 polarized 0-3 piezocomposite as a function of barium titanate particle VF.

Figure 7.5 and Figure 7.6 depicts the comparisons between predictions and experimental measurements on the tip deflection. It is obvious that the predictions from the PZT-856 particles in the barium titanate matrix (solid lines) are in good correlations with experimental results. The predictions of the piezocomposite with barium titanate particles in the PZT-856 matrix (dashed lines) underestimate the tip deflection. The polarized piezoelectric constitutive model used here is linear in nature, and therefore the estimations do not capture the natural hysteresis of the deflections.

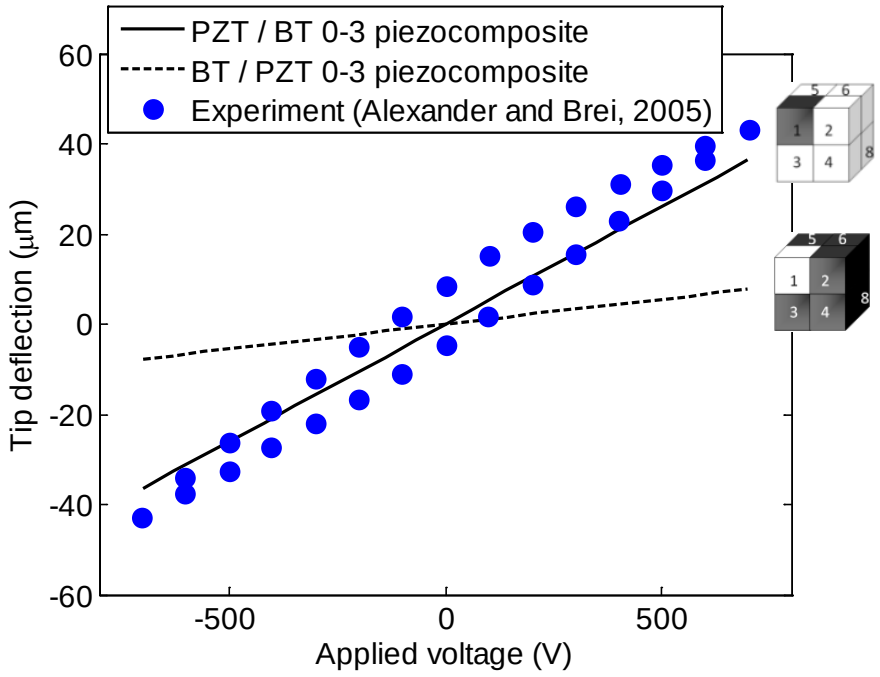

Figure 7.5 Relationships between a total applied voltage and the tip deflection of the two-layer functionally graded piezoelectric bender. The solid (PZT-856/BT 0-3 polarized piezocomposite) and dashed (BT/PZT-856 0-3 polarized piezocomposite) lines show the predictions from different compositions of the piezocomposite by particle-unit-cell model with laminate plate theory while solid circle symbols are experimental measurements from Alexander and Brei, 2005.

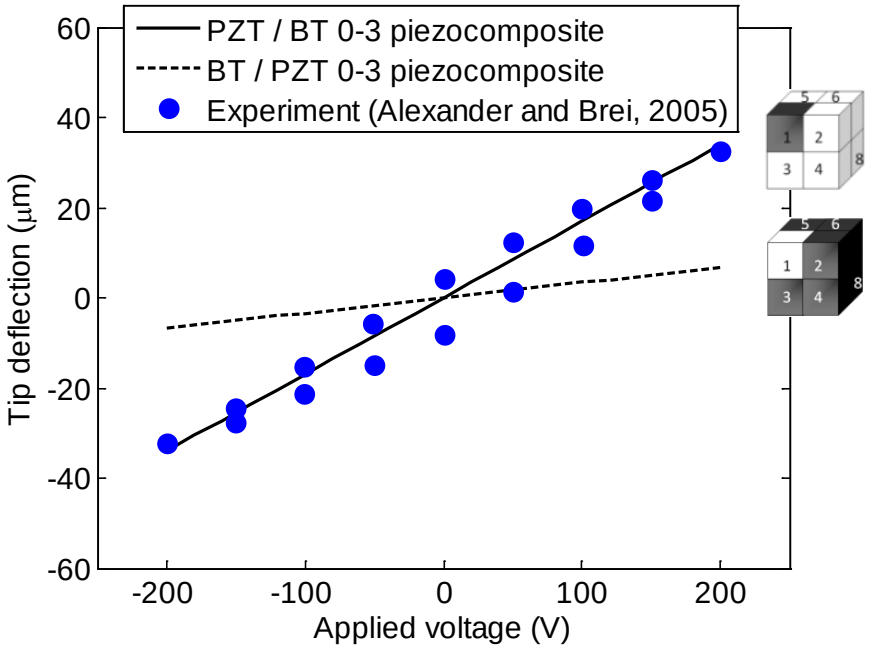

Figure 7.6 Relationships between a total applied voltage and the tip deflection of the five-layer functionally graded piezoelectric bender. The solid (PZT-856/BT 0-3 polarized piezocomposite) and dashed (BT/PZT-856 0-3 polarized piezocomposite) lines show the predictions from different compositions of the piezocomposite by particle-unit-cell model with laminate plate theory while solid circle symbols are experimental measurements from Alexander and Brei, 2005.

Another functionally graded piezoelectric beam was developed by Takagi et al. (2002), who made a graded compositional distribution of platinum (Pt) particles in polarized PZT matrices. The graded composition is achieved by bonding 0-3 piezocomposite layers with different platinum particle VF. Figure 7.7depicts layer configuration of functionally graded piezoelectric beam. The beam consists of seven polarized 0-3 piezocomposite layers with a center-symmetric composition profile, in which the compositions from the central layer to the surface layer are stepwise changed from VF=0.3 to 0 in an interval of VF=0.1 of the Pt particles. The central layer (i.e.,

VF=0.3 Pt particles) as an internal electrode is 200 μm thick, and other layers are 300 μm thick. The poling direction of each layer is toward the x_3-axis. The beam is coated with silver paste on the outer surfaces, which are perpendicular to the x_3-axis. The coated silver surfaces are connected to the same electrode against the internal electrode in the central layer. This design makes the layers above and below the central layer experienced opposite electric field when a voltage supplied by a DC power generator is applied. Thus, the beam bends along x_2-axis due to opposite deformation (extension and contraction) along the x_1-axis of the Pt/PZT polarized 0-3 piezocomposite layers.

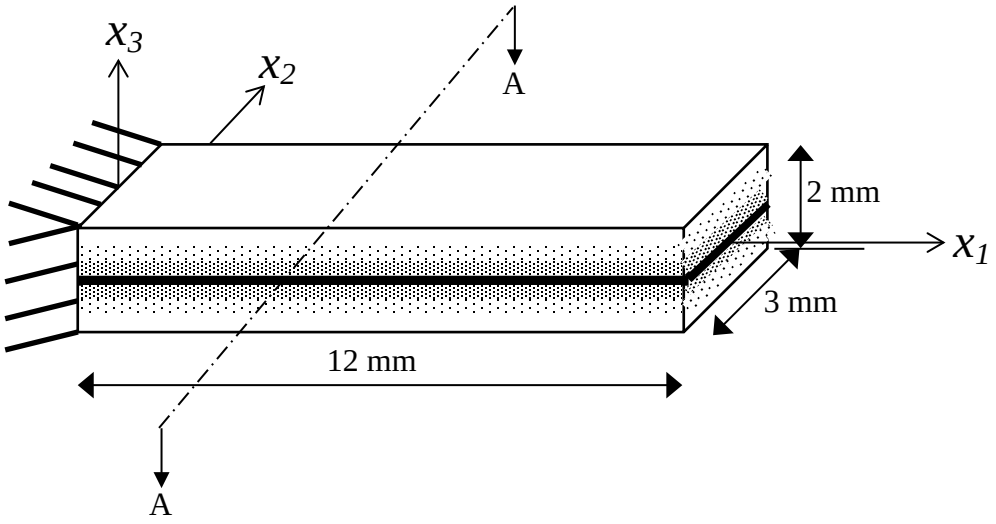

Figure 7.7 Sketch of the functionally graded piezoelectric bender.

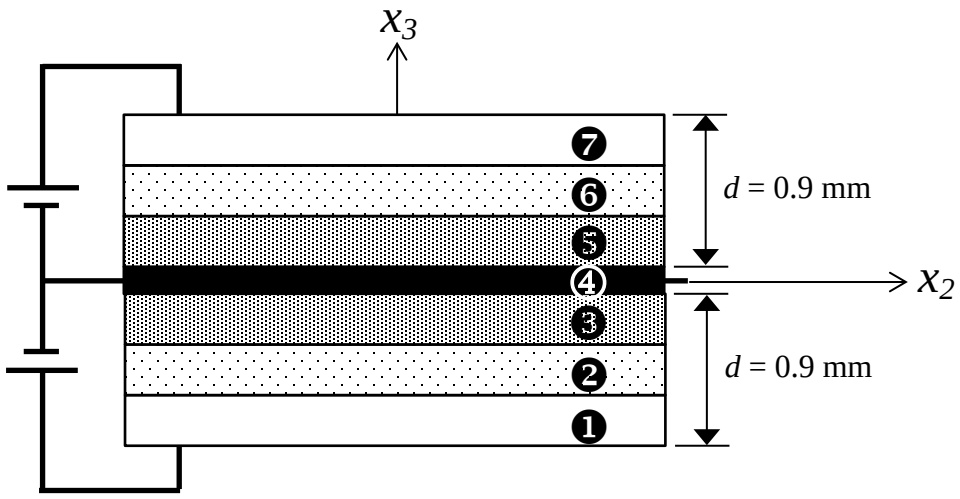

Figure 7.7 Continued.

In the example of Figure 7.7, the zero electric field across the layer 4 is specified due to electrical conductivity resulting from the spatial connection of Pt particles in the PZT matrix when Pt particle volume fraction reaches 0.3, which was reported by Takagi et al. (2002). The material properties of the PZT matrix were given by Takagi et al. (2002) which are listed in Table 7.3 and the properties of the Pt particles are referred to Davis (1998) which are listed in Table 7.4.

Table 7.3 Electro-mechanical material properties for the PZT matrix (Takagi et al., 2002)

	c_{1111} GPa	c_{1122} GPa	c_{1133} GPa	c_{3333} GPa	c_{2323} GPa	e_{311} C/m^2	e_{333} C/m^2	e_{113} C/m^2	$\frac{\kappa_{11}}{\kappa_0}$	$\frac{\kappa_{33}}{\kappa_0}$
PZT matrix	146	95.4	94.3	128	21.1[a]	−3.94	17.5	12.3[a]	1730[a]	1654

[a] Refer to properties of the PZT-5A from Morgan Electro Ceramics, Inc.

Table 7.4 Mechanical and electrical properties of the Pt particles (Davis, 1998)

	Platinum
Young's modulus, E (GPa)	171
Poisson's ratio, ν	0.39
Dielectric coefficient[a], $\kappa_{11} = \kappa_{22} = \kappa_{33}$ (nF/m)	89

[a] This dielectric coefficient which is ten thousand times of vacuum permittivity is assumed for comparison and simulation purpose because dielectric constants of conductive metals, in general, are considered as infinite.

Because this functionally graded piezoelectric beam has lower aspect ratio (i.e., 6), shear deflection could significantly contribute to the total deflection (i.e., sum of shear and bending deflection). It might violate the assumption of Euler-Bernoulli beam theory, zero shear deflection. Thus, we examine the percentage of error prediction due to

the shear deflection before we analyze this functionally graded piezoelectric beam whose aspect ratio is 6. Now, for a homogeneous and isotropic cantilever beam of rectangular cross section $b \times h$ (i.e., width ×height) with length l, loaded with an end load P we have

$$\delta_{\text{bending}} = \frac{Pl^3}{3EI}, \qquad \delta_{\text{shear}} = \frac{3Pl}{2AG},^{15} \tag{7.23}$$

where E, G, A, and I are Young's modulus, shear modulus, area of cross section, and area moment of inertia, respectively. We define the percentage of error prediction is

$$Error = \frac{\delta_{\text{shear}}}{\delta_{\text{bending}} + \delta_{\text{shear}}} \times 100. \tag{7.24}$$

Due to $A = bh$ and $I = bh^3/12$, Equation (7.24) can be rewritten to

$$Error = \frac{3E}{8G\left(l/h\right)^2 + 3E} \times 100. \tag{7.25}$$

Thus, for beams of any high aspect ratio (i.e., l / h), the percentage of error prediction is completely negligible. We consider two extreme cases, a cantilever beam made by PZT and another by Pt. The percentage of error prediction of the functionally graded piezoelectric beam should be between these two extreme cases. Figure 7.8 depicts the percentage of error prediction as a function of aspect ratio. For aspect ratio 6, the percentage of error predictions for PZT and Pt beams are under 4%. Hence, we believe that it is still feasible to use Euler-Bernoulli beam theory to analyze the functionally

[15] Derivation is referred to Den Hartog (1977)

graded piezoelectric beam which was experimentally examined by Takagi et al. (2002) shown in Figure 7.7.

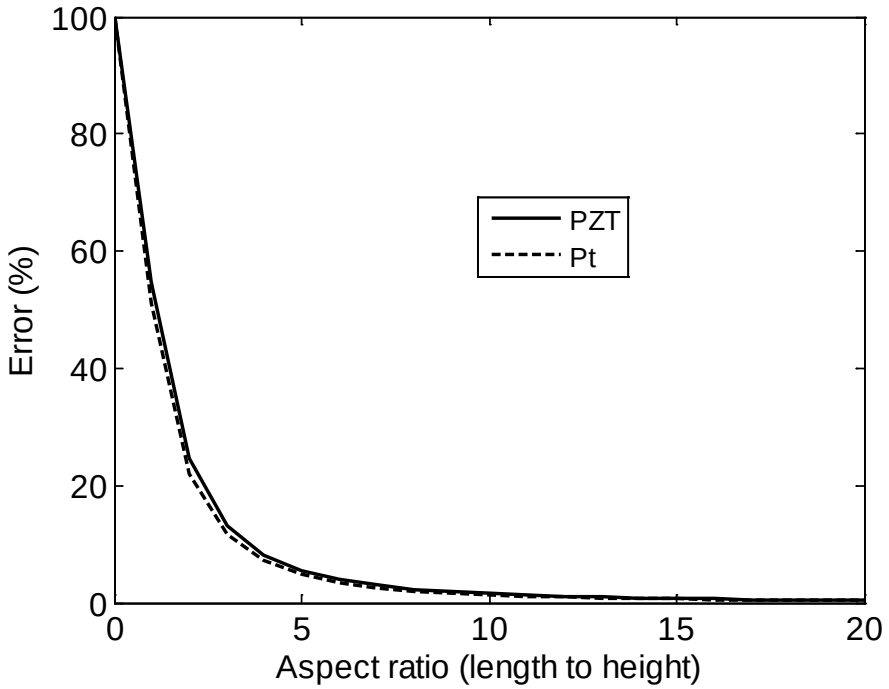

Figure 7.8 The percentage of error prediction vs. aspect ratio of the cantilever beam.

Figure 7.9 depicts the predictions and experimental observations (Takagi et al., 2002) of the curvature of the functionally graded piezoelectric beam against the total applied voltage. The dashed line considers the PZT matrix with linear electro-mechanical responses (i.e., omit the higher-order term in Equation (2.1)) while the solid

line considers nonlinear electro-mechanical responses of the PZT matrix. The nonlinear material parameters of the PZT matrix, $f_{3311} = f_{3322} = -1.95\times10^{-16}$, $f_{3333} = 4.5\times10^{-16}$, $f_{2223} = f_{1113} = 8.0\times10^{-16}$ m^2/V, and $\chi_{111} = \chi_{222} = \chi_{333} = 0$ F/V, are calibrated by using the experimental data at the total applied voltage $V_t = 500$ V shown in Figure 7.9. It is expected that when the total applied voltage is low (i.e., low electric field to be generated), say $V_t = 100$ V, both linear and nonlinear estimations give good agreements to the experimental measurement. As total applied voltage increasing, the linear prediction (dashed line) diverges from the experimental data gradually while the nonlinear estimation (solid line) is able to simulate the experimental data for the whole range of the total applied voltage. It is noted that each Pt/PZT polarized 0-3 piezocomposite layer except conductor layer (i.e., central layer) experiences a magnitude of 0.57 MV/m of the electric field at $V_t = 500$V. The magnitude 0.57 MV/m of the electric field is high enough to induce significant nonlinear response of PZT ceramics, which had been discussed in Section 1.2.1.

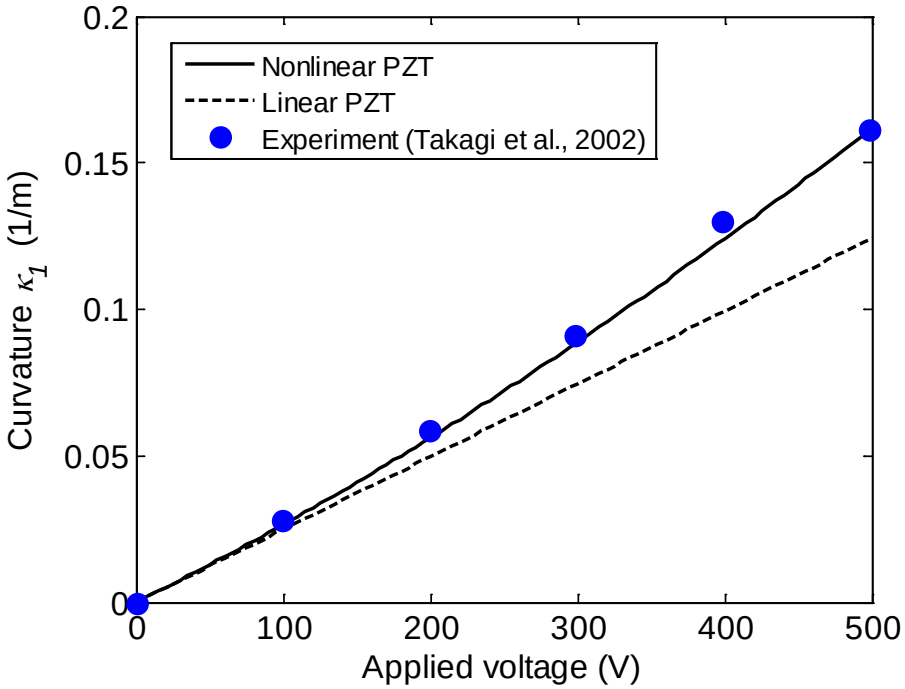

Figure 7.9 Relationships between a total applied voltage and the curvature of the functionally graded piezoelectric bender. The solid (Nonlinear PZT) and dashed (Linear PZT) lines show the predictions from particle-unit-cell model with laminate plate theory while solid circle symbols are experimental measurements of curvatures at specific applied voltages from Takagi et al., 2002.

CHAPTER VIII

CONCLUSIONS AND FUTURE RESEARCH

Conclusions of this study and potential future research are summarized in this chapter.

8.1 Conclusions

This study presents three micromechanical models, i.e., fiber-, particle-, and hybrid-unit-cell models, to study the effective electro-mechanical responses of 1-3, 0-3, and hybrid active composites, respectively. The constitutive models for each constituent in the active composites considered in this study are nonlinear polarized piezoelectric, time-dependent polarization switching, and linear viscoelastic constitutive models. Experimental data available in literature are first used to validate the micromechanical models, followed by parametric studies to examine the overall electro-mechanical responses of the active composites determined from the micromechanical models. In order to predict the effective nonlinear rate-dependent electromechanical responses, linearized micromechanical relations are first imposed in order to provide trial solutions at each instant of time. An iterative scheme, i.e., fixed-point method, is then added to minimize errors from linearizing the nonlinear electromechanical and time-dependent responses. For comparison purposes, Mori-Tanaka model is also reformulated to include the nonlinear polarized piezoelectric and linear viscoelastic constitutive models. Several analyses on understanding the nonlinear electromechanical responses of the active

composites using the proposed micromechanical models have been performed. The results are summarized as follow:

In Chapter IV, the effective responses of the polarized 1-3 active composites with nonlinear piezoelectric effect of the inhomogeneities are significantly different from the ones with linear polarized piezoelectric effects. This is due to the fact that the electromechanical responses in the polarized 1-3 active composites subject to an electric field input along the fiber direction are dominated by the fiber response. However, for the polarized 0-3 active composites with low conductivity of the matrix, the nonlinear responses are less pronounced since the overall responses are dominated by the matrix, which is modeled as linear elastic or viscoelastic, and only a small fraction of the applied electric field reaches the polarized piezoelectric particles. Reponses of the polarized 1-3 active composites under cyclic electric field inputs at different frequencies have also been studied. Inputs with lower frequency (slower loading rates) allow for the materials to undergo more pronounced creep deformation (or stress relaxation), which in this case is shown by the larger hysteretic loop in one cycle, lower amplitude of the corresponding stress output and smaller number of cycles to reach steady state. For the polarized 1-3 active composites the effective transverse responses are more sensitive to fiber cross section (circle vs. square) than the longitudinal responses while for the polarized 0-3 active composites the geometry of the reinforcements (sphere vs. cube) has significant influences on the effective responses. It has also been observed that the UC and MT predictions of the overall properties and responses of the polarized active composites are, in general, close to each other, with some mismatches observed. The comparison

between an original particle-reinforced active composite and a reversed-phase active composite, which is formed by viscoelastic particles dispersed in a polarized piezoelectric matrix, confirms that the matrix dominates the overall responses of a polarized 0-3 active composite.

In Chapter V, the effective hysteretic responses of the 1-3 active composites are significantly greater than those of the 0-3 active composites because the piezoelectric fibers dominate the overall longitudinal responses of the 1-3 active composites while the passive polymer matrix dominates the overall responses of the 0-3 active composites. The same phenomena are also observed in the polarized active composites, which had been discussed in Chapter IV. Higher concentrations of ferroelectric fibers cause stronger effective dielectric hysteresis and butterfly strain responses. The compressive stresses limit the amount of polarization to be generated from electric field inputs, as a result smaller hysteretic polarization and butterfly strain curves are observed in the 1-3 active composites. Also, a lower frequency input allows the 1-3 active composites to undergo more pronounced time-dependent response, which in this case is shown by broader hysteretic responses. The hysteretic response indicates amount of energy being dissipated, which is converted into heat. It is noted that many applications of active materials would involve cyclic electromechanical loading, thus the hysteretic response could eventually lead to cyclic failures. For the 0-3 active composites, improving the dielectric constant of inactive matrix efficiently enhances overall responses when the 0-3 active composites are subject to electric stimuli, which are often the case in actuator applications.

In Chapter VI, hybrid active composites are formed by adding ferroelectric fillers to the matrix, which significantly improves the blocked stress in the transverse fiber direction while insignificantly affects the overall electromechanical performance in the longitudinal fiber direction. This is because the matrix, whose properties change with adding the active fillers, dominates the transverse response. The free strains, however, significantly decrease in both transverse and longitudinal fiber directions as the amount of active fillers increases. This is due to the fact that adding stiffer active particles in a softer epoxy matrix results in a stiffer overall matrix. Thus, adding active fillers are useful for improving the blocked stress for active composites with 3-1 operating mode. Responses of the hybrid active composites under cyclic electric fields, with amplitude higher than the coercive electric field limit of the materials, and compressive stress loadings have been studied. Adding ferroelectric fillers slightly reduces the hysteretic polarization response, and significantly decreases the hysteretic strain response. As the matrix becomes stiffer, matrix would experience smaller deformations when an electric field input is applied, resulting in smaller residual stresses[16] in both fibers and matrix. Although its effect is minimum, the residual stress would affect the overall hysteretic polarization in the composites. As also expected, compressive stresses applied along the direction of electric field reduce the polarization capability of the composites. We also investigated the effect of frequencies on the overall electromechanical responses of the hybrid active composites. A lower frequency input allows the hybrid composites to

[16] The residual stress is defined as internal stresses in the constituents of the composites in absence of external mechanical stimuli. In this study, the residual stresses arise due to the mismatches in the properties and responses of the constituents when the composites are subjected to electric field input.

undergo more pronounced time-dependent response, which in this case is shown by broader hysteretic responses.

Finally, in Chapter VII, the developed particle-unit-cell model has been integrated to laminate plate theory, which forms a multi-scale model of a functionally graded piezoelectric bimorph actuator. The multi-scale model that considers the nonlinear polarized piezoelectric constitutive models is capable in capturing the bending deflection of the functionally graded actuator through applying electric voltages. In practical applications of actuators, it is desirable to utilize the greatest possible strain available in the actuators and it should be achieved by applying large electric fields, which lead to pronounced nonlinear responses.

8.2 Future Research

Two possible further researches are suggested as follow:

1) Multiscale modeling of active composite allows integrating micromechanical models with several types of elements within finite element (FE) analysis, which will be useful for analyzing more complex structures made of active composites. The multiscale analysis is very useful for designing smart devices (structures) having active composites.
2) Constitutive modeling of multifunctional composite materials with coupled multiple physical responses, e.g., mechanical, electrical, thermal, magnetic, and optical, can be realized by integrating different constitutive models into the developed micromechanical models. This extension is very useful for studying different responses of numerous multifunctional composites.

REFERENCES

Abate, J., and P. P. Valkó. 2004. "Multi-precision Laplace Transform Inversion," *Int. J. Numer. Meth. Eng.*, 60(5):979-993.

Aboudi, J. 1991. *Mechanics of Composite Materials*. Elsevier, Amsterdam, Netherlands.

Aboudi, J, 1998. "Micromechanical Prediction of the Effective Coefficients of Thermo-piezoelectric Multiphase Composites," *J. Intel. Mat. Syst. Str.*, 9(9):713-722.

Aboudi, J, 2005. "Hysteresis Behavior of Ferroelectric Fiber Composites," *Smart Mater. Struct.*, 14(4):715-726.

Aldraihem, O. J., A. Baz, and T. S. Al-Saud. 2007. "Hybrid Composites with Shunted Piezoelectric Particles for Vibration Damping," *Mech. Adv. Mater. Struct.*, 14(6):413-426.

Aldraihem, O. J. 2011. "Micromechanics Modeling of Viscoelastic Properties of Hybrid Composites with Shunted and Arbitrarily Oriented Piezoelectric Inclusions," *Mech. Mater.*, 43(11):740-753.

Alexander, P. W., and D. Brei. 2005. "The Fabrication and Material Characterization of PZT Based Functionally Graded Piezoceramics," *Proceedings of SPIE-The International Society for Optical Engineering*, 5764:57-70.

Anderson, E. H. 1989. *Piezoceramic induced strain actuation of one- and two-dimensional structures.* M.S. thesis, Massachusetts Institute of Technology, Cambridge, Massachusetts.

Arafa, M., and A. Baz. 2000. "Dynamics of Active Piezoelectric Damping Composites," *Compos. Part B-Eng.*, 31(4):255-264.

Asare, T. A., J. P. Schultz, B. D. Poquette, A. O. Aning, and S. L. Kampe. 2005. "Dynamic Mechanical Analysis of Metal-Particulate Ferroelectric Ceramic Composites; Copper-Barium Titanate (Cu-$BaTiO_3$) System," *Proceedings of Symposium Sponsored by Materials, Science & Technology 2005 (MS & T'05),* Pittsburgh, Pennsylvania, pp. 189-194.

Asi, O. 2009. "Mechanical Properties of Glass-Fiber Reinforced Epoxy Composites Filled with Al_2O_3 Particles," *J. Reinf. Plast. Comp.*, 28(23):2861-2867.

Asi, O. 2010. "An Experimental Study on the Bearing Strength Behavior of Al_2O_3 Particle Filled Glass Fiber Reinforced Epoxy Composites Pinned Joints," *Compos. Struct.*, 92(2):354-363.

Ballas, R. G. 2007. *Piezoelectric Multilayer Beam Bending Actuators Static and Dynamic Behavior and Aspects of Sensor Integration.* Springer, New York.

Banno, H. 1983. "Recent Developments of Piezoelectric Ceramic Products and Composites of Synthetic Rubber and Piezoelectric Ceramic Particles," *Ferroelectrics*, 50(1):3-12.

Bassiouny, E., A. F. Ghaleb, and G. A. Maugin. 1988. "Thermodynamical Formulation for Coupled Electromechanical Hysteresis Effects—I. Basic Equations," *Int. J. Eng. Sci.*, 26(12):1279-1295.

Bent, A. A., and N. W. Hagood. 1997. "Piezoelectric Fiber Composites with Interdigitated Electrodes," *J. Intel. Mat. Syst. Str.*, 8(11):903-919.

Bent, A. A., N. W. Hagood, and J. P. Rodgers. 1995. "Anisotropic Actuation with Piezoelectric Fiber Composites," *J. Intel. Mat. Syst. Str.*, 6(3):338-349.

Benvensite, Y. 1987. "A New Approach to the Application of Mori-Tanaka's Theory in Composite Materials," *Mech. Mater.*, 6(2):147-157.

Burcsu, E., G. Ravichandran, and K. Bhattacharya. 2004. "Large Electrostrictive Actuation of Barium Titanate Single Crystals," *J. Mech. Phys. Solids*, 52(4):823-846.

Cao, H., and A. G. Evans. 1993. "Nonlinear Deformation of Ferroelectric Ceramics," *J. Am. Ceram. Soc.*, 73(4):890-896.

Chan, H. L. W., and J. Unsworth. 1989. "Simple Model for Piezoelectric Ceramic/Polymer 1-3 Composites Used in Ultrasonic Transducer Applications," *IEEE. Tran. Ultrason., Ferroelectr. Freq. Control*, 36(4):434-441.

Chen, W., and C. S. Lynch. 1998. "A Micro-electro-mechanical Model for Polarization Switching of Ferroelectric Materials," *Acta Mater.*, 46(15):5303-5311.

Cho, J., J.Y. Chen, and I.M. Daniel. 2007. "Mechanical Enhancement of Carbon Fiber/epoxy Composites by Graphite Nanoplatelet Reinforcement," *Scripta Mater.*, 56(8):685-688.

Christensen, R. M. 1982. *Theory of Viscoelasticity*. Academic Press, New York.

Crawley, E. F., and E. H. Anderson. 1990. "Detailed Models of Piezoelectric Actuation of Beams," *J. Intel. Mat. Syst. Str.*, 1(1):4-25.

Dausch, D. E. 1997. "Ferroelectric Polarization Fatigue in PZT-Based RAINBOWs and Bulk Ceramics," *J. Am. Ceram. Soc.*, 80(9):2355-2360.

Davis, J. R. 1998. *Metals Handbook*. ASM International, pp. 626.

Den Hartog, J. P. 1977. *Strength of Materials*. Dover, New York, pp. 108.

Dunn, M. L., and M. Taya. 1993a. "Micromechanics Predictions of the Effective Electroelastic Moduli of Piezoelectric Composites," *Int. J. Solids Struct.*, 30(2):161-175.

Dunn, M. L., and M. Taya. 1993b. "An Analysis of Piezoelectric Composite Materials Containing Ellipsoidal Inhomogeneities," *P. Roy. Soc. Lond. A Mat.*, 443(1918):265-287.

Dvorak, G. J., and M. V. Srinivas. 1999. "New Estimates of Overall Properties of Heteroheneous Solids," *J. Mech. Phys. Solids*, 47(4):899-920.

Fang, D., and C. Li. 1999. "Nonlinear Electric-mechanical Behavior of a Soft PZT-51 Ferroelectric Ceramic," J. Mater. Sci., 34(16):4001-4010.

Ferry, J. D. 1970. *Viscoelastic Properties of Polymers*. John Wiley & Sons, New York.

Fett, T., and G. Thun. 1998. "Determination of Room-temperature Tensile Creep of PZT," *J. Mater. Sci. Lett.*, 17(22):1929-1931.

Furukawa, T., K. Fujino, and E. Fukada. 1976. "Electromechanical Properties in the Composites of Epoxy Resin and PZT Ceramics," *Jap. J. Appl. Phys.*, 15(11):2119-2129.

Gadkaree, K. P. 1992. "Particulate-fibre-reinforced Glass Matrix Hybrid Composite," *J. Mater. Sci.*, 27(14):3827-3834.

Giurgiutiu, V., and A. N. Zagrai. 2000. "Characterization of Piezoelectric Wafer Active Sensors," *J. Intel. Mat. Syst. Str.*, 11(12):959-976.

Hagood, N. W., and A. A. Bent. 1993. "Development of Piezoelectric Fiber Composites for Structural Actuation," In: Proc 34th AIAA Structures, Structural Dynamics, and Materials Conference, April 19-22, La Jolla, CA, AIAA paper no. 93-1717:3625-3638.

Hall, D. A. 2001. "Review Nonlinearity in Piezoelectric Ceramics," *J. Mater. Sci.*, 36(19):4575-4601.

Hori, M., T. Aoki, Y. Ohira, and S. Yano. 2001. "New Type of Mechanical Damping Composites Composed of Piezoelectric Ceramics, Carbon Black and Epoxy Resin," *Compos. Part A-Appl. S.*, 32(2):287-290.

Huber, J.E. 2005. "Micromechanical Modelling of Ferroelectrics," *Curr. Opin. Solid State Mater. Sci.*, 9(3):100-106.

Huber, J.E., N.A. Fleck, C.M. Landis, and R.M. McMeeking. 1999. “A Constitutive Model for Ferroelectric Polycrystals,” *J. Mech. Phys. Solids,* 47(8):1663-1697.

Hussain, M., A. Nakahira, and K. Niihara. 1996. “Mechanical Property Improvement of Carbon Fiber Reinforced Epoxy Composites by Al_2O_3 Filler Dispersion,” *Mater. Lett.*, 26(3):185-191.

Hussain, M., A. Nakahira, S. Nishijima, and K. Niihara. 2000. “Evaluation of Mechanical Behavior of CFRC transverse to the Fiber Direction at Room and Cryogenic Temperature,” *Compos. Part A-Appl. S.*, 31(2):173-179.

Hwang, S. C., C. S. Lynch, and R. M. McMeeking. 1995. “Ferroelectric/ferroelastic Interactions and a Polarization Switching Model,” *Acta Metall. Mater.*, 43(5):2073-2084.

Hwang, H. J., K. Watari, M. Sando, and M. Toriyama. 1997. “Low-temperature Sintering and High-strength $Pb(Zr,Ti)O_3$-matrix Composites Incorporating Silver Particles,” *J. Am. Ceram. Soc.*, 80(3):791-793.

Institute of Electrical and Electronics Engineers. 1987. *IEEE Standard on Piezoelectricity.* IEEE, Inc., New York.

Jayabal, K., D. Srikrishna, T.S. Abhinandan, A. Arockiarajan, and S.M. Srinivasan. 2009. “A Thermodynamically Consistent Model with Evolving Domain Structures in Ferroelectrics,” *Int. J. Eng. Sci.*, 47(10):1014-1024.

Jayendiran, R., and A. Arockiarajan. 2012. “Modeling of Dielectric and Piezoelectric Response of 1-3 Type Piezocomposites,” *J. Appl. Phys.*, 112(4):044107.

Jayendiran, R., and A. Arockiarajan. 2013. “Non-linear Electromechanical Response of 1–3 Type Piezocomposites,” *Int. J. Solids Struct.*, 50(14-15):2259–2270.

Jiang, B., and R.C. Batra. 2001. “Effective Electroelastic Properties of a Piezocomposite with Viscoelastic and Dielectric Relaxing Matrix,” *J. Intel. Mat. Syst. Str.*, 12(12):847-866.

Jiang, Q., E. C. Subbarao, and L. E. Cross. 1994. “Grain Size Dependence of Electric Fatigue Behavior of Hot Pressed PLZT Ferroelectric Ceramics,” *Acta Metall. Mater.*, 42(11):3687–3694.

Kamlah, M. 2001. “Ferroelectric and Ferroelectric Piezoelectrics – Modeling of Electromechanical Hysteresis Phenomena,” *Continuum Mech. Therm.*, 13(4):219-268.

Kar-Gupta, R., and T.A. Venkatesh. 2007. “Electromechanical Response of 1–3 Piezoelectric Composites: An Analytical Model,” *Acta Mater.*, 55(3):1093–1108.

Landis, C. M. 2004. “Non-linear Constitutive Modeling of Ferroelectrics,” *Curr. Opin. Solid State Mater. Sci.*, 8(1):59-69.

Laws, N., and R. McLaughlin. 1978. “Self-consistent Estimates for the Viscoelastic Creep Compliances of Composite Materials,” *P. Roy. Soc. Lond. A Mat.*, 359(1697):251-273.

Le Moal, P., and D. Perreux. 1993. “Evaluation of Creep Compliances of Unidirectional Fiber-reinforced Composites,” *Compos. Sci. Technol.*, 51(4):469-477.

Li, J.Y., and M. L. Dunn. 2001a. “Viscoelectroelastic Behavior of Heterogeneous Piezoelectric Solids,” *J. Appl. Phys.*, 89(5):2893-2903.

Li, J. Y., and M. L. Dunn. 2001b. “Variational Bounds for the Effective Moduli of Heterogeneous Piezoelectric Solids,” *Philos. Mag. A*, 81(4):903-926.

Li, K., X.-L, Gao, and A. K. Roy. 2006. “Micromechanical Modeling of Viscoelastic Properties of Carbon Nanotube-Reinforced Polymer Composites,” *Mech. Adv. Mater. Struct.*, 13(4):317-328.

Li, J.-F., K. Takagi, N. Terakubo, and R. Watanabe. 2001. “Electrical and Mechanical Properties of Piezoelectric Ceramic/metal Composites in the $Pb(Zr,Ti)O_3$/Pt System,” *Appl. Phys. Lett.*, 79(15):2441-2443.

Lines, M. E., and A. M. Glass. 1977. *Principles and Applications of Ferroelectrics and Related Materials*, Oxford University Press, Oxford, England.

Lou, X. J. 2009. “Polarization Fatigue in Ferroelectric Thin Films and Related Materials,” *J. Appl. Phys.*, 105:024101.

Lu, W., D.-N. Fang, C. Q. Li, and K.-C. Hwang. 1999. “Nonlinear Electric–mechanical Behavior and Micromechanics Modelling of Ferroelectric Domain Evolution,” *Acta Mater.*, 47(10):2913-2926.

Ma, B., S. Tong, M. Narayanan, S. Liu, S. Chao, and U. Balachandran. 2011. “Fabrication and Dielectric Property of Ferroelectric PLZT Films Grown on Metal Foils,” *Mater. Res. Bull.*, 46(7):1124-1129.

Mori, T., and K. Tanaka. 1973. “Average Stress in Matrix and Average Elastic Energy of Materials with Misfitting Inclusions,” *Acta Metall.*, 21(5):571-574.

Muliana., A. 2010. “A Micromechanical Formulation for Piezoelectric Fiber Composites with Nonlinear and Viscoelastic Constituents,” *Acta Mater.*, 58(9):3332-3344.

Muliana., A. 2011. “Time Dependent Behavior of Ferroelectric Materials undergoing changes in Their Material properties with Electric Field and Temperature,” *Int. J. Solids Struct.*, 48(19):2718-2731.

Muliana, A., and K.-A. Li. 2010. “Time-dependent Response of Active Composites with Thermo, Electrical, and Mechanical Coupling Effect,” *Int. J. Eng. Sci.*, 48(11):1481-1497.

Muliana, A., and C.-H. Lin. 2011. “A Multi-scale Formulation for Predicting Non-linear Thermo-electro-mechanical Response in Heterogeneous Bodies,” *J. Intel. Mat. Syst. Str.*, 22(8):723-738.

Munro R. G. 1997. “Evaluated Material Properties for a Sintered α-Alumina,” *J. Am. Ceram. Soc.*, 80(8):1919-1928.

Nan, C.-W. 1994. “Effective-medium Theory of Piezoelectric Composites,” *J. Appl. Phys.*, 76(2):1155-1163.

Nan, C.-W., and F.-S. Jin. 1993. “Multiple-scattering Approach to Effective Properties of Piezoelectric Composites,” *Phys. Rev. B*, 48(12):8578-8582.

Nelson, L. J., C. R. Bowen, R. Stevens, M. Cain, and M. Stewart. 2003, “High Field Behaviour of Piezoelectric Fibre Composites” *Proceedings of SPIE Smart Materials and Structures*, 5053:544-555.

Newnham, R.E., D.P. Skinner, and L.E. Cross 1978. “Connectivity and Piezoelectric-pyroelectric Composites,” *Mater. Res. Bull.*, 13(5):525-536.

Odegard, G. M. 2004. “Constitutive Modeling of Piezoelectric Polymer Composites,” *Acta Mater.*, 52(18):5315-5330.

Panteny, S., C. R. Bowen, and R. Stevens. 2006. “Characterisation of Barium Titanate-silver Composites, Part I: Microstructure and Mechanical properties,” *J. Mater. Sci.*, 41(12):3837-3843.

Park, S.-E., V. Vedula, M.-J. Pan, W. S. Hackenberger, P. Pertsch, and T. R. Shrout. 1998. “Relaxor Based Ferroelectric Single Crystals for Electromechanical Actuators,” *Proceedings of SPIE the International Society for Optical Engineering*, 3324:136-144.

Poquette, B. D., J. P. Schultz, T. A. Asare, A. O. Aning, and S. L. Kampe. 2005. “Ferroelectric Reinforced Metal Matrix Composites for Damping Applications,”

Proceedings of Symposium Sponsored by Materials, Science & Technology 2005 (MS & T'05), Pittsburgh, Pennsylvania, pp. 119-126.

Rajagopal, K.R., and A.S. Wineman. 2008. "A Quasi-correspondence Principle for Quasi-linear Viscoelastic Solids," *Mech. Time-depend. Mater.*, 12(1):1-14.

Safari, A. 1994. "Development of Piezoelectric Composites for Transducers," *J. Phys. III France*, 4(7):1129-1149.

Schapery, R. A. 1974. *Mechanics of Composite Materials*. Vol. 2, ed. G. P. Sendeckyj Academic Press, New York, pp. 119.

Shieh, J., J. H. Yeh, Y. C. Shu, and J. H. Yen. 2007. "Operation of Multiple 90° Switching Systems in Barium Titanate Single Crystals under Electromechanical Loading," *Appl. Phys. Lett.*, 91(6):062901.

Smith, W. A. 1986. "Composite Piezoelectric Materials for Medical Ultrasonic Imaging Transducers — A Review," *Proceedings of IEEE ISAF*, pp. 249-256.

Smith, W. A., and B. A. Auld. 1991. "Modeling 1-3 Composite Piezoelectrics: Thickness-mode Oscillations," *IEEE T. Ultrason. Ferr.*, 38(1):40-47.

Sohrabi, A., and A. Muliana. 2013. "Rate-dependent Electro-mechanical Coupling Response of Ferroelectric Materials: A Finite Element Formulation," *Mech. Mater.*, 62(1):44-59.

Subramaniyan, A. K., and C.T. Sun. 2006. "Enhancing Compressive Strength of Unidirectional Polymeric Composites Using Nanoclay," *Compos. Part A-Appl. S.*, 37(12):2257-2268.

Swallow, L. M., J. K. Luo, E. Siores, I. Patel, and D. Dodds. 2008. "A Piezoelectric Fibre Composite Based Energy Harvesting Device for Potential Wearable Applications," *Smart Mater. Struct.*, 17(2):025017.

Takagi, K., J.-F. Li, S. Yokoyama, and R. Watanabe. 2003. "Fabrication and Evaluation of PZT/Pt Piezoelectric Composites and Functionally Graded Actuators," *J. Eur. Ceram. Soc.*, 23(10):1577-1583.

Takagi, K., J.-F. Li, S. Yokoyama, R. Watanabe, A. Almajid, and Minoru Taya. 2002. "Design and Fabrication of Functionally Graded PZT/Pt Piezoelectric Bimorph Actuator," *Sci. Technol. Adv. Mater.*, 3(2):217-224.

Tan, P., and L. Tong. 2001. “Micromechanics Models for Non-linear Behavior of Piezo-electric Fiber Reinforced Composite Materials,” *Int. J. Solids Struct.*, 38(50-51):8999-9032.

Taylor, R. L., K. S. Pister, and G. L. Goudreau. 1970. “Thermomechanical Analysis of Viscoelastic Solids,” *Int. J. Numer. Meth. Eng.*, 2(1):45-59.

Tiersten, H. F. 1993. “Electroelastic Equations for Electroded Thin Plates Subject to Large Driving Voltages,” *J. Appl. Phys.*, 74(5):3389-3393.

Tsai, J.-L., and M.-D. Wu. 2007. “Organoclay Effect on Mechanical Responses of Glass/Epoxy Nanocomposites,” *J. Compos. Mater.*, 41(20):2513-2528.

Uddin, M. F., and C.T. Sun. 2008. “Strength of Unidirectional Glass/epoxy Composite with Silica Nanoparticle-enhanced Matrix,” *Compos. Sci. Technol.*, 68(7-8):1637-1643.

Vlasveld, D.P.N., H.E.N. Bersee, and S.J. Picken. 2005. “Nanocomposite Matrix for Increased Fibre Composite Strength,” *Polymer*, 46(23):10269-10278.

Wang, S., S. Adanur, and Z. Jang. 1997. “Mechanical and Thermo-mechanical Failure Mechanism Analysis of Fiber/Filler Reinforced Phenolic Matrix Composites,” *Compos. Part B-Eng.*, 28(3):215-231.

Wang, D., Y. Fotinich, and G. P. Carman. 1998. “Influence of Temperature on the Electromechanical and Fatigue Behavior of Piezoelectric Ceramics,” *J. Appl. Phys.*, 83(10):5342.

Weng, G.J. 1984. “Some Elastic Properties of Reinforced Soilds, with Special Reference to Isotropic Ones Containing Spherical Inclusion,” *Int. J. Eng. Sci.*, 22(7):845-856.

Wu, C. C. M., M. Kahn, and W. Moy. 1996. “Piezoelectric Ceramics with Functional Gradients: A New Application in Material Design,” *J. Am. Ceram. Soc.*, 79(3):809-812.

Yancey, R. N., and M.-J. Pindera. 1990. “Micromechanical Analysis of the Creep Response of Unidirectional Composites,” *J. Eng. Mater.-T. ASME*, 112(2):157-163.

Zeng, R., K. W. Kwok, H. L. W. Chan, and C. L. Choy. 2002. “Longitudinal and Transverse Piezoelectric Coefficients of Lead Zirconate Titanate/vinylidene Fluoride-trifluoroethylene Composites with Different Polarization States.” *J. Appl. Phys.*, 92(5):2674-2679.

Zhang, N., L. Li, and Z. Gui. 2001. “Degradation of Piezoelectric and Dielectric Relaxation Properties due to Electric Fatigue in PLZT Ferroelectric Capacitors,” *Mater. Lett.*, 48(1):39-43.

Zhang, H. L., J.-F. Li, and B.-P. Zhang. 2006. “Fabrication and Evaluation of PZT/Ag Composites and Functionally Graded Piezoelectric Actuators,” *J. Electroceram.*, 16(4):413-417.

Zheng, Y., R. Ning, and Y. Zheng. 2005. “Study of SiO_2 Nanoparticles on the Improved Performance of Epoxy and Fiber Composites,” *J. Reinf. Plast. Comp.*, 24(3):223-233.

Zhou, X., and A. Chattopadhyay. 2000. “Hysteresis Behavior and Modeling of Piezoceramic Actuators,” *Proceeding of SPIE Smart Structure and Material*, 3985:640.

Zhou, X., and A. Chattopadhyay. 2001. “Hysteresis Behavior and Modeling of Piezoceramic Actuators,” *J. Appl. Mech.*, 68(2):270-277.

Zhou, D., and M. Kamlah. 2005. “Determination of Room-temperature Creep of Soft Lead Zirconate Titanate Piezoceramics under Static Electric Fields,” *J. Appl. Phys.*, 98:104107.

Zhou, D., and M. Kamlah. 2006. “Room-temperature Creep of Soft PZT under Static Electrical and Compressive Stress Loading,” *Acta Mater.*, 54(5):1389-1396.

APPENDIX A

The micromechanical relations of the fiber-unit-cell model, shown in Figure 3.1, are formed by imposing the traction and electric flux continuity and displacement and potential compatibility conditions within all subcells and the perfect bonding condition at the subcells' interfaces. The linearized micromechanical relations for piezocomposite comprising unidirectional fibers with poling direction aligned in the x_3 direction are summarized as follows. The displacement compatibility conditions give:

$$\frac{V^{(1)}}{V^{(1)}+V^{(2)}}\varepsilon_{11}^{(1)}+\frac{V^{(2)}}{V^{(1)}+V^{(2)}}\varepsilon_{11}^{(2)}=\overline{\varepsilon_{11}}, \tag{A.1}$$

$$\frac{V^{(3)}}{V^{(3)}+V^{(4)}}\varepsilon_{11}^{(3)}+\frac{V^{(4)}}{V^{(3)}+V^{(4)}}\varepsilon_{11}^{(4)}=\overline{\varepsilon_{11}}, \tag{A.2}$$

$$\frac{V^{(1)}}{V^{(1)}+V^{(3)}}\varepsilon_{22}^{(1)}+\frac{V^{(3)}}{V^{(1)}+V^{(3)}}\varepsilon_{22}^{(3)}=\overline{\varepsilon_{22}}, \tag{A.3}$$

$$\frac{V^{(2)}}{V^{(2)}+V^{(4)}}\varepsilon_{22}^{(2)}+\frac{V^{(4)}}{V^{(2)}+V^{(4)}}\varepsilon_{22}^{(4)}=\overline{\varepsilon_{22}}, \tag{A.4}$$

$$\varepsilon_{33}^{(1)}=\overline{\varepsilon_{33}}, \tag{A.5}$$

$$\varepsilon_{33}^{(2)}=\overline{\varepsilon_{33}}, \tag{A.6}$$

$$\varepsilon_{33}^{(3)}=\overline{\varepsilon_{33}}, \tag{A.7}$$

$$\varepsilon_{33}^{(4)}=\overline{\varepsilon_{33}}, \tag{A.8}$$

$$\frac{V^{(1)}}{V^{(1)}+V^{(3)}}\varepsilon_{23}^{(1)}+\frac{V^{(3)}}{V^{(1)}+V^{(3)}}\varepsilon_{23}^{(3)}=\overline{\varepsilon_{23}}, \tag{A.9}$$

$$\frac{V^{(2)}}{V^{(2)}+V^{(4)}}\varepsilon_{23}^{(2)}+\frac{V^{(4)}}{V^{(2)}+V^{(4)}}\varepsilon_{23}^{(4)}=\overline{\varepsilon_{23}}, \tag{A.10}$$

$$\frac{V^{(1)}}{V^{(1)}+V^{(2)}}\varepsilon_{13}^{(1)}+\frac{V^{(2)}}{V^{(1)}+V^{(2)}}\varepsilon_{13}^{(2)}=\overline{\varepsilon_{13}}, \tag{A.11}$$

$$\frac{V^{(3)}}{V^{(3)}+V^{(4)}}\varepsilon_{13}^{(3)}+\frac{V^{(4)}}{V^{(3)}+V^{(4)}}\varepsilon_{13}^{(4)}=\overline{\varepsilon_{13}}, \tag{A.12}$$

$$V^{(1)}\varepsilon_{12}^{(1)}+V^{(2)}\varepsilon_{12}^{(2)}+V^{(3)}\varepsilon_{12}^{(3)}+V^{(4)}\varepsilon_{12}^{(4)}=\overline{\varepsilon_{12}}. \tag{A.13}$$

The traction continuity conditions yield to:

$$\sigma_{11}^{(1)}-\sigma_{11}^{(2)}=0, \tag{A.14}$$

$$\sigma_{11}^{(3)}-\sigma_{11}^{(4)}=0, \tag{A.15}$$

$$\sigma_{22}^{(1)}-\sigma_{22}^{(3)}=0, \tag{A.16}$$

$$\sigma_{22}^{(2)}-\sigma_{22}^{(4)}=0, \tag{A.17}$$

$$\sigma_{23}^{(1)}-\sigma_{23}^{(3)}=0, \tag{A.18}$$

$$\sigma_{23}^{(2)}-\sigma_{23}^{(4)}=0, \tag{A.19}$$

$$\sigma_{13}^{(1)}-\sigma_{13}^{(2)}=0, \tag{A.20}$$

$$\sigma_{13}^{(3)}-\sigma_{13}^{(4)}=0, \tag{A.21}$$

$$\sigma_{12}^{(1)}-\sigma_{12}^{(2)}=0, \tag{A.22}$$

$$\sigma_{12}^{(1)}-\sigma_{12}^{(3)}=0, \tag{A.23}$$

$$\sigma_{12}^{(1)} - \sigma_{12}^{(4)} = 0. \tag{A.24}$$

The micromechanical relations for the potential compatibility conditions are:

$$\frac{V^{(1)}}{V^{(1)}+V^{(2)}} E_1^{(1)} + \frac{V^{(2)}}{V^{(1)}+V^{(2)}} E_1^{(2)} = \overline{E_1}, \tag{A.25}$$

$$\frac{V^{(3)}}{V^{(3)}+V^{(4)}} E_1^{(3)} + \frac{V^{(4)}}{V^{(3)}+V^{(4)}} E_1^{(4)} = \overline{E_1}, \tag{A.26}$$

$$\frac{V^{(1)}}{V^{(1)}+V^{(3)}} E_2^{(1)} + \frac{V^{(3)}}{V^{(1)}+V^{(3)}} E_2^{(3)} = \overline{E_2}, \tag{A.27}$$

$$\frac{V^{(2)}}{V^{(2)}+V^{(4)}} E_2^{(2)} + \frac{V^{(4)}}{V^{(2)}+V^{(4)}} E_2^{(4)} = \overline{E_2}, \tag{A.28}$$

$$E_3^{(1)} = \overline{E_3}, \tag{A.29}$$

$$E_3^{(2)} = \overline{E_3}, \tag{A.30}$$

$$E_3^{(3)} = \overline{E_3}, \tag{A.31}$$

$$E_3^{(4)} = \overline{E_3}. \tag{A.32}$$

The micromechanical relations for the electric flux continuity conditions are:

$$D_1^{(1)} - D_1^{(2)} = 0, \tag{A.33}$$

$$D_1^{(3)} - D_1^{(4)} = 0, \tag{A.34}$$

$$D_2^{(1)} - D_2^{(3)} = 0, \tag{A.35}$$

$$D_2^{(2)} - D_2^{(4)} = 0. \tag{A.36}$$

APPENDIX B

The micromechanical relations for the particle-unit-cell model, shown in Figure 3.1, are formed with similar assumptions to those of the fiber-unit-cell model. The linearized micromechanical relations for a piezocomposite with the poling direction aligned in the x_3 direction are summarized as follows. The micromechanical relations for the displacement compatibility conditions are:

$$\frac{V^{(1)}}{V^{(1)}+V^{(2)}}\varepsilon_{11}^{(1)}+\frac{V^{(2)}}{V^{(1)}+V^{(2)}}\varepsilon_{11}^{(2)}=\overline{\varepsilon_{11}}, \tag{B.1}$$

$$\frac{V^{(3)}}{V^{(3)}+V^{(4)}}\varepsilon_{11}^{(3)}+\frac{V^{(4)}}{V^{(3)}+V^{(4)}}\varepsilon_{11}^{(4)}=\overline{\varepsilon_{11}}, \tag{B.2}$$

$$\frac{V^{(5)}}{V^{(5)}+V^{(6)}}\varepsilon_{11}^{(5)}+\frac{V^{(6)}}{V^{(5)}+V^{(6)}}\varepsilon_{11}^{(6)}=\overline{\varepsilon_{11}}, \tag{B.3}$$

$$\frac{V^{(7)}}{V^{(7)}+V^{(8)}}\varepsilon_{11}^{(7)}+\frac{V^{(8)}}{V^{(7)}+V^{(8)}}\varepsilon_{11}^{(8)}=\overline{\varepsilon_{11}}, \tag{B.4}$$

$$\frac{V^{(1)}}{V^{(1)}+V^{(3)}}\varepsilon_{22}^{(1)}+\frac{V^{(3)}}{V^{(1)}+V^{(3)}}\varepsilon_{22}^{(3)}=\overline{\varepsilon_{22}}, \tag{B.5}$$

$$\frac{V^{(2)}}{V^{(2)}+V^{(4)}}\varepsilon_{22}^{(2)}+\frac{V^{(4)}}{V^{(2)}+V^{(4)}}\varepsilon_{22}^{(4)}=\overline{\varepsilon_{22}}, \tag{B.6}$$

$$\frac{V^{(5)}}{V^{(5)}+V^{(7)}}\varepsilon_{22}^{(5)}+\frac{V^{(7)}}{V^{(5)}+V^{(7)}}\varepsilon_{22}^{(7)}=\overline{\varepsilon_{22}}, \tag{B.7}$$

$$\frac{V^{(6)}}{V^{(6)}+V^{(8)}}\varepsilon_{22}^{(6)}+\frac{V^{(8)}}{V^{(6)}+V^{(8)}}\varepsilon_{22}^{(8)}=\overline{\varepsilon_{22}}, \tag{B.8}$$

$$\frac{V^{(1)}}{V^{(1)}+V^{(5)}}\varepsilon_{33}^{(1)}+\frac{V^{(5)}}{V^{(1)}+V^{(5)}}\varepsilon_{33}^{(5)}=\overline{\varepsilon_{33}}, \tag{B.9}$$

$$\frac{V^{(2)}}{V^{(2)}+V^{(6)}}\varepsilon_{33}^{(2)}+\frac{V^{(6)}}{V^{(2)}+V^{(6)}}\varepsilon_{33}^{(6)}=\overline{\varepsilon_{33}}, \tag{B.10}$$

$$\frac{V^{(3)}}{V^{(3)}+V^{(7)}}\varepsilon_{33}^{(3)}+\frac{V^{(7)}}{V^{(3)}+V^{(7)}}\varepsilon_{33}^{(7)}=\overline{\varepsilon_{33}}, \tag{B.11}$$

$$\frac{V^{(4)}}{V^{(4)}+V^{(8)}}\varepsilon_{33}^{(4)}+\frac{V^{(8)}}{V^{(4)}+V^{(8)}}\varepsilon_{33}^{(8)}=\overline{\varepsilon_{33}}, \tag{B.12}$$

$$\frac{V^{(1)}\cdot 2\varepsilon_{23}^{(1)}+V^{(3)}\cdot 2\varepsilon_{23}^{(3)}+V^{(5)}\cdot 2\varepsilon_{23}^{(5)}+V^{(7)}\cdot 2\varepsilon_{23}^{(7)}}{V^{(1)}+V^{(3)}+V^{(5)}+V^{(7)}}=2\overline{\varepsilon_{23}}, \tag{B.13}$$

$$\frac{V^{(2)}\cdot 2\varepsilon_{23}^{(2)}+V^{(4)}\cdot 2\varepsilon_{23}^{(4)}+V^{(6)}\cdot 2\varepsilon_{23}^{(6)}+V^{(8)}\cdot 2\varepsilon_{23}^{(8)}}{V^{(2)}+V^{(4)}+V^{(6)}+V^{(8)}}=2\overline{\varepsilon_{23}}, \tag{B.14}$$

$$\frac{V^{(1)}\cdot 2\varepsilon_{13}^{(1)}+V^{(2)}\cdot 2\varepsilon_{13}^{(2)}+V^{(5)}\cdot 2\varepsilon_{13}^{(5)}+V^{(6)}\cdot 2\varepsilon_{13}^{(6)}}{V^{(1)}+V^{(2)}+V^{(5)}+V^{(6)}}=2\overline{\varepsilon_{13}}, \tag{B.15}$$

$$\frac{V^{(3)}\cdot 2\varepsilon_{13}^{(3)}+V^{(4)}\cdot 2\varepsilon_{13}^{(4)}+V^{(7)}\cdot 2\varepsilon_{13}^{(7)}+V^{(8)}\cdot 2\varepsilon_{13}^{(8)}}{V^{(3)}+V^{(4)}+V^{(7)}+V^{(8)}}=2\overline{\varepsilon_{13}}, \tag{B.16}$$

$$\frac{V^{(1)}\cdot 2\varepsilon_{12}^{(1)}+V^{(2)}\cdot 2\varepsilon_{12}^{(2)}+V^{(3)}\cdot 2\varepsilon_{12}^{(3)}+V^{(4)}\cdot 2\varepsilon_{12}^{(4)}}{V^{(1)}+V^{(2)}+V^{(3)}+V^{(4)}}=2\overline{\varepsilon_{12}}, \tag{B.17}$$

$$\frac{V^{(5)}\cdot 2\varepsilon_{12}^{(5)}+V^{(6)}\cdot 2\varepsilon_{12}^{(6)}+V^{(7)}\cdot 2\varepsilon_{12}^{(7)}+V^{(8)}\cdot 2\varepsilon_{12}^{(8)}}{V^{(5)}+V^{(6)}+V^{(7)}+V^{(8)}}=2\overline{\varepsilon_{12}}. \tag{B.18}$$

The micromechanical relations for the traction continuity conditions are:

$$\sigma_{11}^{(1)}-\sigma_{11}^{(2)}=0, \tag{B.19}$$

$$\sigma_{11}^{(3)}-\sigma_{11}^{(4)}=0, \tag{B.20}$$

$$\sigma_{11}^{(5)} - \sigma_{11}^{(6)} = 0, \tag{B.21}$$

$$\sigma_{11}^{(7)} - \sigma_{11}^{(8)} = 0, \tag{B.22}$$

$$\sigma_{22}^{(1)} - \sigma_{22}^{(3)} = 0, \tag{B.23}$$

$$\sigma_{22}^{(2)} - \sigma_{22}^{(4)} = 0, \tag{B.24}$$

$$\sigma_{22}^{(5)} - \sigma_{22}^{(7)} = 0, \tag{B.25}$$

$$\sigma_{22}^{(6)} - \sigma_{22}^{(8)} = 0, \tag{B.26}$$

$$\sigma_{33}^{(1)} - \sigma_{33}^{(5)} = 0, \tag{B.27}$$

$$\sigma_{33}^{(2)} - \sigma_{33}^{(6)} = 0, \tag{B.28}$$

$$\sigma_{33}^{(3)} - \sigma_{33}^{(7)} = 0, \tag{B.29}$$

$$\sigma_{33}^{(4)} - \sigma_{33}^{(8)} = 0, \tag{B.30}$$

$$\sigma_{23}^{(1)} - \sigma_{23}^{(3)} = 0, \tag{B.31}$$

$$\sigma_{23}^{(1)} - \sigma_{23}^{(5)} = 0, \tag{B.32}$$

$$\sigma_{23}^{(1)} - \sigma_{23}^{(7)} = 0, \tag{B.33}$$

$$\sigma_{23}^{(2)} - \sigma_{23}^{(4)} = 0, \tag{B.34}$$

$$\sigma_{23}^{(2)} - \sigma_{23}^{(6)} = 0, \tag{B.35}$$

$$\sigma_{23}^{(2)} - \sigma_{23}^{(8)} = 0, \tag{B.36}$$

$$\sigma_{13}^{(1)} - \sigma_{13}^{(2)} = 0, \tag{B.37}$$

$$\sigma_{13}^{(1)} - \sigma_{13}^{(5)} = 0, \tag{B.38}$$

$$\sigma_{13}^{(1)} - \sigma_{13}^{(6)} = 0, \tag{B.39}$$

$$\sigma_{13}^{(3)} - \sigma_{13}^{(4)} = 0, \tag{B.40}$$

$$\sigma_{13}^{(3)} - \sigma_{13}^{(7)} = 0, \tag{B.41}$$

$$\sigma_{13}^{(3)} - \sigma_{13}^{(8)} = 0, \tag{B.42}$$

$$\sigma_{12}^{(1)} - \sigma_{12}^{(2)} = 0, \tag{B.43}$$

$$\sigma_{12}^{(1)} - \sigma_{12}^{(3)} = 0, \tag{B.44}$$

$$\sigma_{12}^{(1)} - \sigma_{12}^{(4)} = 0, \tag{B.45}$$

$$\sigma_{12}^{(5)} - \sigma_{12}^{(6)} = 0, \tag{B.46}$$

$$\sigma_{12}^{(5)} - \sigma_{12}^{(7)} = 0, \tag{B.47}$$

$$\sigma_{12}^{(5)} - \sigma_{12}^{(8)} = 0. \tag{B.48}$$

The micromechanical relations for the potential compatibility conditions are:

$$\frac{V^{(1)}}{V^{(1)}+V^{(2)}} E_1^{(1)} + \frac{V^{(2)}}{V^{(1)}+V^{(2)}} E_1^{(2)} = \overline{E_1}, \tag{B.49}$$

$$\frac{V^{(3)}}{V^{(3)}+V^{(4)}} E_1^{(3)} + \frac{V^{(4)}}{V^{(3)}+V^{(4)}} E_1^{(4)} = \overline{E_1}, \tag{B.50}$$

$$\frac{V^{(5)}}{V^{(5)}+V^{(6)}} E_1^{(5)} + \frac{V^{(6)}}{V^{(5)}+V^{(6)}} E_1^{(6)} = \overline{E_1}, \tag{B.51}$$

$$\frac{V^{(7)}}{V^{(7)}+V^{(8)}} E_1^{(7)} + \frac{V^{(8)}}{V^{(7)}+V^{(8)}} E_1^{(8)} = \overline{E_1}, \tag{B.52}$$

$$\frac{V^{(1)}}{V^{(1)}+V^{(3)}}E_2^{(1)}+\frac{V^{(3)}}{V^{(1)}+V^{(3)}}E_2^{(3)}=\overline{E_2}, \tag{B.53}$$

$$\frac{V^{(2)}}{V^{(2)}+V^{(4)}}E_2^{(2)}+\frac{V^{(4)}}{V^{(2)}+V^{(4)}}E_2^{(4)}=\overline{E_2}, \tag{B.54}$$

$$\frac{V^{(5)}}{V^{(5)}+V^{(7)}}E_2^{(5)}+\frac{V^{(7)}}{V^{(5)}+V^{(7)}}E_2^{(7)}=\overline{E_2}, \tag{B.55}$$

$$\frac{V^{(6)}}{V^{(6)}+V^{(8)}}E_2^{(6)}+\frac{V^{(8)}}{V^{(6)}+V^{(8)}}E_2^{(8)}=\overline{E_2}, \tag{B.56}$$

$$\frac{V^{(1)}}{V^{(1)}+V^{(5)}}E_3^{(1)}+\frac{V^{(5)}}{V^{(1)}+V^{(5)}}E_3^{(5)}=\overline{E_3}, \tag{B.57}$$

$$\frac{V^{(2)}}{V^{(2)}+V^{(6)}}E_3^{(2)}+\frac{V^{(6)}}{V^{(2)}+V^{(6)}}E_3^{(6)}=\overline{E_3}, \tag{B.58}$$

$$\frac{V^{(3)}}{V^{(3)}+V^{(7)}}E_3^{(3)}+\frac{V^{(7)}}{V^{(3)}+V^{(7)}}E_3^{(7)}=\overline{E_3}, \tag{B.59}$$

$$\frac{V^{(3)}}{V^{(3)}+V^{(7)}}E_3^{(3)}+\frac{V^{(7)}}{V^{(3)}+V^{(7)}}E_3^{(7)}=\overline{E_3}, \tag{B.60}$$

The micromechanical relations for the electric flux continuity conditions are:

$$D_1^{(1)}-D_1^{(2)}=0, \tag{B.61}$$

$$D_1^{(3)}-D_1^{(4)}=0, \tag{B.62}$$

$$D_1^{(5)}-D_1^{(6)}=0, \tag{B.63}$$

$$D_1^{(7)}-D_1^{(8)}=0, \tag{B.64}$$

$$D_2^{(1)}-D_2^{(3)}=0, \tag{B.65}$$

$$D_2^{(2)} - D_2^{(4)} = 0, \tag{B.66}$$

$$D_2^{(5)} - D_2^{(7)} = 0, \tag{B.67}$$

$$D_2^{(6)} - D_2^{(8)} = 0, \tag{B.68}$$

$$D_3^{(1)} - D_3^{(5)} = 0, \tag{B.69}$$

$$D_3^{(2)} - D_3^{(6)} = 0, \tag{B.70}$$

$$D_3^{(3)} - D_3^{(7)} = 0, \tag{B.71}$$

$$D_3^{(4)} - D_3^{(8)} = 0. \tag{B.72}$$